DISS. ETH NO. 23838

Magnetic Resonance Imaging of the Gastrointestinal Processing of Fat Emulsions

A thesis submitted to attain the degree of

Doctor of Sciences of ETH Zurich

(Dr. sc. ETH Zurich)

presented by

Dian Liu

Dipl.-Ing., Technische Universität Darmstadt

born on 24.06.1987

citizen of Germany

accepted on the recommendation of

Prof. Dr. Sebastian Kozerke

Prof. Dr. Peter A. Fischer

Dr. Andreas Steingötter

2016

读万卷书，

行万里路。

——刘彝

献给我的父母

Meinen Eltern gewidmet

Contents

Summary

The increased utilization of fat emulsions for functional foods has prompted increased efforts to correlate human fat digestion in the gastrointestinal (GI) tract to emulsion composition, structure and physiochemical properties. In particular, it has been previously shown that stable emulsions, whose structure and properties remain unchanged inside the stomach, exhibit differences in gastric emptying and satiety in comparison to unstable emulsions.

With magnetic resonance imaging (MRI), the in vivo processing of ingested emulsions can be visualized in order to reveal aspects of human GI function. However, conventional MRI has difficulties to quantify the changing structural properties of ingested meals during passage through the GI tract. Therefore, the use of quantitative MRI methods has been acknowledged to be of importance for nutritional science. To this day, the adaption of these quantitative methods for the study of emulsions has been very limited and thus, there is a huge potential of GI MRI that has been unused so far.

For an accurate and reliable application of quantitative methods for the in vivo assessment of fat emulsions, the complex structure of the emulsion needs to be taken into account. Fat emulsions can be described as a mixture of different signal compartments with different chemical shifts and relaxation times. The present work showed that this multi-compartment effect presented an important confounding factor for fast steady-state imaging sequences such as double echo steady-state (DESS) and triple echo steady-state (TESS). The measured signal intensities could

heavily depend on the choice of echo time (TE). Therefore, whenever fat was present, this had significant negative implications for quantitative parameter mapping, such as T_2 quantification.

The water–fat separation method of iterative decomposition with echo asymmetry and least squares estimation (IDEAL) allows for a robust separation of the measured signal into its water and fat compartments and can therefore be used to study the fate of fat during digestion. The method was validated in vitro and in vivo. In a cross-over study with 12 healthy subjects, gastric and duodenal fat emptying and related emulsion processing were investigated and quantified for a stable and an unstable emulsion. The study showed that, compared with the stable emulsion, the unstable emulsion indicated a faster gastric fat emptying and a strong creaming in the stomach.

The impact of the acidic gastric secretion on the ingested emulsion can be indirectly assessed by T_1 relaxation mapping. However, this is technically challenging due to the multi-compartment property of emulsions and the related bi-exponential relaxation behavior demands an additional correction. This was developed and evaluated in a combined fat fraction and secretion mapping scheme. In a parallel study with 21 healthy subjects, it was assessed how emulsion stability modulated the intragastric volumes, the layering and the mixing of emulsified fat and secretion and how the corresponding parameters were interrelated. The findings indicated that intragastric fat layering was mainly influenced by the degree of mixing rather than the overall dominance of secretion. The stable emulsion triggered a higher accumulation of gastric secretion, which in turn facilitated homogenization of intragastric content in comparison to its unstable counterpart.

The fourth study addressed the need for fast imaging sequences in GI MRI that allow the acquisition of abdominal volumes within one breath hold. Especially in clinical nutrition, these breath holds need to be sufficiently short in order to avoid artifacts from respiratory motion. This study acquired retrospectively and prospectively undersampled data from 7 healthy

subjects at a reduction factor $R = 4$. A dictionary-based signal model was integrated into image reconstruction. This allowed for the acceleration of gastric MRI at an improved image quality and increased accuracy of fat quantification in comparison to conventional parallel imaging (PI).

In conclusion, in this thesis methods for the in vivo quantification of fat emulsions in the stomach were developed, validated and their value for nutritional studies shown. The monitoring of the macrostructural behavior of ingested emulsions offers a more comprehensive analysis of human processing of food emulsion systems. The newly obtained insights have the potential to bridge the gap between current in vitro models and in vivo behavior.

Zusammenfassung

Die zunehmende Nutzung von Fettemulsionen als funktionelle Lebensmittel ist verknüpft mit zunehmenden Bestrebungen, die Zusammenhänge zwischen der menschlichen Fettverdauung im gastrointestinalen (GI) Trakt und dem Aufbau, der Struktur und der physikalisch-chemischen Eigenschaften von Emulsionen zu verstehen. Im Besonderen wurde bisher gezeigt, dass stabile Emulsionen, deren Struktur und Eigenschaften unverändert im Magen bleiben, sich in der Magenentleerung und Sättigung von instabilen Emulsionen unterscheiden.

Mit Magnetresonanztomographie (MRT) kann die Verdauung von eingenommenen Emulsionen visualisiert werden, um Aspekte der menschlichen GI-Funktion zu enthüllen. Allerdings ist es mit konventioneller MRT schwierig, die veränderten strukturellen Eigenschaften von eingenommenen Mahlzeiten zu quantifizieren, während diese den GI-Trakt passieren. Daher wird der Verwendung von quantitativen MRT-Methoden eine bedeutende Stellung in den Ernährungswissenschaften eingeräumt. Bisher gibt es jedoch nur sehr wenige Anwendungen dieser quantitativen Methoden für die Studie von Emulsionen, weshalb GI-MRT ein gewaltiges Potential besitzt, das bisher ungenutzt geblieben ist.

Für eine exakte und verlässliche Anwendung der quantitativen Methoden für die in-vivo-Untersuchung von Fettemulsionen muss die komplexe Struktur der Emulsionen berücksichtigt werden. Fettemulsionen können als Gemisch verschiedener Signalkompartimente mit verschiedenen chemischen Verschiebungen und Relaxationszeiten beschrieben werden. Die vorliegende Arbeit zeigte, dass dieser Multikompartimentseffekt ein

wichtiger Störfaktor für schnelle Steady-State-Sequenzen wie des Dual-Echo-Steady-States (DESS) und des Tripel-Echo-Steady-States (TESS) darstellte. Der Effekt bewirkte eine starke Abhängigkeit der gemessenen Signalintensitäten von der Wahl der Echozeiten. Sobald Fett vorhanden war, hatte dies signifikante negative Auswirkungen für quantitatives Parametermapping wie der T_2-Quantifizierung.

Die Wasser-Fett-Separationsmethode IDEAL erlaubt eine robuste Trennung des gemessenen Signals in seine Wasser- und Fettkompartimente und kann daher genutzt werden um das Verarbeitung von Fett während der Verdauung zu studieren. In dieser Arbeit wurde die Methode in vitro und in vivo validiert. In einer Crossover-Studie mit 12 gesunden Teilnehmern wurden gastrische und duodenale Fettentleerung und die dort auftretenden Emulsionsprozesse für eine stabile und instabile Emulsion untersucht und quantifiziert. Die Studie zeigte, dass im Vergleich zur stabilen Emulsion die instabile Emulsion eine schnellere Fettentleerung und ein stärkeres Aufrahmen im Magen aufwies.

Die Bedeutung der Magensekretion auf die aufgenommene Emulsion kann mit T_1-Relaxationsmapping untersucht werden. Dies ist jedoch aufgrund der Multikompartimentseigenschaft von Emulsionen technisch anspruchsvoll. Das einhergehende bi-exponentielle Relaxationsverhalten verlangt eine zusätzliche Korrektur, die in einem Ansatz mit kombiniertem Mapping von Fettanteil und Sekretion entwickelt und evaluiert wurde. In einer Parallel-Studie mit 21 gesunden Teilnehmern wurde untersucht, wie die Stabilität der Emulsion das intragastrische Volumen, die Schichtbildung und die Vermischung des emulgierten Fettes und auch der Sekretion moduliert und wie die dazugehörigen Parameter miteinander verknüpft waren. Es stellte sich dabei heraus, dass die intragastrische Bildung der Fettschicht vor allem durch den Vermischungsgrad anstelle der allgemeinen Dominanz von Sekretion beeinflusst wurde. Die stabile Emulsion löste im Vergleich zur instabilen eine höhere Akkumulation von Magensekretion aus, was wiederum das Homogenisieren des Mageninhalts vereinfachte.

Zusammenfassung

Die vierte Studie befasste sich mit der Notwendigkeit schneller Bildgebungssequenzen in GI-MRT, bei denen das abdominale Volumen innerhalb eines Atemstopps abgebildet werden kann. Vor allem in der klinischen Ernährung sind ausreichend kurze Atemstopps erforderlich um Artefakte aufgrund der kontinuierlich vorhandenen Atembewegungen zu vermeiden. Diese Studie erfasste bei 7 gesunden Teilnehmern retrospektiv und prospektiv unterabgetastete Daten mit einem Reduktionsfaktor $R = 4$. Ein Dictionary-basiertes Signalmodell wurde in die Bildrekonstruktion integriert und erlaubte damit die Beschleunigung von gastrischer MRT. Eine verbesserte Bildqualität und erhöhte Genauigkeit der Fettquantifizierung im Vergleich zu konventioneller paralleler Bildgebung war die Folge.

Zusammenfassend wurden in der vorliegenden Arbeit Methoden für die in-vivo-Quantifizierung von Fettemulsionen im Magen entwickelt, validiert und deren Wert für Ernährungsstudien aufgezeigt. Diese ermöglichten die Untersuchung eingenommener Emulsionen in Bezug auf ihre makrostrukturelle Veränderung in-vivo und somit eine umfassendere Analyse der Verarbeitung von Nahrungsemulsionssystemen im menschlichen GI-Trakt. Die somit generierten neuen Einblicke in die menschliche Verdauung helfen dabei die Lücke zwischen gegenwärtigen in-vitro-Modellen und dem in-vivo-Verhalten zu schliessen.

1   Introduction

1.1   Motivation

Fat forms an integral part of our daily food intake [1]. It is not only a source of essential polyunsaturated ω-3 and ω-6 fatty acids but it also facilitates absorption of fat-soluble vitamins, minerals, antinutrients and class II pharmaceuticals [2–7]. Moreover, fat acts as a carrier for fat-soluble aroma compounds, which make fatty foods highly appealing, giving it a key role in determining dietary preferences [8]. However, fat is the most energy dense of the macronutrients. Together with its attractive effect on humans, diets rich in fats have often been seen as a leading contributor to caloric overconsumption. Today, the increased prevalence of nutrition-related diseases and obesity is recognized as a worldwide health problem, which is especially pronounced in the Western world [9].

The serious health issues and increasing costs associated with over-weight has given rise to different approaches to counteract this trend. Approaches include the overall reduction of fat intake or a decrease in the digestibility of the fat. The negative side effects of these approaches are that also the positive functions of fat in foods are reduced, leading to the inhibited absorption of fat-soluble micronutrients, which must be compensated for. The alternative strategy to fight obesity is to design foods that control satiation and satiety [10] by protecting the fat in such a way that its release in the gastrointestinal (GI) tract is controlled. Since many natural and processed fatty foods consist either partly or wholly as fat emulsions, including milk, sauces, soups, salad dressings and desserts,

there has been an increased utilization of fat emulsions for functional foods. This has prompted for increased efforts to correlate human fat digestion, absorption and related peptide hormone release in the GI tract to emulsion composition, structure and physiochemical properties [11]. For example, the tendency for fat droplet creaming and flocculation to occur within the stomach has been shown to modulate, i.e. reduce satiety and satiation [12, 13] and hence, there has been interest in designing fat emulsions that remain stable within the stomach.

The whole process from fat intake to absorption and satiety feelings is a complex and highly integrated system and thus, attempts to understand and subsequently modulate food intake is a challenging task. Modern fat emulsion design relies on the integration of knowledge from different scientific disciplines in order to obtain a more holistic understanding of fat emulsions [14, 15]. Research is carried out at different levels, ranging from the study of emulsion structure and physiochemical properties to the study of the behavior of emulsions within the human body after ingestion. The characterization of the GI fate of fat emulsions has been the focus of a great deal of research the past decade, which has led to a corresponding interest in the development of appropriate techniques. One of the most effective in vivo technique for visualizing the dynamic behavior of ingested fat emulsions is magnetic resonance imaging (MRI). It has evolved as a promising imaging modality to comprehensively analyze aspects of human GI function including emptying, motility, secretion, mixing, distribution and transport. With the use of MRI, it has been previously shown that stable emulsions that remain evenly distributed throughout the stomach lead to slower gastric emptying and therefore, a higher feeling of satiety in comparison to unstable emulsions [16–19].

When imaging the GI tract, several challenges have to be faced. The three-dimensional (3D) morphology is complex and highly variable not only between individuals [20] but also within one individual depending on the amount of the ingested meal and stage of digestion. Especially in the lower GI tract, i.e. small intestine and colon, the analysis of images becomes

very difficult and insights into the structure and function are hard to obtain. For these reasons, advances in imaging techniques usually occur first for the stomach before they are applied to the more complicated structures of intestinal loops.

Another key constraint in GI MRI is motion. It can be classified into respiratory motion, GI motility and the constant flux of intraluminal content traveling down the GI tract. Whereas the two latter motion types are of highly irregular nature, which hampers the application of gating approaches as frequently employed in cardiac imaging [21], respiratory motion necessitates the use of fast imaging sequences that allow acquisitions within one breath hold. In general, since there is always a tradeoff between scan duration, signal-to-noise ratio (SNR) and resolution, compromises on image quality and the spatial resolution have to be made.

Besides, the limited information provided by conventional MRI on the composition of intraluminal GI content is mainly of qualitative nature. Since images are produced only in grayscale, it is difficult to differentiate between the individual foods and to quantitatively monitor the changing structural properties of the ingested emulsion during passage through the GI tract. For this reason, the use of quantitative MRI methods, which involves the measurement of quantifiable physical properties of tissue, has been acknowledged to be of importance for nutritional science [22–24]. One promising example is the quantification of T_1 relaxation for ingested aqueous foods, which allows for the separate detection of meal and secretion volumes in the stomach [25]. However, for an accurate and reliable adaption to the in vivo processing of fat emulsions, its complex structure needs to be taken into account. Fat has magnetic resonance (MR) properties that are very different to those of water, and therefore, a bi-exponential decay must be considered when quantifying T_1 and T_2 relaxation. In general, the adaption of quantitative methods for the study of fat emulsions have been very limited and thus, there is a huge potential of GI MRI that has been unused to this date.

1.2   Outline

An introduction to fat emulsions and their digestion, followed by an overview of methods to monitor and to characterize the ingested fat emulsions passing through the GI tract are presented in Chapter 2.

Quantitative MRI methods using rapid imaging sequences or accelerated acquisitions that are relevant for the in vivo characterization of fat emulsions are described in Chapter 3.

The modulation of the steady-state signal of fat emulsions due to their complex composition in double echo steady-state (DESS) and triple echo steady-state (TESS) sequences is shown in Chapter 4. It highlights the employment of adequate multi-compartment models in MR parameter quantification.

Chapter 5 presents the quantification of ingested emulsified fat using a multipeak spectral fat model for water-fat separation. Based on two fat emulsions of different stability, an in vivo study was carried out to assess the influence of stability on the fat distribution and related processing within the stomach and duodenum.

The presented method is advanced in Chapter 6 for the simultaneous quantification of fat and gastric secretion. The corresponding in vivo study analyzes the influence of stability on secretion in the stomach. Additional insights were derived on the degree of influence that secretion and fat have on each other during the gastric emptying period.

A signal model-based approach using dictionaries for accelerating gastric fat quantification at an acceleration factor of 4 is given in Chapter 7. The incorporation of a priori knowledge is proposed for providing an improved quality of the reconstruction and an accurate detection of gastric fat volumes compared to conventional parallel imaging (PI) methods.

Chapter 8 summarizes the findings of this thesis and gives an outlook on potential future developments.

1.3   Contribution of the thesis

By the development of fast quantitative MRI methods, studies on fat emulsions during passage through the stomach has been made possible in human. It was shown on the example of the DESS and TESS sequence that multi-compartment effects modulate the signal when measuring emulsified or pure fat. Therefore, in order to accurately quantify MR parameters of fat emulsions, the underlying signal model needs to be adapted.

The quantification of emulsified fat was validated in vivo using a multi-peak spectral fat model, which provided a reliable characterization of the fat emptying and emulsion processing in stomach and duodenum. It revealed differences in emptying, phase separation and creaming depending on the emulsion stability.

The combination of this method with T_1 quantification allowed to simultaneously quantify gastric secretion and fat. It was observed that emulsion stability clearly modulates the spatial and temporal behavior of fat and secretion in the stomach. The stable emulsion impedes the creaming process and its emulsified fat empties slower from the stomach than its unstable counterpart. In terms of secretion, the stable emulsion shows an increased accumulation of secretion in the stomach and promotes mixing between fat and secretion.

In clinical nutrition, where study settings involve obese subjects, the breath hold durations required for fat quantification needs to be further reduced. For this, a framework using signal-model based dictionaries was developed, which improved the quality of the reconstructed image in terms of root mean square error (RMSE) and offered an accurate measurement of gastric fat volumes.

2 Fat emulsions and digestion

2.1 Principles

An emulsion is a mixture of two immiscible liquids, in which one of the liquids is dispersed as droplets within the other [11]. The most common emulsion in foods is an oil-in-water emulsion, which will be called fat emulsion throughout the thesis. Examples of fat emulsions are dressings, mayonnaise, sauces, milk, cream and a wide range of other dairy products. Usually, the diameters of the fat droplets range between 100 nm and 100 μm.

Due to the thermodynamical instability of emulsions, homogenization of pure water and pure oil cannot be maintained. When stirring them together, the mixture immediately separates into its two original phases, where a layer of oil due to its lower density is formed on top of a layer of water due to its higher density. However, the use of emulsifiers enhances the kinetic stability of the emulsions, which slows down the phase separation process and enables the production of emulsions that are stable for a reasonable period of time. Many emulsions are stabilized by surface-active biopolymers of different characteristics. For example, proteins are particularly sensitive to pH changes and ionic strength [26] and are therefore prone to instability within the gastric environment, whereas polysaccharides tend to be resistant to pH but need to be added at high concentrations [27].
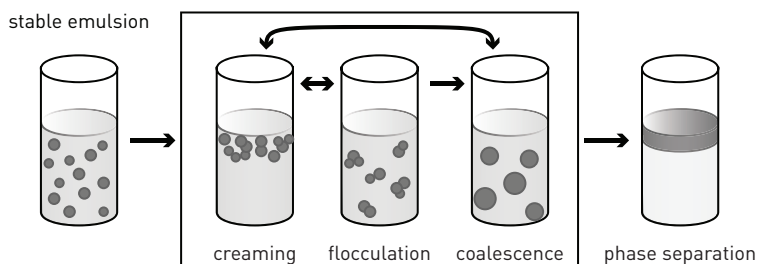
Figure 2.1 *Schematic representation of emulsion stability through a variety of physical mechanisms.*

2.1.1   Modes of instability

In foods, most forms of emulsion instability are undesirable as they lead to quality impairments. The most common modes that are responsible for emulsion instability can be categorized into several physical processes [28], which are shown schematically in Figure 2.1.

Creaming is a form of gravitational separation due to the different densities of the emulsion phases. Since most edible oils are less dense than water, creaming describes the upward movement of fat droplets.

Flocculation occurs when two or more droplets come together to form an aggregate in which the droplets retain their individual integrity.

Coalescence is another type of droplet aggregation where two or more droplets merge together to form a single larger droplet. This is an irreversible process, which constitutes the most important difference between creaming and flocculation, where droplets may separate again. Extensive droplet coalescence can eventually lead to the formation of a separate layer of oil on top of the emulsion.

In addition to the physical processes leading to instability, emulsions are also affected by a variety of chemical processes such as lipid oxidation and enzyme hydrolysis and microbiological processes such as bacterial growth.

2.2   Human digestion

After ingestion, the structural and functional properties of the ingested fat emulsion undergo constant change under the different gastrointestinal (GI) environments [29], where each GI unit plays a different role in digestion. During its passage through the GI tract, the major macronutrients, i.e. fats, proteins, and carbohydrates, are gradually broken down into their digestion products (Figure 2.2).

2.2.1   Chemosensory communication

Chemosensory receptors, which detect the nutrients during passage, are spread out over the various units of the GI tract [30]. They provide hormonal and neural signal communication between the spatially separated GI units, making them highly connected to each other [1]. These numerous signal responses influence eating pleasure, food intake, and nutrient processing. Normally, they are highly regulated to maintain an optimum body weight and composition. In order to promote food consumption, the body is able to generate hormonal hunger signals that stimulate the feeling of hunger, such as ghrelin [13, 31]. Respective inhibitory or fullness signals such as cholycystokinin (CCK), peptide tyrosine tyrosine (PYY) and glucagon-like peptide (GLP-1) are another set of peptides, which counterpart the hunger signals to suppress appetite and inhibit food intake. The composition, structure, and breakdown of emulsions within the GI tract influences the release of these peptides and can therefore be manipulated in order to control satiation and satiety. The decreased desire to consume food during a meal is known as satiation, whereas the reduced desire to consume food after a meal has been completed is known as satiety. Satiation therefore influences the total amount of food consumed during a particular meal, whereas satiety influences the length of time before a person feels hungry again, and therefore influences the total amount of food consumed daily.

2.2.2   Mouth

Digestion already starts in the mouth where the ingested emulsion is exposed to increased ionic strength, mucin and amylase [11]. pH remains about neutral, the surrounding temperature increases and mastication further applies mechanical stress on the emulsion.

2.2.3   Stomach

After swallowing, the emulsion is passed through the esophagus into the stomach where it is mixed with gastric secretion, stored, and further processed [32, 33]. The motility of the stomach establishes a complex set of flow and force patterns for these tasks. Gastric secretion plays an important role in preventing infection by contaminated foods, as well as facilitating the breakdown of the food matrix so as to facilitate nutrient, especially protein, absorption. In the fasted state, gastric secretion is usually highly acidic, with pH generally ranging from 1 to 3 depending on the individual. After ingestion, the quantity and type of meal consumed affects the subsequent changes of pH, typically leading to an increase. Together with the highly acidic environment, the mixture of digestive enzymes within the gastric secretion have a pronounced influence on the emulsion stability, which may promote chemical degradation of some food components that in turn, may alter emulsion stability and properties. Whereas major emulsion structuring occurs within the stomach, only limited lipolysis, i.e. the breakup of triglycerides in the emulsified fat into fatty acids suitable for absorption, takes place. Therefore, the changes in emulsion structure mainly depend on the initial state of the fat droplets entering the stomach. The tendency for fat droplet aggregation to occur within the stomach influences the hormone response of the ingested meal and may be an important modulator for satiety and satiation [12, 13]. It has also been suggested that stable emulsions lead to slower gastric emptying and therefore a higher feeling of satiety than unstable emulsions [17, 18].
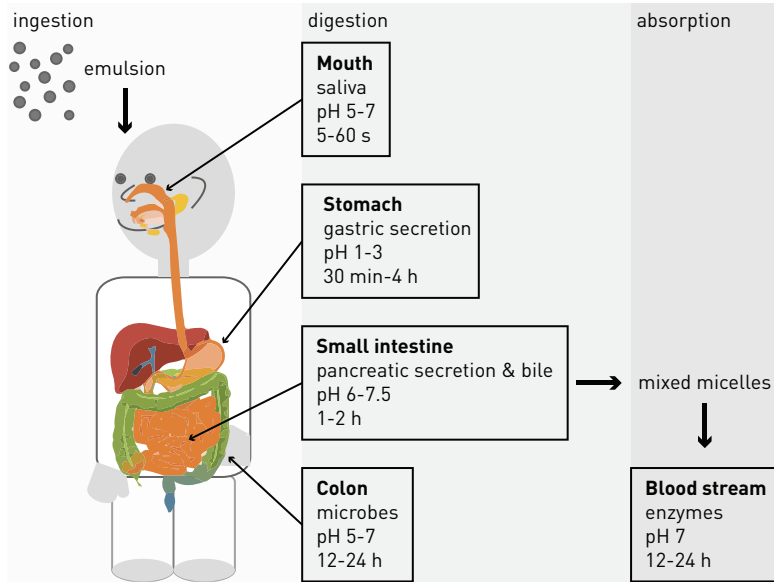
Figure 2.2 *The different units of the human GI tract with their respective intraluminal pH values, released GI fluids and passage times.*

2.2.4   Small intestine

The partially digested contents leaving the gastric environment pass through a small muscular valve called the pylorus sphincter, which opens and closes so as to control the flow of intraluminal content from the stomach to the duodenum [1, 34]. The flow and the subsequent nutrient sensing by the intestinal mucosa induces a large range of inhibiting pathways, together called the enterogastric reflexes, which down-regulate stomach activity and gastric emptying rate. The small intestine is the main site of absorption and detection of nutrients and is usually divided into three successive sections, the duodenum, the jejunum, and the ileum. Intraluminal content within the duodenum is mixed with pancreatic secretion and bile from the gallbladder. The alkaline pancreatic secretion causes an increase in the pH of the intestinal contents until it eventually becomes around neutral. Most of the lipolysis takes place in the small intestine,

where the digestive enzymes in the pancreatic secretion further break down the fat into its absorbable form of fatty acids. The fatty acids form into mixed micelles and are normally almost fully absorbed through the mucus layer lining the intestinal wall. Bile from the gallbladder facilitates their adsorption by acting as a surfactant that stabilizes the micelles. The remaining mainly indigestible contents pass the ileocecal valve to enter the colon.

2.3   Assessment of emulsion digestion

Understanding the GI fate of fat emulsions has been the focus of a great deal of research during the past decade, which has led to a corresponding interest in the development of appropriate techniques. These techniques can broadly be divided into in vitro simulations, animal feeding studies and human in vivo studies. Since it is extremely difficult to accurately simulate the complex processes that occur within the human GI tract by only one technique, it is often helpful to use a combination of different techniques to understand how an emulsion behaves in the GI tract. The establishment of robust in vitro–in vivo correlations is of importance as it ensures that any in vitro method used to test a meal gives a reliable prediction of its performance in vivo.

2.3.1   In vitro simulations

In vitro simulations offer several advantages over in vivo studies because they are usually faster, less expensive and more versatile [32]. Since they allow the physicochemical characterization of emulsions, they are are most suitable for rapidly screening and adapting key physicochemical attributes of different formulations during the early development of emulsions. A reliable prediction of the in vivo evolution of the emulsion structure is usually required before ethical consideration for in vivo studies [35–37]. In vitro approaches vary in their sophistication and accuracy. Some of the approaches focus on one particular unit of the GI tract, whereas others are

based on a number of sequential steps to more accurately mimic the entire GI tract [37]. Typically, a sample is prepared and then sequentially subjected to one or more environments designed to simulate the main GI units, such as mouth, stomach, small intestine and colon. Usually, the passage of an ingested meal through the GI tract is simulated at body temperature, i.e. 37°C, by exposing it to a series of different simulated GI secretions with adapted compositions. The development of a suitable simulation requires an understanding of the influence of different GI environments on the properties of an emulsion [1, 33].

There have been numerous in vitro simulations that focus on the behavior of emulsions during passage through the stomach [29, 38, 39]. It is common to mix the emulsion sample with simulated gastric fluid (SGF) for a specified time under fixed agitation conditions. To simulate gastric conditions, a volume ratio of 1:1 of the sample to SGF is often used, where the SGF is typically a highly acidic aqueous solution that contains acids, buffers, salts, and digestive gastric enzymes. In the small intestine, the timings, the level of agitation, the composition of the simulated secretion and its pH need to be adjusted. The sample collected after this processing stage can either be passed on to simulate the colon, or for the analysis of nutrient absorption. Absorption simulations mimic the uptake in mucus layer of the small intestine, which can be performed using physical [40], biological [41] or cellculture approaches [42].

It is also useful to derive models based on computational fluid dynamics that numerically predict the dynamics of the ingested emulsions in the GI tract such as in the stomach [43]. These numerical models are based on knowledge of the stomach's anatomy and its physiological conditions.

2.3.2   Animal feeding studies

A more realistic indication of the potential performance of a fat emulsion can be obtained using in vivo feeding studies with animals, which aims to extrapolate the findings to human fat digestion [33]. They are useful when the setup of human studies is limited by factors such as ethical

regulations, high expenses and difficulties in controlling diet and life style during studies. The easiest and most commonly used animals to study digestion and absorption of food components are rodents, i.e. mice or rats [44, 45]. However, due to their often appreciably different GI tract, study outcomes can often only provide limited information. Therefore, pigs, which have an anatomy and physiology of the digestive system that are similar to those of humans [46], are sometimes used. An animal may be fed the emulsion being tested, either alone or as part of a diet, over a specified period. Changes in the whole animal in terms of behavior or body weight or changes in specific internal organs may be measured, typically after the animal is sacrificed. In particular, the liver is the major organ for lipid metabolism and thus it is very important to evaluate for emulsion studies. Alternatively, changes in the composition of the feces, urine, blood, or breath of an animal may be measured to monitor the absorption, metabolism and excretion of a particular component. In some cases, it is possible to pass invasive tubes through the GI tract of live animals to collect samples of the ingested emulsion.

2.3.3 Human in vivo studies

The ability to characterize emulsion digestion and the resulting metabolic processes in vivo has shown considerable advances in recent years [38]. Similar to animal feeding studies, samples of the ingested fat emulsion can be collected from different units within the GI tract by nasogastric intubation [47] (Figure 2.3a). After inserting the invasive tube through the mouth of the subject, the emulsion to be tested can be administered normally or through the tube. Samples of the partially digested emulsion can then be aspirated at different times after ingestion, and at different positions within the digestive tract by physically positioning the tube at different locations. This procedure may cause temporary discomfort but can provide an estimation of what happens in the human GI tract. The collected samples can then be analyzed in the laboratory in order to determine their properties. For example, the pH, ionic strength, overall microstructure, droplet size
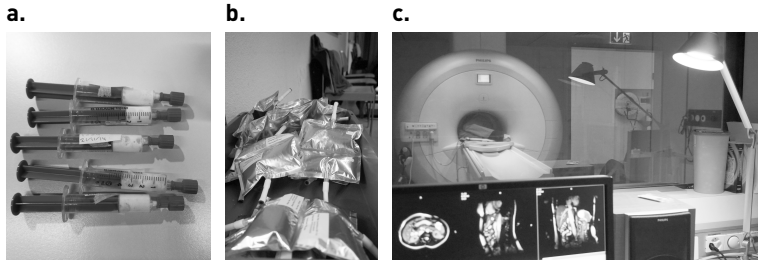
Figure 2.3 *Pictures of (a) a nasogastric tube for in human use with corresponding aspirated samples of an ingested fat emulsion, (b) breath testing bags filled with exhaled air and (c) 1.5 T whole-body magnetic resonance imaging (MRI) system.*

distribution, interfacial composition, and viscosity could be analyzed as the ingested emulsion passes through the human subject.

The use of stable isotope breath testing [48] can be very useful to understand digestion and absorption of food components (Figure 2.3b). This is a technique, which administers a labeled compound and traces its fate in the human body by measuring its disappearance from the endogenous pool. If the emulsion to be ingested is labeled with isotope ^{13}C, then the absorption and subsequent metabolization in the liver to labeled carbon dioxide $^{13}CO_2$ can be measured from the exhaled air. Stable isotopes are non-radioactive and are thus considered safe. However, it has still to be proven that measurement of stable isotopes in the breath is the correct reflection of the function of interest. Interpretation of data requires good understanding of the metabolic fate in the human system, for example, what are the absorption, delivery, metabolism, and elimination processes for the labeled compound.

Based on the fact that whatever is not absorbed or digested should be eliminated from the body, collecting and analyzing fecal samples can provide valuable information without invasive methods [32]. Although this method obviously may not provide detailed information about the events happening in the GI tract, some valuable information can be obtained, e.g. the total amount and types of lipids, cholesterol, or bile salts excreted.

The undigested target samples can be recovered and analyzed using appropriate analytical methods, and the absorption yield can be obtained. Another sampling methods from human subjects is drawing blood [49]. Blood can be useful for certain bio-markers, which provide an indication of the absorption, metabolism, or bioactivity of particular food components, e.g. profile of lipids and peptides [50]. Similar types of analyses can be carried out on urine samples.

Recently, a number of whole-body, noninvasive imaging modalities have been employed to follow the fate of foods after ingestion. Typically, gastric emptying is studied. For example, ultrasound has been used for the characterization of GI function such as for the measurement of gastric emptying and gallbladder contractions [51] whereas scintigraphy has been applied for gastric emptying and accommodation [52].

One of the most effective systems for visualizing dynamic changes of ingested emulsions is MRI (Figure 2.3c). Like ultrasound, it is radiation-free and noninvasive but offers dynamic imaging at a high spatial and temporal resolutions with large volume coverage, good image quality and contrast. Developments in abdominal MRI mostly aimed at detecting mural and transmural diesease but have been recently exploited for the application of functional GI imaging [53–56]. It has evolved as a promising imaging modality and has been validated for physiologic and clinical measurements. In particular it has the ability to comprehensively visualize aspects of human GI function including emptying, motility, secretion, mixing, distribution and transport in health and disease states. The ability of MRI to assess multiple aspects of GI physiomechanics simultaneously represents a significant improvement compared to other technologies. To this date, MRI has been used in a handful of fat emulsion studies, often in conjunction with other complementary methods, and it was suggested that stable emulsions lead to slower gastric emptying and therefore a higher feeling of satiety, than unstable emulsions [16–19]. This may be able to provide important information about the digestion and absorption of fats in humans.

3   Fast quantitative imaging

Magnetic resonance imaging (MRI) allows to manipulate image contrast by choice of different excitation and detection techniques and therefore, offers tissue contrast to be adjusted to specific applications. Proton density ρ, longitudinal relaxation time T_1 and transverse relaxation time T_2 are the three most basic, intrinsic magnetic resonance (MR) properties. The weighting by one or by a mixture of several of the properties results in the specific tissue contrast in the acquired images.

Although conventional contrast-based imaging techniques are sensitive to differentiate between tissues, they are also sensitive to differences in hardware and image acquisition parameters, such as repetition time (TR), echo time (TE), radiofrequency (RF) irradiation power and frequency offset. The development of quantitative MRI methods therefore enables to characterize tissues more objectively and independently of system and sequence. The quantification of T_1, T_2, fat fraction, diffusion coefficient and magnetization transfer have been widely used to study the human body in health and disease state. In nutritional science, it is generally understood that T_1 and T_2 water relaxation and diffusion characteristics reflect molecular and microscopic structural properties of food colloids [23]. This dependency is exploited to determine the change in macromolecular food structure induced by processing operations. Extrapolations of these techniques to physiological applications have been very limited. A few possible quantitative approaches are presented in this chapter. Moreover, acceleration techniques to shorten image acquisition are addressed in order to relax the time constraints in gastrointestinal (GI) MRI.

3.1 T_1 **mapping**

The inversion recovery (IR) sequence represents the standard MR sequence for T_1 quantification. In the equilibrium state, the magnetization vector is aligned along the z axis, that is, $\boldsymbol{M} = (0, 0, M_0)^T$. Note that all vectors and matrices are represented as bold letters to distinguish them from scalars. An inversion pulse flips the longitudinal magnetization from the $+z$ axis to the $-z$ axis by a flip angle of $\alpha_I = 180°$ for a complete inversion. Immediately after the inversion, the longitudinal magnetization M_z becomes,

$$M_z = M_0 \cos \alpha_I = -M_0 \,. \tag{3.1}$$

Before applying the RF excitation pulse, a time delay known as the inversion time (TI) is provided to allow the inverted magnetization to recover toward its equilibrium value. Tissues with different T_1 values recover at different rates, creating a T_1 contrast among them. During time $t =$TI, an applied spoiler gradient dephases the transversal component while the longitudinal magnetization experiences T_1 relaxation according to the Bloch equation,

$$\frac{dM_z}{dt} = \frac{M_0 - M_z}{T_1} \,. \tag{3.2}$$

Using the initial condition given in Eq. 3.1 at $t = 0$, the longitudinal magnetization becomes,

$$M_z(t) = M_0 \left[1 - (1 - \cos \alpha_I) e^{-t/T_1} \right] = M_0 (1 - 2e^{-t/T_1}) \,. \tag{3.3}$$

The RF excitation pulse then tips the longitudinal magnetization into the transverse plane to provide the T_1 weighted signal. The next IR measurement is performed after a long TR, typically in the rage of 5-10 s, in order to allow full recovery.

One way to quantify T_1 is to find the zero-crossing point of the magnetization,

$$T_{I,\text{null}} = T_1 \ln 2 \,. \tag{3.4}$$

Alternatively, consecutive measurements of the IR sequence at different TIs along the longitudinal recovery curve can be performed. A two-parameter, nonlinear least squares fit according to Eq. 3.3 is then applied at the measured time points.

Although the IR sequence provides accurate quantification of T_1, it suffers from extremely long acquisition times, which makes it sensitive to motion. It is therefore not suitable for abdominal imaging where breath holds are necessary. Modified IR sequences such as the Lock-Looker sequence [57] have much shorter acquisition times, which makes them more suitable for in vivo use. In contrast to IR, a set of small flip angle RF pulses are applied after the inversion pulse during each repetition period. This allows to sample multiple time points on the longitudinal recovery curve. It can be shown that within the limit of small flip angles, the measured signal is manipulated similar to an IR sequence. The modified Look-Locker sequence (MOLLI) is a variation of this sequence and is the most widely used technique for cardiac applications [58].

3.1.1   Dual flip angle technique

In addition to the Look-Locker sequence, there is another common fast T_1 mapping technique, which is based on variable flip angles [59]. Instead of sampling the longitudinal recovery curve, several images with different flip angles (FAs) are consecutively acquired in a spoiled gradient echo steady-state sequence. The theoretical signal intensity of the steady-state signal is a complex function of the equilibrium longitudinal magnetization, relaxation times T_1 and T_2 and sequence parameters TR, TE and FA α,

$$s = M_0 \sin \alpha \, \frac{(1 - E_1) \, E_2}{1 - E_1 \cos \alpha} \, , \tag{3.5}$$

where $E_1 = e^{-TR/T_1}$ and $E_2 = e^{-TE/T_2}$. Eq. 3.5 can be expressed in linear form $y = ax + b$,

$$\frac{s}{\sin \alpha} = E_1 \frac{s}{\tan \alpha} + M_0 (1 - E_1) \, E_2 \, . \tag{3.6}$$
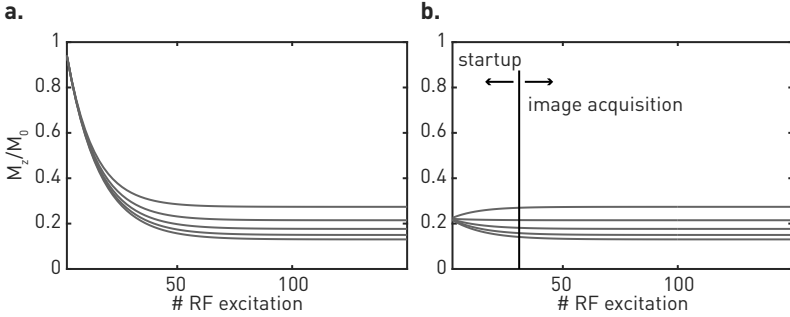
Figure 3.1 *Normalized longitudinal magnetization as a function of RF excitation number (a) without startup and (b) with an optimized startup. All curves are plotted for TR of 9 ms, FA of 20° and five T_1 values ranging between 200 and 1000 ms. By selecting an optimized startup parameters (initial FAs of 78°, 30 cycles), the duration to establish steady-state can be minimized over the considered T_1 range.*

Since only the FA is varied while TR and TE remain constant, a linear fit that is characterized by slope $a = E_1$ and intercept $b = M_0(1 - E_1)E_2$ can be applied to the different FA acquisitions. A special case is the dual flip angle (DFA) technique, which relies on two FA acquisitions where T_1 is computed according to,

$$T_1 = \frac{TR}{\ln a} \, .$$

(3.7)

The estimation of T_1 based on Eq. 3.7 is only valid under certain assumptions. First, the longitudinal magnetization needs to reach its dynamic equilibrium, i.e. steady-state. This is established by inserting a certain number of dummy excitations or startup cycles before the actual image acquisition. The duration of the startup cycles can be significantly decreased by choosing an initial FA that is lower than the subsequently applied FAs as shown in Figure 3.1. In order to derive optimal startup parameters, the time evolution of longitudinal magnetization is simulated for a given T_1 range of interest. This allows to probe all possible startup FA combinations and to select the optimal FAs with the corresponding number of startup cycles.

Moreover, the applied nominal FA is assumed to be valid. This is fulfilled

if amplitude of the transmit RF field B_1 is assumed homogeneous over the complete field of view (FOV) and the applied RF pulses are of uniform, nominal value over the whole selected slice.

3.1.2 B_1 **correction**

Inhomogeneity of the RF transmit field B_1 induces spatial variations in the nominal FA. Since the DFA technique relies on the correct FAs values and is sensitive of variations thereof, the measurements need be corrected with a B_1 map. For B_1 mapping, one common technique is derived from dual TR measurements, known as actual flip angle imaging (AFI) [60, 61]. The practical limitation of this method is mainly due to the duration of the B_1 mapping acquisition, which gives rise to flow and motion artifacts especially in abdominal imaging. More importantly, the combined T_1-B_1 mapping scheme usually does not fit into one single breath hold, resulting in a reduced alignment between the DFA acquisitions and the corrections derived from the B_1 map. Dubbed dual refocusing echo acquisition mode (DREAM) is a rapid multislice B_1 mapping technique, which is more than an order of magnitude faster than existing techniques [62]. It is depicted in Figure 3.2. It employs a stimulated echo acquisition mode (STEAM) preparation sequence employing the same pulse shape as for the DFA sequence. Directly after the preparation, the longitudinal magnetization is given by [63],

$$M_{z,\text{STE}} = \frac{1}{2} M_0 \sin^2 \alpha \,, \tag{3.8}$$

$$M_{z,\text{FID}} = M_0 \cos^2 \alpha \,, \tag{3.9}$$

where $M_{z,\text{STE}}$ and $M_{z,\text{FID}}$ denote the STEAM-prepared and the unprepared longitudinal magnetization, respectively, and α is the unknown FA of the STEAM pulses. The following tailored single-shot gradient echo sequence with imaging FA β simultaneously measures the stimulated echo and the free induction decay as gradient-recalled echoes, S_{STE} and S_{FID}, respec-
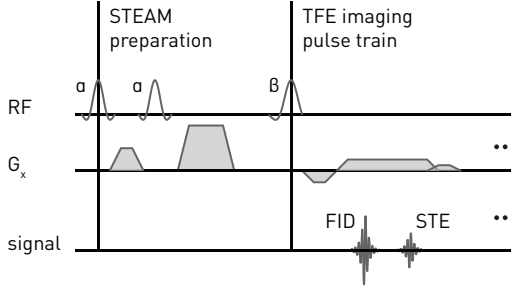
Figure 3.2 *Pulse sequence scheme of DREAM. For clarity, the gradients for slice selection and phase encoding have been omitted.*

tively. Their intensities are given by,

$$S_{\text{STE}} = \sin \beta \, M_{z,\text{STE}} = \frac{1}{2} M_0 \sin \beta \sin^2 \alpha \,, \qquad (3.10)$$

$$S_{\text{FID}} = \sin \beta \, M_{z,\text{FID}} = \quad M_0 \sin \beta \cos^2 \alpha \,. \qquad (3.11)$$

Their ratio is used to derive the actual FA α according to the analytic expression,

$$\alpha = \arctan \sqrt{\frac{2S_{\text{STE}}}{S_{\text{FID}}}} \,. \qquad (3.12)$$

The RF excitation pulse, image geometry and RF power are chosen to be identical for both DFA and DREAM sequence, resulting in an equal FA distribution over the complete FOV.

3.1.3   Slice profile correction

The correction of the nominal FAs for their actual FAs by B_1 mapping is an accurate approach for three-dimensional (3D) and nonselective RF excitation pulses. Two-dimensional (2D) encoding however, additionally suffers from the imperfections of slice-selective RF pulses, which give rise to slice profile effects. This leads to additional systematic errors in the FA correction [64].

Slice profile correction takes into account the temporal shape of the

applied RF pulse $B_1(t)$ and translates it to their spatial slice profile in order to simulate a more realistic FA. Since slice-selective RF pulses are usually sinc pulses, the corresponding excited spins will not represent a perfect rectangle along slice selection direction z. Knowledge on the applied sinc pulse allows to relate it to the slice profile of its actual FA $\alpha(z)$ by Fourier transform,

$$\alpha(z) = \frac{\gamma}{2\pi} \int_{-\infty}^{\infty} B_1(t) e^{-j2\pi\gamma G_z z t} dt \,, \qquad (3.13)$$

where γ is the gyromagnetic ratio ($\gamma_{\text{proton}} = 2\pi \cdot 42.6 \frac{\text{MHz}}{\text{T}}$) and G_z the slice selection gradient. Based on the estimated FAs, the corresponding steady-state signal along z within the slice $s'(z)$ is computed according to Eq. 3.5. The received signal intensity can finally be estimated as its average over the whole slice, which is an integration over the slice profile normalized to the slice thickness TH,

$$s = \frac{1}{\text{TH}} \int_{-\infty}^{\infty} s'(z) \, dz \,. \qquad (3.14)$$

Since the calculation of the steady-state signal depends on T_1 of the considered tissue, the slice profile correction needs to be incorporated directly into the T_1 estimation process, which is demonstrated in Figure 3.3. In this iterative process, first the actual FA is simulated according to Eq. 3.13. By assuming the estimated T_1 value without slice profile correction as an initial guess for T_1, the corresponding steady-state signal is calculated according to Eq. 3.14. Last, T_1 is estimated according to Eq. 3.7. The resulting T_1 serves as an update for a second iteration of FA and T_1 estimation, which is repeated (e.g. ten iterations) until convergence is reached.

3.1.4   Quantification of dilution by gastric secretion

Fast T_1 quantification enables the quantification of dilution of gastric secretion [25], which allows for separate detection of intragastric meal and secretion volumes in health and disease states [65, 66]. By homogeneously labeling the meal to be ingested with a Gadolinium (Gd)-based
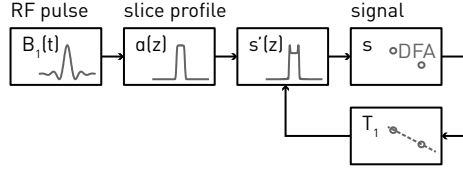
Figure 3.3 *Schematic flowchart describing the slice profile correction. After calculating the slice profile of the applied RF pulse, T_1 is updated based on the corresponding steady-state signals of the DFA acquisition. This is repeated until convergence is reached.*

paramagnetic contrast agent (CA), the concentration of gastric secretion can be determined in vivo by dynamically detecting the changes in CA concentration by measuring changes in T_1. The interrelationship between the CA-concentration C_{CA} and T_1 is given by [67],

$$\frac{1}{T_1} = \frac{1}{T_{10}} + r_1 C_{CA} \, , \tag{3.15}$$

where r_1 is the relaxivity of the CA and T_{10} the relaxation time of the meal in the absence of CA. While traveling down the GI tract, the diluted meal is exposed to constant change in the GI environment in terms of temperature, pH and macromolecular content and hence, both parameters are also subject to constant change. In particular, it has been shown that for liquid meals within the gastric environment, r_1 and T_{10} can be modeled as a function of C_{CA}, which yields in the modified interrelationship [25],

$$\frac{1}{T_1} = \frac{1}{a\,C_{CA} + b} + (c\,C_{CA} + d)\,C_{CA} \, , \tag{3.16}$$

where the four parameters a, b, c and d can be empirically derived in an in vitro experiment. In this experiment, T_1 values are measured in the serial dilution of the meal at the corresponding C_{CA} values and a nonlinear least squares fit is performed to estimate the four parameters.

The dependency between T_1 and gastric secretion concentration is

finally given by,

$$\text{secretion concentration }[\%] = 100\% \cdot \frac{C_{CA}}{C_{CA0}}\ , \tag{3.17}$$

where C_{CA0} is the initial C_{CA} of the undiluted meal. This in vitro relationship between secretion concentration and C_{CA} is applied as a calibration curve for the related in vivo measurements.

3.2   Water-fat separation

Protons in different environments can resonate at slightly different frequencies. This frequency difference is known as chemical shift, which is described by a dimensionless parameter δ given in ppm. Although the largest source of ^{1}H MR signal arises from protons bound in water ($\delta = 4.7$ ppm), many organic compounds in the human body have different chemical shifts. Body fat is one dominant source. Compared to water, the complex structure of triglyceride molecules results in complex chemical shifts within the fat molecule, which gives rise to a fat spectrum with more than one spectral peak. In literature, the chemical shift of fat is often found to be $\delta \approx 1.2$ ppm, which corresponds to the highest spectral peak of fat arising from the methylene group. This single-peak assumption is a coarse approximation for the fat spectrum, accounting only for 70% of the total fat protons [68].

Chemical shifts can be detected using magnetic resonance spectroscopy (MRS) and MRI. MRS has long been considered the gold standard for measuring tissue fat content but with the rise of improved imaging techniques for water-fat separation, imaging has become an alternative to MRS for accurate quantification of proton density fat fraction [69]. However, especially at very low fat contents, an adequate performance of imaging techniques remains challenging and spectroscopic methods are the preferred choice.
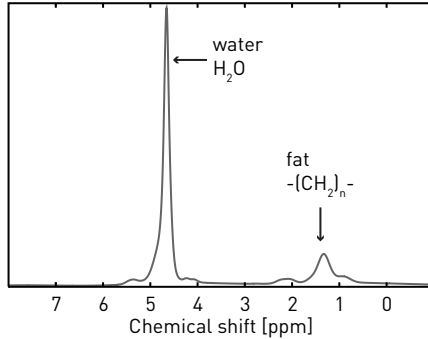
Figure 3.4 *A representative spectroscopic spectrum of a fat emulsion with the two main peaks from water (4.7 ppm) and methylene groups in fat (1.2 ppm).*

3.2.1   Spectroscopy

In MRS, the abundance of different molecules in tissue, not their spatial distribution is usually measured. The output of MRS is therefore a collection of peaks at different chemical shifts, the spectrum, which represents protons in different chemical environments. Figure 3.4 shows an example of a fat emulsion spectrum. Point resolved spectroscopy (PRESS) and STEAM are widely used single-voxel techniques for the localized measurement of spectra with spatial tissue excitation. In general, high signal-to-noise ratios (SNRs) are achieved with short TEs, which allows the detection of an increased number of metabolites. For TR, it is beneficial to choose large values in order to limit a T_1 weighting of the spectrum. This is especially of interest, if absolute quantification of the measured spectral peaks is attempted. For quantification, the sequence is usually repeated at multiple TEs in order to estimate T_2 values and subsequently remove the T_2 weighting of the peaks [69, 70]. Fat quantification with MRS has been successfully applied to fat emulsions for the study of intragastric fat fraction [71]. In addition, MRS is often employed to measure and precalibrate the multi-peak fat spectrum to be used for imaging approaches.

3.2.2 Dixon

In a gradient echo imaging sequence, the chemical shift invokes phase accumulation during the readout gradient G_x. This modulates the acquired signal phase at readout for a specific TE according to,

$$\phi(t) = -2\pi k_x(x + \delta B_0/G_x) - \gamma \delta B_0 \text{TE}\,, \tag{3.18}$$

where k_x is the k-space dimension in readout direction and B_0 is the magnetic field strength. The first summand introduces a chemical shift artifact in the readout, causing a spatial shift in the image along readout direction. The second summand introduces an additional phase of the signal. If water is excited onresonant, the chemical shift of fat becomes $\delta = -3.5$ppm under the assumption of a single-peak fat model. In this simple case, the total signal can be expressed in terms of the offresonance frequency $\Delta\omega = \gamma \delta B_0$ as,

$$s(\text{TE}) = W + Fe^{-j\Delta\omega \text{TE}}\,, \tag{3.19}$$

where W and F are the signals from the water and fat protons in each voxel, respectively. The proton density fat fraction is defined as,

$$\text{ff} = \frac{F}{W + F}\,. \tag{3.20}$$

Chemical shift-based water-fat separation was introduced by the Dixon technique [72]. Two images are acquired at two different $\text{TE}_{1,2}$ chosen in such a way that the first image, i.e. in-phase image, is acquired with water and fat in zero-phase and the second image, i.e. out-of-phase image, is acquired with water and fat 180° out of phase, respectively. The resulting signals $s(\text{TE}_1)$ and $s(\text{TE}_2)$ are given by,

$$s(\text{TE}_1) = W + F\,, \tag{3.21}$$

$$s(\text{TE}_2) = W - F\,. \tag{3.22}$$

Water and fat can then be separated by,

$$W = \frac{1}{2}\big(s(\mathsf{TE}_1) + s(\mathsf{TE}_2)\big)\,, \tag{3.23}$$

$$F = \frac{1}{2}\big(s(\mathsf{TE}_1) - s(\mathsf{TE}_2)\big)\,. \tag{3.24}$$

Based on this simple concept, many variants have been implemented with two or three TEs.

3.2.3 IDEAL

Although the Dixon technique is satisfactory for many applications, it faces the major challenges of water-fat separation, which are B_0 inhomogeneity, T_2^* decay, the spectral complexity of the fat, noise and T_1 bias. These challenges present confounding factors that need to be addressed for accurate fat quantification. A recent approach is the iterative decomposition with echo asymmetry and least squares estimation (IDEAL) [73], which allows an asymmetric choice of TEs and corrects for B_0 inhomogeneity by iteratively calculating the field map. Further improvements were made in [74], which accounts for T_2^* by estimating a complex field map instead of a real-valued one and incorporates a multi-peak spectral fat model. The complex field map is given by,

$$\hat{\psi} = \gamma B_0 + j\frac{1}{T_2^*}\,. \tag{3.25}$$

The P-peak fat model is mathematically given by the weighted sum of exponentials, described by the relative amplitude β_p and offresonance frequency $\Delta\omega_p$ of the p-th peak. With these definitions, a more complex signal model than the one given in Eq. 3.19 can be expressed as,

$$s(\mathsf{TE}) = \Big(W + F\sum_{p=1}^{P}\beta_p e^{-j\Delta\omega_p\mathsf{TE}}\Big)e^{-j\hat{\psi}\mathsf{TE}}\,. \tag{3.26}$$

Since nonlinear curve fitting needs to be performed for Eq. 3.26, IDEAL
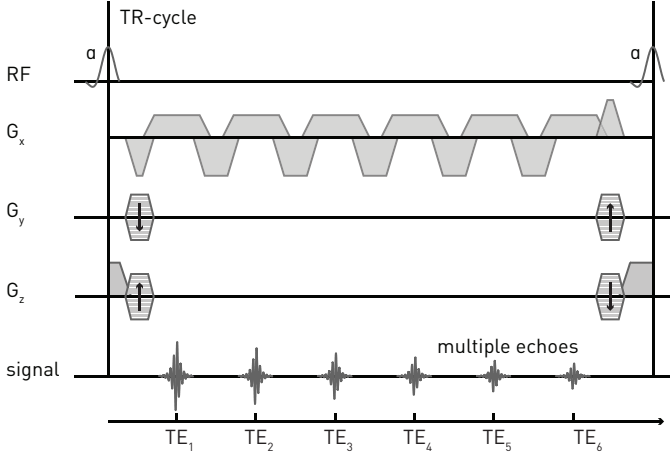
Figure 3.5 *Pulse sequence scheme of IDEAL using a multi-echo gradient echo sequence and flyback gradients for an unipolar readout.*

is usually used in conjunction with more than three echoes. Typically, a multi-echo gradient echo sequence, e.g. with six echoes, and unipolar gradients is applied as depicted in Figure 3.5. For a group of M echoes measured at specific TEs, TE_m $(m = 1, \cdots M)$, the signal model can be rewritten in matrix form,

$$\boldsymbol{s} = \boldsymbol{D}(\hat{\psi}) \, \boldsymbol{A} \begin{bmatrix} W \\ F \end{bmatrix} , \qquad (3.27)$$

where $\boldsymbol{s} = [s(\mathsf{TE}_1) \, s(\mathsf{TE}_2) \cdots s(\mathsf{TE}_M)]^T$,

$$\boldsymbol{D}(\hat{\psi}) = \begin{bmatrix} e^{-j\hat{\psi}\mathsf{TE}_1} & 0 & 0 \\ 0 & \ddots & 0 \\ 0 & 0 & e^{-j\hat{\psi}\mathsf{TE}_M} \end{bmatrix} \text{ and } \boldsymbol{A} = \begin{bmatrix} 1 & \sum_{p=1}^{P} \beta_p e^{-j\Delta\omega_p\mathsf{TE}_1} \\ \vdots & \vdots \\ 1 & \sum_{p=1}^{P} \beta_p e^{-j\Delta\omega_p\mathsf{TE}_M} \end{bmatrix} .$$

In the IDEAL algorithm [75], $\hat{\psi}$ is estimated first. The corresponding phase shifts arising from matrix $\boldsymbol{D}(\hat{\psi})$ are then demodulated from the acquired signal by exploiting the property $\boldsymbol{D}^{-1}(\hat{\psi}) = \boldsymbol{D}(-\hat{\psi})$. Final estimates

of W and F are obtained by performing the Penrose-Moore pseudoinverse,

$$\begin{bmatrix} W \\ F \end{bmatrix} = (\boldsymbol{A}^H \boldsymbol{A})^{-1} \boldsymbol{A}^H \boldsymbol{D}(-\hat{\psi})\boldsymbol{s} \,, \tag{3.28}$$

where superscript H is the complex Hermitian transpose operator.

3.3   Acceleration

In MRI, resolution and scan duration are key parameters and of particular concern in GI applications where fast imaging is necessary to meet breath hold constraints. In order to accelerate image acquisition, it is possible to choose from a large variety of techniques, which utilize the fact that images have spatial and temporal redundancy [76]. Acceleration is achieved by reducing the density of spatial frequencies in k-space and hence, this principle is also referred to as undersampling.

3.3.1   Image reconstruction

The acquired MR signal is a complex-valued signal of the excited imaging volume V. It can be written as the Fourier transform of the imaged object $i(\boldsymbol{x})$ at position $\boldsymbol{x}$, weighted with the receive coil sensitivity $c(\boldsymbol{x})$ according to,

$$d(\boldsymbol{k}) = \int_V c(\boldsymbol{x})i(\boldsymbol{x})e^{-j2\pi \boldsymbol{k}\boldsymbol{x}}d\boldsymbol{x} \,. \tag{3.29}$$

The imaging principle can also be expressed in matrix form,

$$\boldsymbol{d} = \mathcal{F}\boldsymbol{S}\boldsymbol{i} = \boldsymbol{E}\boldsymbol{i} \,, \tag{3.30}$$

where $\boldsymbol{E} = \mathcal{F}\boldsymbol{S}$ is the encoding matrix, which comprises the Fourier transform $\mathcal{F}$ and the coil sensitivities $\boldsymbol{S}$. The inverted process of Eq. 3.30 is the reconstruction of the image from the measurements using the reconstruction matrix $\boldsymbol{F}$,

$$\boldsymbol{i} = \boldsymbol{F}\boldsymbol{d} \,. \tag{3.31}$$

The presence of noise adds uncertainty to the acquisition in Eq. 3.30 and reconstruction can then be expressed as a minimization problem,

$$\arg\min_{\boldsymbol{i}}\|\boldsymbol{E}\boldsymbol{i} - \boldsymbol{d}\|_2^2\,. \tag{3.32}$$

If including prior information about the expected image, small entries in the inversion process can be avoided and accordingly, excessive noise amplification can be reduced. For example, a Tikhonov regularization improves stability of reconstruction, which corresponds to the minimization problem,

$$\arg\min_{\boldsymbol{i}}\|\boldsymbol{E}\boldsymbol{i} - \boldsymbol{d}\|_2^2 + \lambda\|\boldsymbol{i}\|_2\,, \tag{3.33}$$

where the regularization parameter λ determines the weight of the prior information relative to the required data consistency constraint in Eq. 3.32.

Since the sampling of k-space is at discrete points, different trajectories can be designed to cover k-space. The most popular k-space trajectory is Cartesian sampling in which one line in k-space corresponds to one readout with a specific phase-encoding gradient. Since this results in parallel, equidistant k-space lines, the fast Fourier transform (FFT) can directly be applied as $\mathcal{F}$.

As in all discrete sampling applications, the Nyquist theorem needs to be fulfilled. Therefore, a fully sampled k-space necessitates the acquisition of a sufficient number of samples. Otherwise, if the undersampled k-space is left uncompensated, the reconstruction problem becomes underdetermined and signal aliasing occurs, which appears as fold-over artifacts in the reconstructed image. The degree of undersampling is defined by the acceleration factor R as the ratio of samples in the fully sampled case to the actually acquired ones.

3.3.2   Parallel imaging

In parallel imaging (PI), image reconstruction of the undersampled k-space can be compensated for by measuring with multiple receive coils.

In traditional sensitivity encoding (SENSE) reconstruction [77], image reconstruction is considered as a linear problem, where the encoding matrix $\boldsymbol{E} = \boldsymbol{\mathcal{F}}_u \boldsymbol{S}$ contains the undersampled Fourier transform operator $\boldsymbol{\mathcal{F}}_u$. Assuming the number of independent coils N_c to be larger than R, image reconstruction reads,

$$\boldsymbol{i} = (\boldsymbol{E}^H \boldsymbol{\psi}^{-1} \boldsymbol{E})^{-1} \boldsymbol{E}^H \boldsymbol{\psi}^{-1} \boldsymbol{d} \,, \tag{3.34}$$

where $\boldsymbol{\psi}$ is the noise covariance matrix, which accounts for coupling of the coils.

SENSE performs reconstruction directly in the image domain as given in Eq. 3.34, whereas other PI approaches such as GRAPPA are performed in the k-space domain [78]. Another way to classify the various PI techniques relates to the process of measuring $\boldsymbol{S}$. With SENSE it is obtained explicitly in a separate pre-scan. However, implicit approaches such as using auto-calibration have been implemented as well.

In general, the quality of the reconstructed accelerated images depends on the orthogonality of the spatial sensitivities of the receive coils. The influence of the coil geometry results in a spatially dependent noise enhancement, which is described by the geometry factor g_x for a voxel at location x,

$$g_x = \sqrt{(\boldsymbol{E}^H \boldsymbol{\psi}^{-1} \boldsymbol{E})_{x,x} (\boldsymbol{E}^H \boldsymbol{\psi}^{-1} \boldsymbol{E})_{x,x}^{-1}} \geq 1 \,. \tag{3.35}$$

Accordingly, the SNR of the reconstructed image reflects the following proportionality,

$$\mathrm{SNR}_x \propto \frac{1}{g_x \sqrt{R}} \,. \tag{3.36}$$

3.3.3   Compressed sensing

Like PI, compressed sensing (CS) aims to reconstruct undersampled images. While PI in general does not require prior information about the object to be imaged, CS exploits the fact that objects are sparse [79]. Sparsity refers to the image property where only a subset of all entries
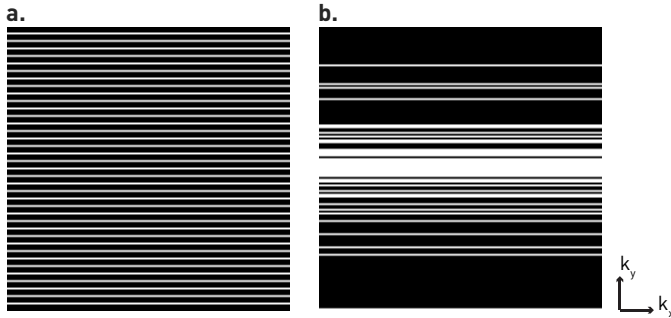
Figure 3.6 *Undersampling patterns in Cartesian space of $R = 4$ with a (a) uniform scheme and (b) variable-density scheme. Acquired sampling lines are shown in white whereas omitted ones are shown in black.*

in i are different from zero or noise. Since this property is not directly fulfilled by MR images, they need to be sparsified into a suitable transform domain such as the Wavelet domain [80]. Image reconstruction in CS usually employs the l_1-norm to address sparsity, which yields the convex minimization problem,

$$\arg\min_{i}\|\boldsymbol{Ei} - \boldsymbol{d}\|_2^2 + \lambda\|\boldsymbol{\Psi i}\|_1, \qquad (3.37)$$

where $\boldsymbol{\Psi}$ represents the sparsifying transform operator. The nonlinear minimization problem can be solved iteratively using the conjugate gradient (CG) [79] or iterative shrinkage thresholding (IST) [81] algorithm. Additional penalty terms may be introduced to Eq. 3.37 such as a variational constraint to enforce piece-wise constant images using total variation [82], i.e. $\lambda_{TV}\text{TV}(\boldsymbol{i})$. In dynamic cardiac image series, temporal redundancy of the time frames can be exploited in the frequency domain using the time-sparsifying operator $\boldsymbol{\Psi}_t$, i.e. $\lambda_t\|\boldsymbol{\Psi}_t(\boldsymbol{i})\|_2^2$.

Besides sparsity, an essential requirement of CS is the incoherence of aliasing effects. This can be well addressed by using random undersampling patterns in k-space such as the variable-density sampling scheme instead of a uniform undersampling pattern as depicted in Figure 3.6.

3.3.4   Dictionary-based reconstruction

The use of signal model-based dictionaries has recently gained interest as an alternative to CS-based image reconstruction. Instead of assuming sparsity using a fixed, global sparsifying transform, dictionary-based approaches tailor the sparsifying transformation to a specific class of images or anatomical configurations, which potentially offers image reconstruction of improved quality.

In the classical patch-based use of dictionaries, it is assumed that local image features can be described by a set of patches in a sparsifying dictionary [83–85]. The dictionary matrix $\boldsymbol{D}$ comprises all L entries or atoms of image patches in its columns. In each column, the length $n \times n$ of the vector corresponds to the patch size and defines the number of rows in $\boldsymbol{D}$. It is assumed that each patch $\boldsymbol{x}_i$ can be approximated by a linear combination $\boldsymbol{D}\boldsymbol{\alpha}_i$, where $\boldsymbol{\alpha}_i$ is the sparse representation of $\boldsymbol{x}_i$ in the transform domain. Reconstruction is achieved by solving the minimizaton problem,

$$\underset{\boldsymbol{i},\boldsymbol{\alpha},\boldsymbol{D}}{\arg\min} \sum_i \|\boldsymbol{R}_i\boldsymbol{i} - \boldsymbol{D}\boldsymbol{\alpha}_i\|_2^2 + \lambda\|\boldsymbol{E}\boldsymbol{i} - \boldsymbol{d}\|_2^2 \,\text{s.t}\, \|\boldsymbol{\alpha}_i\|_0 \leq T\,, \qquad (3.38)$$

where $\boldsymbol{R}_i$ is the operator for patch extraction and the l_0-norm is employed to encode sparsity at sparsity level T. Typically, Eq. 3.38 is solved using a two-step alternating minimization. In the dictionary learning step, $\boldsymbol{D}$ is trained using the K-SVD algorithm [86] and to determine $\boldsymbol{\alpha}_i$. In the reconstruction step, $\boldsymbol{i}$ is updated with a fixed $\boldsymbol{D}$ and $\boldsymbol{\alpha}_i$.

Dictionaries can also be useful for quantitative MR, which has been applied to the mapping of relaxation times [87–89]. In parameter mapping, multiple acquisitions, each measured at a different scan parameter value, are required, e.g. multiple FAs in T_1 mapping or multiple TEs in water-fat separation. The acquisition series spans a third encoding dimension similar to the time domain in dynamic image series. By applying prior knowledge along this dimension in the form of a signal model, sparsity can be enforced. Thus, the signal model-based use of dictionaries can

be interpreted as a variant of CS with sparsity applied in the parameter domain.

4 Multi-compartment effects in steady-state

4.1 Introduction

Non-balanced steady-state free precession (SSFP) sequences have proven useful for fast morphological and quantitative magnetic resonance imaging (MRI) [90]. Using appropriate gradient waveforms, individual transverse states of the magnetization can be selected, which allow the acquisition of magnetic resonance (MR) images with different contrasts. Double echo steady-state (DESS) imaging [91, 92] is an important variant of non-balanced SSFP sequences, which relies on the acquisition of the two lowest-order transverse states. The dependence of these states on quantitative MR parameters enables rapid parameter mapping in conjunction with water-selective pulses [93, 94]. In particular, the measurement of transverse relaxation times T_2 in the articular cartilage has been of major interest [95, 96]. More recently, the triple echo steady-state (TESS) sequence was introduced [97], which additionally acquires a third transverse state. Applications for T_2 quantification in cartilage have been demonstrated [98].

Articular cartilage consists of 65-80% water and the remainder of other molecules, including 10-15% of glycoproteins [99] and up to 4% of lipids [100]. It can be described as a mixture of different tissue compartments [101, 102], which may exhibit different T_1 and T_2 values due to water exchange or different off-resonant frequencies from susceptibility differences, partial volume effects or chemical shift. In the human body, another prevalent example of multi-compartment tissue is found in adipose

tissue and bone marrow where water and fat are the two main compart-
ments [103, 104]. The chemical shifts between the compartments could
induce phase offsets, which modulate the total signal of the transverse
states. Consequently, the assumption of a single-compartment model may
confound the accuracy of T_2 quantification. Therefore, off-resonance signal
modulations in the transverse states of non-balanced SSFP sequences
need to be considered.

The purpose of the present work was to investigate the effect of multi-
compartments on the MR signals in the TESS sequence without water-
selective pulses using simulations and in vitro measurements. The ac-
curacy of TESS for T_2 quantification in multi-compartment tissue was
assessed using in vitro phantom samples and in vivo experiments in the
knee. A novel approach to exploit the multi-compartment effect for fat
fraction quantification is demonstrated for monitoring fat digestion in the
stomach.

4.2 Theory

In non-balanced SSFP sequences, one longitudinal state and two trans-
verse states with complementary phase evolution (F_n, F_{-n}) are created
after each each radiofrequency (RF) pulse. In between two RF pulses, the
non-balanced moment induces dephasing and rephasing of the transverse
states. The gradient moment is designed such that the phase evolution of
the state increments by 2π within each repetition time (TR)-period, which
transforms previous F_n states into F_{n+1} [105]. This is written as,

$$F_n^+ \to F_{n+1} = E_2 F_n^+ \, , \qquad (4.1)$$

where superscript $+$ denotes the state immediately after the RF pulse and
$E_2 = \exp\left(-\text{TR}/T_2\right)$. Extended phase graphs [106] as depicted in Figure 4.1
visualize the phase evolutions. The F_0 state is rephased at the beginning
whereas the F_{-1} state is rephased at the end of each TR-period. A proper
design of the gradient switching pattern allows manipulation of the zero-
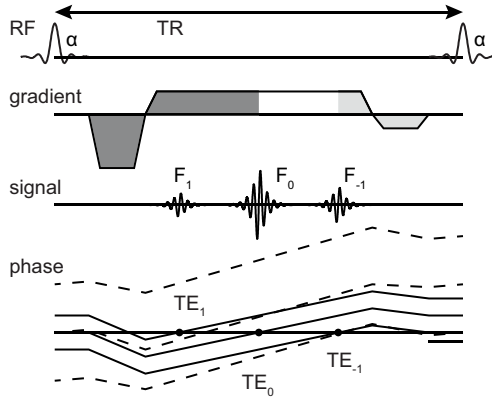
Figure 4.1 *Sequence diagrams and corresponding phase graphs of TESS. The white area of the gradient lobe reflects the non-balanced moment. The solid lines depict the phase evolution of the transverse states in the presence of the readout gradient waveform and on-resonance excitation, whereas the dashed lines depict phase evolution due to off-resonance. Note that the off-resonance is illustrated by the change in the slope of the phase, while the different degrees of static dephasing are illustrated by the transverse states.*

crossings of transverse states in order to acquire selected transverse states. DESS exploits the F_0 and F_{-1} states at respective echo times (TEs) of TE1 and TE1+dTE, where TE1 is the first echo time and dTE is the echo spacing. TESS exploits the three states F_1, F_0 and F_{-1} at respective TEs of TE1, TE1 + dTE and TE1 + 2dTE. Their corresponding signal intensities can be derived according to [107, 108].

If the tissue exhibits an off-resonant frequency $\Delta\omega$ due to e.g. chemical shift, the transverse states experience a phase shift. The evolution of the states in Eq. 4.1 becomes [109],

$$F_n^+ \rightarrow F_{n+1} = E_2 F_n^+ \cdot e^{i\Delta\omega \cdot \text{TR}} , \tag{4.2}$$

During readout, an additional phase offset ϕ_n is added to each transverse state F_n, which can be described as a function of TE_n and its initial phase at the beginning of the TR-period $\phi_{n,0}$ or as a function of the effective

echo time τ_n,

$$\phi_n = \Delta\omega \cdot \text{TE}_n + \phi_{n,0} = \Delta\omega\,\tau_n\,. \tag{4.3}$$

F_1 evolves from the previous F_0, which has accrued a phase offset according to Eq. 4.3 and hence, $\phi_{1,0} = \Delta\omega \cdot \text{TR} + 2\pi$. Analogously, $\phi_{-1,0} = -\Delta\omega \cdot \text{TR} - 2\pi$ holds for the inverted state. F_0 evolves from the rephased previous F_{-1} and therefore, the accrued phase is eliminated, $\phi_{0,0} = 0$.

Assuming symmetrical gradient timings, such that TR is 2TE1+dTE for DESS, the following relationships hold,

$$\tau_0 = \quad TE1\,, \tag{4.4}$$

$$\tau_{-1} = -TE1, \tag{4.5}$$

and therefore, the resulting signal phase depends on the choice of TE1 but is independent of dTE. For TESS, symmetrical gradient timings imply a TR of 2TE1+2dTE, resulting in the following relationships,

$$\tau_1 = 3\,TE1 + 2dTE\,, \tag{4.6}$$

$$\tau_0 = \quad TE1 + \quad dTE\,, \tag{4.7}$$

$$\tau_{-1} = -TE1\,. \tag{4.8}$$

In multi-compartment tissue where at least one compartment is excited off-resonance, the total signal is the complex sum of all compartment signals. As an example, we consider a two-compartment model with an on-resonance compartment W such as water and an off-resonance compartment F such as fat with a fat fraction ff. The signal intensities of their transverse states $s_{W,n} = F_n^W\,(1 - \text{ff})$ and $s_{F,n} = F_n^F\text{ff}$ are added to form the complex total signal,

$$s_n = s_{W,n} + s_{F,n} \cdot e^{i\phi_n}\,, \tag{4.9}$$

with corresponding magnitude signal,

$$|s_n| = \sqrt{s_{W,n}^2 + s_{F,n}^2 + 2s_{W,n}\, s_{F,n} \cos(\phi_n)}. \tag{4.10}$$

As seen from Eq. 4.10, the summation of off-resonant compartments induces periodical, sine-like modulations of the measured signal. The modulations are a function of ϕ_n and consequently of TE. The frequency of these periodical modulations varies for the different states and imaging sequences (Eq. 4.4-4.8), whereas the amplitude of the modulations is dependent on ff.

When employing a more realistic fat model using more than one spectral fat peak, Eq. 4.9 becomes,

$$s_n = s_{W,n} + s_{F,n} \cdot \sum_{p=1}^{P} \beta_p e^{i\Delta\omega_p \tau_n}, \tag{4.11}$$

where β_p is the relative amplitude and $\Delta\omega_p$ is the off-resonance frequency of the p-th peak of the underlying P-peak spectral fat model.

4.3   Methods

4.3.1   Simulations of the multi-compartment effect

Multi-compartment DESS and TESS magnitude signals were simulated for 1.5T using Eq. 4.11 with the signal intensities of the individual transverse states F_n computed according to the expressions given in [96, 97]. Different tissue scenarios were modelled at various TEs: (a) single-compartment tissue; (b) two-compartment tissue, chemical shift 3.5 ppm, ratio fat:total 1:20; (c) two-compartment tissue, chemical shift 3.5 ppm, ratio fat:total 1:10 and (d) multi-compartment tissue. For the off-resonance compartment, an 8-peak spectral fat model according to [110] was used. Signals were generated by varying TE1 between 3 and 6 ms while fixing dTE at 3 ms and by varying dTE between 3 and 6 ms while fixing TE1 at 3 ms. An increment of 0.2 ms was used for the variations.

4.3.2   Phantom and in vivo experiments

In vitro, an emulsion of water and rapeseed oil was produced with 20 wt% fat according to [110]. The emulsion was diluted with the appropriate volumes of water to generate a set of phantom samples that matched the four scenarios: (a) water; (b) emulsion with 5 wt% fat; (c) original emulsion with 10 wt% fat and (d) pure rapeseed oil. For T_2 quantification, a second set of the same phantom samples with shortened relaxation times was prepared by doping the emulsion with Gd-DOTA (DOTAREM®, Guerbet, France). A third in vitro experiment was performed with ten phantom samples consisting of 0, 2.5, 5, ..., 17.5, 20 and 100 wt% fat.

Experimental data were acquired on a 1.5 T whole-body MRI scanner (Achieva, Philips Healthcare, Best, the Netherlands) with a 4-channel abdominal phased array coil (Philips Healthcare, Best, the Netherlands). The scan parameters for the TESS acquisitions were: flip angle 15°, field of view (FOV) 100x100x30 mm^3, voxel size 1.0x1.0x3.0 mm^3, bandwidth 433 Hz/voxel. The acquisitions were repeated for a range of TEs by varying dTE between 3.2 and 4.8 ms while fixing TE1 at 3 ms or 3.6 ms. The minimum TR was chosen for each TE and ranged from 10.6 to 18.1 ms. For the set of doped samples, a single slice from a spin echo (SE) sequence was acquired as reference. Scan parameters were: TR 5000 ms, ten TEs ranging from 10 to 100 ms and otherwise identical parameters.

The in vivo study was approved by institutional and local ethics committees (Cantonal Ethics Commission Zurich). Sagittal and axial human knee images were acquired with TESS and SE using a knee coil and following scan parameters: FOV 200x200x30 mm^3, voxel size 0.9x0.9x3.0 mm^3 and otherwise identical parameters as in vitro. TESS acquisitions were obtained by varying dTE between 3.2 and 4.8 ms while fixing TE1 at 6.3 ms with three averages and a duration of 2-3 minutes each. An increment of 0.4 ms was used for the variations.

For T_2 quantification, a pixelwise iterative minimization procedure was employed for TESS as described in [97]. Based on the signal ratios of the transverse states, T_2 maps were fitted to a single-compartment model.

T_2 maps of the acquired SE images were generated by a pixelwise fitting procedure.

Magnitude images of the transverse states and the corresponding T_2 maps were analyzed. To this end, mean ± standard deviation values were calculated in region of interests (ROIs). In vitro, ROIs were positioned within the bottles of the phantom samples. For the in vivo data, ROIs were placed in posterior cartilage, muscle, bone marrow and visceral fat.

4.3.3   Fat fraction quantification

When acquiring the transverse states at more than one TE, more mea-surements are available for the subsequent fitting procedure. This po-tentially allows to take advantage of the multi-compartment effect by in-corporating a signal model with two or more compartments. Such an approach was investigated in vitro for the estimation of the fat-fraction in water-fat tissue using the third set of phantom samples. To test the in vivo feasibility of the approach, additional in vivo images of the stomach were acquired after intake of the emulsion described in the previous section as a test meal. The images were acquired in one breath hold each to account for respiratory motion. For fat fraction mapping two-dimensional (2D) TESS acquisitions were acquired using a sinc-shaped RF pulse with a time-bandwidth product of 10.02. The two TEs that captured the largest variation in the amplitudes of the sine-like signal modulation were chosen. With the choice of TE1 of 3.2 and 3.8 ms, dTE of 3 ms, the minimum and maximum of the modulation of the F_1 state was captured. Since the signal model according to Eq. 4.11 was nonlinear, a fitting procedure using a dictionary containing possible simulated signal intensities was used. The orthogonal matching pursuit (OMP) algorithm [111] was implemented to search for the fat fraction value with the closest match between the measurements and the dictionary entries in order to generate quantitative fat fraction maps. A detailed description of this process is given in Appendix B.

4.4   Results

For single-compartment tissue, the signal of all transverse states revealed slowly and little varying intensities and no major dependence on the chosen TEs in both simulation and measurement. This is demonstrated in Figure 4.2a, where the acquired states of TESS in water are depicted as a function of dTE. For tissue with more than one compartment, a dependency on TE is observed, which becomes stronger with increasing fat fraction (Figure 4.2b-d). For the two-compartment scenarios, the signal of the transverse states exhibited periodical signal modulations. As expected, the fat fraction determined the amplitude of the modulation, while TE controlled the frequency of the modulation. For TESS, only the F_{-1} state was independent of dTE (Eq. 4.8). The other two states showed a dependence on both TE1 and dTE with different oscillation frequencies and reached maximum amplitude whenever $\tau_{0,1}$ (Eq. 4.6-4.7) was multiple of the in-phase time, resulting in a constructive summation of their compartments (Eq. 4.9). The highest frequency occurred for the F_1 state, i.e. with a frequency of 1/(3TE1+2dTE) (Eq. 4.6). The multi-compartment scenario exhibited more complex signal modulations, since it constituted the sum of all compartment modulations, each with a different frequency due to different off-resonances. The simulated and measured signal intensities using the multi-compartment model were in excellent agreement. The corresponding behavior as a function of TE1 is depicted in Figure A.1. The corresponding DESS transverse states are given in Appendix C and Figure A.2.

The signal modulations induced by the multi-compartment effect confounded the T_2 quantification using TESS. T_2 values for the scenarios of the simulations and measurements are given in Figure 4.3a-b. The single-compartment scenario exhibited adequate T_2 estimation for different TEs. The T_2 values of the multi-compartment solutions exhibited signal modulations, which depended on the choice of TE and varied with varying fat fractions. Even at a relatively low water-fat ratio of 1:20, deviations could
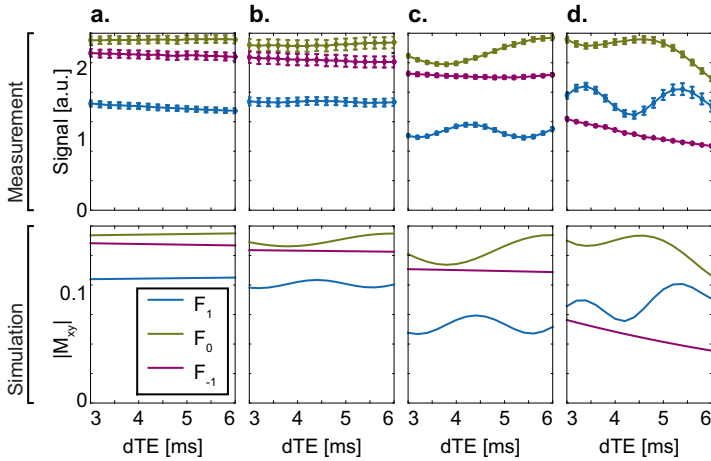
Figure 4.2 *Behavior of TESS transverse states as a function of dTE (TE1 = 3 ms) in simulations and measurements. (a) Single-compartment scenario using water; (b) two-compartment scenario using a 5 wt% emulsion; (c) two-compartment scenario using a 10 wt% emulsion and (d) multi-compartment scenario using pure fat. Upper and lower panels show the agreement between measurement and simulation.*

be observed.

In the in vivo measurements, the erroneous T_2 offsets observed in the phantom samples could also be seen. Figure 4.4 displays TESS transverse states and T_2 maps of the knee using the SE reference sequence and TESS at two different TEs. In Figure 4.3c, the estimated T_2 values are given, obtained within ROIs positioned in posterior cartilage, muscle, bone marrow and visceral fat. T_2 values of muscle derived from TESS caused variations depending on the choice of echo spacing of 12%. Tissues with a more pronounced multi-compartment nature exhibited larger variations: 28% for cartilage, 42% for bone marrow and 36% for visceral fat.

Figure 4.5a-b shows the estimated fat fraction maps based on TESS acquisitions at two different TEs. Linear regression showed a strong correlation between the expected fat content of the emulsions and the estimated fat fraction values with a slope of 0.97 and an intercept of -0.32 ($r^2 = 0.999$). In vivo, the estimated fat fractions allowed monitoring of the fat content in
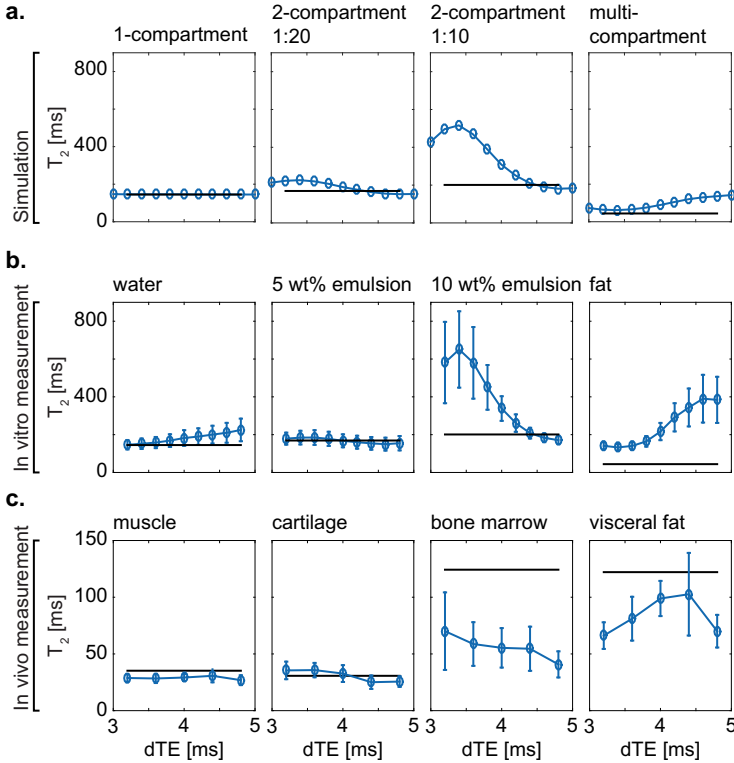
Figure 4.3 *Behavior of T_2 values as a function of dTE (TE1 = 3.6 ms) for the different scenarios and tissues. (a) simulations; (b) in vitro measurements and (c) in vivo measurements of the knee. Reference T_2 values of SE are depicted by the black line.*

the stomach. After 120 minutes, a lower fat content could be observed in the stomach (Figure 4.5c).

4.5   Discussion

In this work, we demonstrated that tissues with multiple compartments of different chemical shift affect the signal intensities of the transverse states in non-balanced SSFP. The contributions of the off-resonant compartments to the total signal intensity induced periodical signal modula-

a.

b.
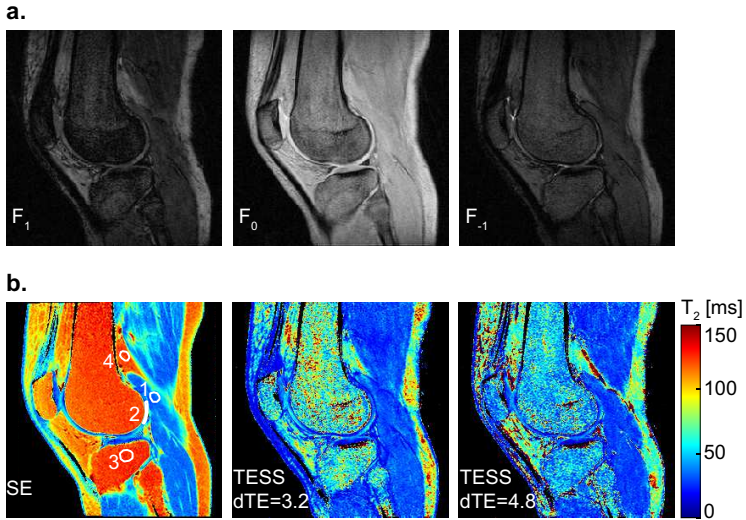
Figure 4.4 *Sagittal human acquisitions of the knee, (a) TESS transverse state images F_1, F_0 and F_{-1}. (b) T_2 maps of SE (left), TESS with dTE=3.2 ms (middle) and dTE=4.8 ms (right). The numbered ROIs depict in ascending order: muscle, posterior cartilage, bone marrow and visceral fat.*

tions dependent on the choice of TE causing inaccuracies in subsequent T_2 quantification. When applying a suitable multi-compartment model, these signal modulations can be leveraged, as was shown in vivo for the estimation of fat fractions inside the stomach.

Four scenarios were investigated, among which two were defined as two-compartment tissues. Strictly speaking, fat itself is already a multi-compartment tissue exhibiting multiple peaks of different chemical shift. However, since the considered compartment ratios were low, only the modulation of the largest fat peak (3.5 ppm chemical shift) significantly contributed to the observed modulation and therefore, their designation as two-compartment scenarios was considered well-suited.

In the case of T_2 quantification, potential estimation errors arise from the use of a single-compartment model when the presence of additional off-resonant compartments cannot be neglected. While the impact on T_2

a.

b.

c.

after 20 min.

after 120 min.

Fat fraction
100%

0%
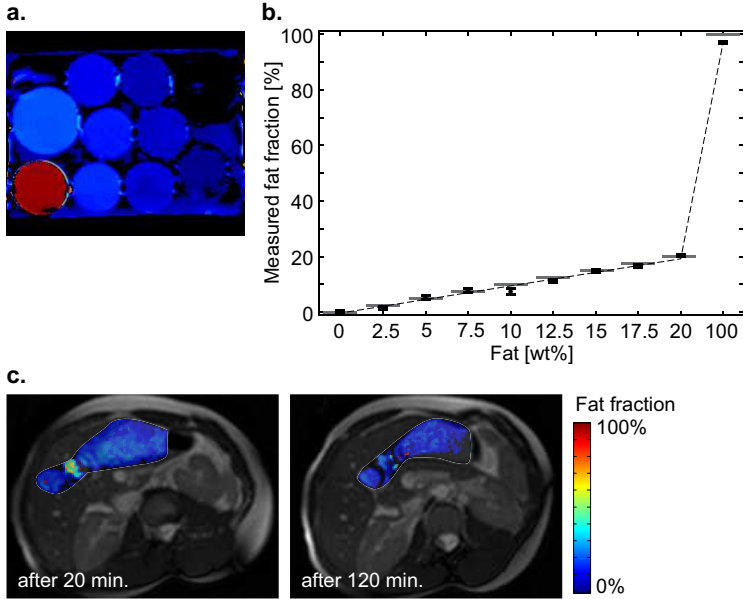
Figure 4.5 *(a) Reconstructed fat fraction maps of in vitro phantom samples and (b) corresponding estimates relative to the reference values. The gray horizontal lines depict the nominal fat fractions whereas the dashed line depicts the regression line; (c) reconstructed fat fraction maps of the stomach overlaid on top of the anatomical transverse image slice at two different time points after emulsion ingestion.*

was explicitly shown, the impact on T_1 quantification according to [97] is expected to be comparable, since its estimation is likewise based on the signal ratios of the transverse states.

Protons can be found in many organic compounds [112], with the most prevalent example being body fat. Simulations showed that it is possible to choose a TE such that the estimated T_2 value will be equal to the T_2 value of the water compartment only, e.g. TE1 = 3.6 ms and dTE = 4.2 ms. However, due to the different relaxation times of the compartments, the reference T_2 is a weighted result of the compartments' values, and the exact TE for most accurate T_2 quantification with regards to the reference cannot be determined in general. In our experiments, this resulted in a shift of dTE

towards larger values for larger fat fractions. Employing fat suppression schemes such as spectral-spatial excitation [113] is especially beneficial in musculoskeletal imaging [114], as it effectively eliminates the chemical shift artifact. Fat suppression schemes, however, are sensitive to B_0 and B_1 inhomogeneities. Especially in tissues where motion effects cannot be completely avoided, the decreased effectiveness of fat suppression schemes becomes problematic. In relatively static tissue which can be shimmed sufficiently such as the knee, which can be shimmed sufficiently, fat suppression has been successfully demonstrated [97, 115].

Prior knowledge about the different compartments may allow for an adjustment of the applied signal model. If data is acquired at more than one TE, multi-compartment parameters such as compartment ratios can potentially be estimated. Since the performance of the estimation is sensitive to the choice of TEs, an optimized sequence protocol must be used. For the presented fat quantification, the best performance was obtained when the minimum and maximum of the sine-like modulation of the F_1 state was chosen. It is speculated whether the presented approach for fat fraction quantification can also be applied to estimate other parameters. For example, the quantification of multi-exponential T_2 relaxation has already been investigated in articular cartilage using other sequences [101, 102, 116]. For its adaptation to non-balanced SSFP, further work is necessary.

Limitations of the present work include that experiments were performed only at 1.5T. The general results of this work are expected to translate to higher field strengths. However, higher field strengths such as 3 T might provide a more flexible choice on TEs due to double off-resonance frequencies. A second limitation is that the T_2 values of the phantoms were higher than those of the investigated in vivo tissues. Simulations showed that the multi-compartment effects are smaller for lower relaxation values but are still in the same order of magnitude. Also, the in vivo measurements did not include an actual analysis of the underlying cartilage tissue composition. Thus, only a qualitative statement of multi-compartment effects on in vivo cartilage tissue could be given.

4.6   Appendix

A   Figures
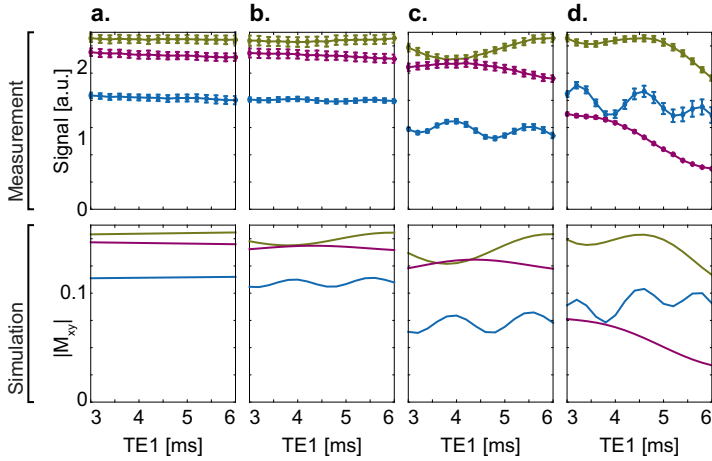
Figure A.1 *Behavior of TESS transverse states as a function of TE1 (dTE = 3 ms) in simulations and measurements. (a) Single-compartment scenario using water; (b) two-compartment scenario using a 5 wt% emulsion; (c) two-compartment scenario using a 10 wt% emulsion and (d) multi-compartment scenario using pure fat.*
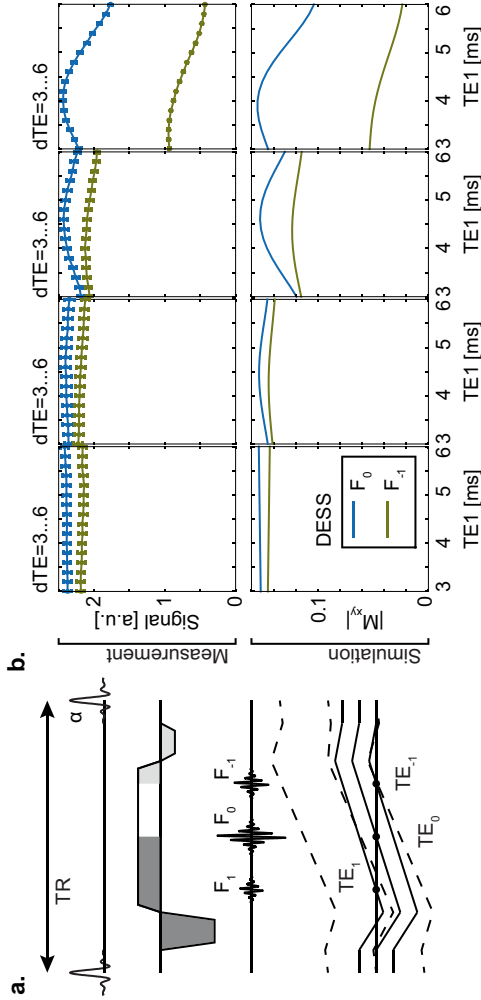
Figure A.2 *(a) Sequence diagrams and corresponding phase graphs of DESS. (b) Behavior of DESS transverse states as a function of TE1 (dTE = 3 ms) in simulations and measurements. From left to right: single-compartment scenario using water; two-compartment scenario using a 5 wt% emulsion; two-compartment scenario using a 10 wt% emulsion and multi-compartment scenario using pure fat. Upper and lower panels show the agreement between measurement and simulation.*

B Nonlinear fitting procedure

Relative fat and water ratios can be replaced in Eq. 4.11 by the fat fraction ff of the voxel and a normalization factor $a = F_n^W/(1-\mathrm{ff}) = F_n^F/\mathrm{ff}$,

$$s_n = a \cdot s_n' = a \cdot \left[F_n^W \cdot (1-\mathrm{ff}) + F_n^F \cdot \mathrm{ff} \cdot \sum_{p=1}^{P} \beta_p e^{i\Delta\omega_p \tau_n} \right]. \qquad (4.12)$$

Since F_n^W and F_n^F are dependent on the relaxation times of water and fat, respectively, s_n' can be regarded as a function of the three parameters ff, T_1 and T_2 of the water compartment, i.e. $s_n' = s_n'(\mathrm{ff}, T_1, T_2)$, assuming that the relaxation times of fat are known a priori. Relaxation times of fat were derived from measurements of rapeseed oil heated to body temperature, which mimics the state of emulsified fat within the stomach. Resulting values were $T_1 = 260\,\mathrm{ms}$ and $T_2 = 60\,\mathrm{ms}$ for the fat compartment.

By stacking the signals intensities of the three TESS states at two different TE acquisitions A and B, a 6-element vector is formed,

$$\boldsymbol{s}'(\mathrm{ff}, T_1, T_2) = \begin{bmatrix} s_{1,A}' & s_{0,A}' & s_{-1,A}' & s_{1,B}' & s_{0,B}' & s_{-1,B}' \end{bmatrix}^T. \qquad (4.13)$$

In order to generate the dictionary, $\boldsymbol{s}'(\mathrm{ff}, T_1, T_2)$ was simulated for a range of combinations of ff, T_1 and T_2. The different $\boldsymbol{s}'(\mathrm{ff}, T_1, T_2)$ are normalized and stacked horizontally, each forming one column in the dictionary matrix $\boldsymbol{D}$. This allows an alternative formulation of the signal intensities in vector form according to,

$$\boldsymbol{s} = \boldsymbol{D}\boldsymbol{\alpha} = \begin{bmatrix} \boldsymbol{s}'(\mathrm{ff}_1, T_{1,1}, T_{2,1}) \dots \boldsymbol{s}'(\mathrm{ff}_{L_1}, T_{1,L_2}, T_{2,L_3}) \end{bmatrix} \cdot \begin{bmatrix} \alpha_{111} \\ \vdots \\ \alpha_{L_1 L_2 L_3} \end{bmatrix}, \qquad (4.14)$$

where $\boldsymbol{\alpha}$ is the transform domain, and the parameters ff, T_1 and T_2 are discretized into the respective lengths L_1, L_2 and L_3. For ff, the full range from 0 to 100% was used. For T_1 and T_2, a range from 100 to 3000 ms and 100 to 2000 ms were chosen, respectively. Dictionary dimensions were

$L_1 = 101$, $L_2 = 30$ and $L_3 = 20$.

For $\boldsymbol{\alpha}$, only one nonzero entry is assumed as an approximation in order to maintain the stability of reconstruction. This entry selects the corresponding parameter combination and scales the dictionary atom to the non-normalized signal magnitudes of $\boldsymbol{s}$. The search for the best matching dictionary atom was implemented using the OMP algorithm (21), where the sparsity level was set to 1 in order to force only one nonzero entry in $\boldsymbol{\alpha}$.

C   Simulations and in vitro measurements for the DESS sequence

Experimental data were acquired using the same parameters as for the TESS sequence. Figure A.2 depicts the acquired states of DESS for the four in vitro scenarios as a function of TE1. Similar to the TESS behavior, the signal of the transverse states exhibited periodical signal modulations in the two-compartment scenarios. For DESS, modulations were only observed as a function of TE1, where both transverse states showed the same oscillation frequency (Eq. 4.4-4.5).

5 Gastrointestinal fat quantification

5.1 Introduction

In recent years, there has been a substantial increase in the number of reported nutrition-related diseases [117, 118]. Further, obesity – which is a major risk factor for these diseases – has become a global problem [119]. Diets that are high in fat have often been cited as a leading cause for obesity [9]. However, dietary fat remains an important source of essential fatty acids and plays a major role in the absorption of nutrients and pharmaceuticals [2–4]. Therefore, this has prompted an increase in research efforts to understand how food, particularly fat, is processed and digested within the gastrointestinal (GI) tract [120]. The physical state of fat has been demonstrated to affect the rate of fat digestion [71, 121]. Using fat emulsions, the in vivo physical state of fat can be adapted by careful design [19]. Therefore, there is keen interest from both physiological and product engineering perspectives in order to gain advanced insight into how fat is transformed during digestion and absorption [3, 32].

To date, there is a reasonable correlation between in vitro models and in vivo outcomes of fat nutrient sensing [2, 122–125]. These models together with extensive in vitro studies have generated a good understanding of how a controlled behavior of fat within the GI tract can influence both nutrient sensing and uptake in vivo [38, 126]. However, a complete and direct in vitro–in vivo correlation is often hindered by the limited understanding of how intraluminal processes such as emptying dynamics, trituration and inter-mixing with secretions impact the structure of ingested fat emulsions.

Therefore, a reliable and convenient method for the visualization of fat within the human GI tract is required. Magnetic resonance imaging (MRI) is a suitable technique meeting these requirements. MRI methods have been validated for both physiological and clinical measurements of GI function in health and disease states [54, 55]. Moreover, a small number of studies have demonstrated the feasibility of MRI to visualize the structural changes of lipid emulsions and their impact on gastric emptying and satiation [16, 17, 19, 127]. Further understanding can be provided by using quantitative MRI methods, which have been acknowledged to be of importance for food science and engineering [22–24, 128]. Indeed, relaxation mapping methods have already been utilized for the quantification of gastric secretion [65, 129–131]. The water–fat separation method, iterative decomposition with echo asymmetry and least squares estimation (IDEAL) allows for a robust separation of the magnetic resonance (MR) signal into its water and fat components [73, 74, 132]. Therefore, the IDEAL method can provide the visualization and quantification of spatial distribution of water and fat in vivo [133]. This enables fat fraction maps to be extracted – that is, images with quantitative information – contrasting the commonly applied qualitative fat-selective imaging strategies. This technique has not been applied to the GI tract so far, and thus is a potentially promising tool to study the spatial distribution and emptying dynamics of total intraluminal content alongside an independent measure of fat. This knowledge may ultimately offer deeper insights into the biophysics of gastric mixing and fat digestion. This in turn may provide the means to further bridge the gap between in vitro models and in vivo studies.

Therefore, the overarching aim of this study was to validate the non-invasive quantification of fat fraction in gastric and duodenal contents by MRI, utilizing the water–fat separation method IDEAL. To this end, two lipid emulsions with differing acid stabilities were utilized in order to quantify and assess the dynamic processing of fat within the stomach (phase separation and creaming) and duodenum in a randomized, cross-over, single-blinded study design.

	E1	E4
Fat fraction	20 wt% (liquid)	20 wt% (liquid)
Emulsifier	0.8 wt% polysorbate 80	1 wt% sodium caseinate 0.25 wt% monoglyceride
Mean particle size (D 4,3um)	0.33	0.38
Acid stable	yes	no
Redispersible	yes	yes

Table 5.1 *Composition and physical properties of the two fat emulsions.*

5.2   Methods

5.2.1   Fat emulsions

Two types of previously described and tested fat emulsions E1 and E4 were used in this study. The composition and properties of the emulsions are outlined in Table 5.1 [19]; they were prepared as described in Appendix B.

5.2.2   Fat fraction maps

In order to compute fat fractions based on chemical shift-induced signal variations, an accurate fat model of rapeseed oil was required. Therefore, a spectral multi-peak fat model of rapeseed oil was generated to quantify the fat peaks using a spectroscopic MR measurement on a 3-Tesla MRI scanner (Ingenia, Philips Healthcare). This fat model was used in the IDEAL reconstruction of all fat fraction maps (Figure A.1). All MRI data were acquired using a 1.5T MRI scanner (Achieva, Philips Healthcare), using an abdominal phased array coil (4-channel SENSE body coil; Philips Healthcare) with four elements. In order to acquire the fat fraction maps, IDEAL scans were performed with a multi-point echo sequence. The scanned data were then reconstructed by combining the multiple images acquired at the different echo times using the IDEAL approach [133]. In reconstruction, B0 field inhomogeneity, T2* decay and the multi-peak spectral fat model were

incorporated. After separating the data into water and fat images using the IDEAL reconstruction, the resulting fat fraction maps were obtained by calculating the ratio of the water and fat images.

5.2.3   Study design

Study population

This study was conducted according to the guidelines laid down in the Declaration of Helsinki, and all the procedures involving human subjects were approved by the Ethics Committee of the Canton of Zurich (KEK-ZH-Nr. 2014-0220); the trial was registered at ClinicalTrials.gov with identifier NCT02226029. Written informed consent was obtained from all subjects.

The present study was performed using a randomized, single-blinded, two-armed, cross-over study design. A total of twelve healthy subjects were recruited by advertisement. At an initial screening visit, subject eligibility criteria were assessed. Therefore, those invited to participate had neither current health problems nor a history of GI disease or abdominal surgery (excluding appendectomy or hernia repair). Subjects were also required to provide a negative pregnancy test (if applicable), have a body mass index (BMI) between 18 and 25 kg/m^2, be a non-regular smoker, aged between 18 and 50 years and have no contraindication to MRI. All the participants underwent MRI scans of 3 h on two different study days. During each study day, subjects were given one of the two emulsions. Assuming a standard deviation (SD) of 1.5% based on earlier data, we estimated that a total of twelve subjects would be needed to detect a difference of 2% fat fraction, with a defined power of 0.9. Two computer-generated, permuted blocks of twelve defined the randomization sequence for all subjects. Blinding of the subjects was ensured, as the emulsions had the same visual appearance.

Measurements

On the study day, subjects arrived in the morning at the MR center at the University Hospital Zurich after 8 h of fasting. A silicone nasogastric tube
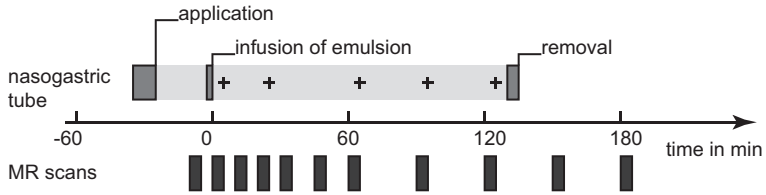
Figure 1 *Timeline of the study protocol. Exemplary gastric sampling time points are indicated by crosses.*

(Freka CH 12; Fresenius Kabi) was positioned in the gastric corpus through the nostril of the subject. The subjects were infused with 200 mL (1590 kJ (380 kcal)) of the emulsions within 1 min in order to control for the effect of inter-individual tolerance to texture and taste. End of infusion was taken as starting point t=0 min of gastric emptying. Subjects were positioned into the right decubitus in the MR scanner and were allowed to assume a sitting position outside the scanner during longer scan pauses. In these positions, intragastric gas accumulates in the fundus, which ensures a maintained rate of gastric emptying and distribution despite changes in body position [134]. The first MR image was acquired before meal infusion in order to obtain the volume of residual stomach content in the fasted state. All other MR images were acquired within scan blocks, which were performed at time points t=0, 10, 20, 30, 45, 60, 90, 120, 150 and 180 min, yielding ten blocks in total. Scans were performed during one breath-hold each, lasting from 5 to 34 s. Figure 1 shows the timeline of the study day.

Up to five samples of gastric content of 2 mL each were collected via the nasogastric tube between t=0 and 120 min. The aspirated gastric samples (Figure A.2) were used to obtain laboratory fat fractions in order to validate the fat fractions obtained using the MRI method IDEAL. After t=120 min, the nasogastric tube was removed. In each MRI scan block, four image types were acquired: IDEAL and volume scans were used for obtaining gastric and duodenal content volumes. Fat-selective scans yielded qualitative fat-selective images, which served as a comparator to the quantitative fat fraction maps. High-resolution volume scans were acquired in order to

determine the position of the nasogastric tube (Appendix C).

5.2.4   Fat fraction validation

In vitro

An in vitro validation of the fat fraction measurements obtained by IDEAL was performed. The emulsions were diluted to give a series of nine fat fraction samples between 0 and 20%. The samples were placed into plastic Falcon® tubes (Corning) and then simultaneously positioned in the MRI scanner to be measured by IDEAL. Mean fat fraction values were calculated within a region of interest (ROI) of 5×5 voxels for each sample and compared with the nominal fat fraction values by Lin's concordance correlation coefficient r_c [135].

In vivo

The fat fraction measurements provided by IDEAL were validated in vivo with nasogastric aspirates [136]. The tip of the catheter was first identified in the high-resolution volume scan, and then a ROI of 5×5 voxels was chosen at the appropriate position in the corresponding fat fraction map (Figure A.3). The fat fraction of the gastric samples was measured by gravimetric analysis. Each sample was first centrifuged at 4300 g for 5 min (Labofuge 400R; Heraeus Instruments) to enhance the phase separation between the emulsion and gastric juice. If possible, the clear gastric juice part was extracted from the gastric sample in order to minimize the contribution of residual particles to the resulting fat fractions. The weights of all samples and extracted gastric juice parts were determined. Subsequently, the samples were dried in a controlled environment and the weights of all samples were measured again after complete evaporation. Gastric samples that either developed mold during the drying process, contained solid particles or could not be identified in the MRI because of ambiguous detection of the nasogastric tip were excluded from the analysis. Laboratory fat fractions were calculated by obtaining the corresponding

weight ratios. IDEAL and laboratory fat fractions were compared against each other by r_c.

5.2.5   Data analysis

Fat distribution and emptying

A custom software tool written in MATLAB 2012b (The MathWorks) was used for image segmentation and related volume calculation. Gastric or duodenal total content volume (TCV), which are defined as content volumes without intraluminal air, were derived by semi-automatic segmenting of the content contours of each volume image [137]. Gastric or duodenal fat contents were obtained by applying the contours of the volume images to the fat fraction maps. Fat volume (FV) was calculated at each time point by weighting TCV with its corresponding average fat fraction value obtained from the fat fraction maps. Gastric and duodenal TCVs and their respective FVs were plotted over time to generate volume emptying curves.

Intragastric emulsion profiles

In order to assess creaming and phase separation of the ingested emulsions, intragastric fat fractions were averaged at each level along the direction of gravity as illustrated in Figure 2. Using these intragastric emulsion profile plots, the time point of maximum phase separation was defined by the occurrence of a maximum fat fraction (ff$_{max}$) in the stomach. A data-driven bi-phasic model (Appendix D) was fitted to these profiles in order to detect (1) the location of phase separation in the distal stomach (x_0), (2) the normalized extent of this phase separation $E = x_0/x_{stomach}$ and (3) the increase or gradient in the fat fraction towards the proximal stomach G (see again Figure 2). These parameters may be considered as surrogate markers for the degree of phase separation and creaming, respectively. The non-linear least-squares fit was performed in MATLAB 2012b.
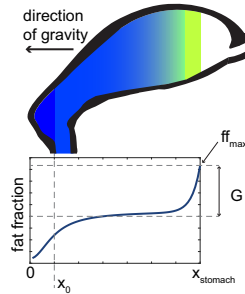
Figure 2 *Modeling of fat layering. Schematic to visualise the computed emulsion profiles and the applied model.*

Statistics

Statistical analyses were carried out using program R, version 3.1.3 [138]. The effects on fat emptying and emulsion profile were tested by linear mixed-effects models using function lmer of R package lme4 (version 1.1–7). The outcome measures TCV, FV and fat fraction were modeled with subject as a random effect. For the stomach, emulsion, time and fasted content volume (TCV-1) were used as fixed effects, whereas only emulsion was used as a fixed effect for the duodenum. The outcome measures ff_{max}, E and G were modeled with subject as a random effect and emulsion as a fixed effect. Model parameter estimates are presented with 95% confidence interval (CI).

5.3 Results

In total twelve subjects were included in the study for MRI measurements. MRI scans were successfully performed on all the twelve subjects (five men, seven women; mean age: 22.0 (SD 2.0) years; mean BMI: 21.9 (SD 1.5) kg/m^2). Gastric image data of three scan blocks and duodenal image data of seven scan blocks were missing because of technical errors. Nevertheless, gastric and duodenal volume curves were successfully determined in all subjects. The nasogastric tube, the emulsions and the
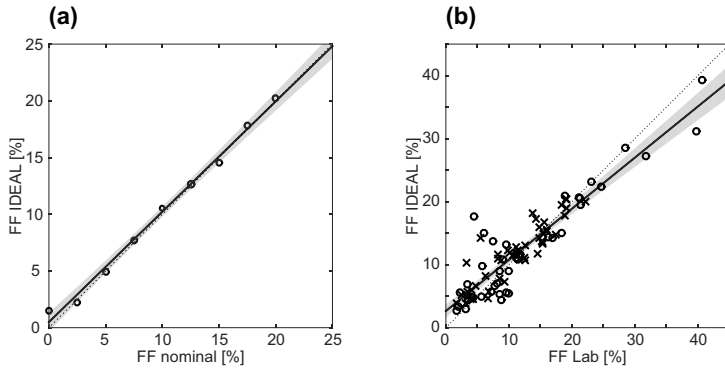
Figure 3 *In vitro and in vivo fat fraction validation. (a) Correlation plot showing the agreement between the in vitro experiment with iterative decomposition with IDEAL fat fractions and the nominal fat fractions. (b) Correlation plot showing the agreement between in vivo experiment with laboratory fat fractions and IDEAL fat fractions including data from E1 (crosses) and E4 (circles). Each plot depicts the line of identity (dashed line) and the linear regression fit (solid line) with 95% CI (gray area).*

breath-holds were well tolerated by all subjects.

5.3.1   Fat fraction validation

Figure 3(a) depicts the scatterplot of the in vitro MRI measurements (nine data points), which demonstrates the agreement between nominal fat fractions and fat fractions measured by IDEAL. Lin's concordance correlation coefficient was 1.00 (95% CI 0.98, 1.00). The laboratory fat fraction values from gastric content samples were determined from a total of eighty-eight included samples. In total twenty-seven samples were excluded from the analysis; Lin's concordance correlation coefficient was 0.91 (95% CI 0.87, 0.94). The agreement between the two measurement methods is presented in the scatterplot of Figure 3(b).

5.3.2   Fat distribution and emptying

Statistical analyses of emulsion profiles were performed only on those during the time point of maximum phase separation (twenty-four data

points). Statistical analyses on emptying were performed on 238 gastric and 233 duodenal observations.

Stomach

The different intragastric stability of the fat emulsions resulted in different structuring of intraluminal content. In the standard qualitative fat-selective images, this was indicated by changes in MR signal intensities, where higher fat contents resulted in brighter signals. Color coding was applied for the fat fraction maps, where blue and red indicated 0 and 100% fat fraction, respectively. A direct comparison between the two image types showed that they were in agreement with each other, both depicting the different dynamics of phase layering and revealing the different dynamics of fat structuring (Figure 4). However, inhomogeneity features such as fat fraction gradients and fat pockets could hardly be identified in the fat-selective images but were obvious in the fat fraction maps.

Typical fat distributions in the stomach of the acid-stable emulsion E1 and the acid-unstable emulsion E4 are depicted in the fat fraction maps in Figure 5(a). E1 largely maintained its stability throughout the 180-min scanning period. This is demonstrated by the gradual transition of the homogeneous gastric content to the deeper shades of blue, which represent lower fat fractions. Further, this indicates that gastric secretion was continuously released into the stomach and then mixed with gastric content. E4 underwent clear structural changes under gastric conditions, resulting in less homogeneous intragastric fat distributions. Shortly after meal infusion, E4 exhibited creaming, flocculation of fat and separation into two phases. This phase separation occurred as a region of higher fat content developing on top of the remaining gastric content. This bi-phasic fat distribution led to a faster emptying of the lower fat content phase present in the distal stomach. In a few subjects, re-emulsification of the flocculated fat could be observed in the image data.

These observations are nicely reflected in the emulsion profiles. The dynamics of phase separation, including the degree of flocculation and
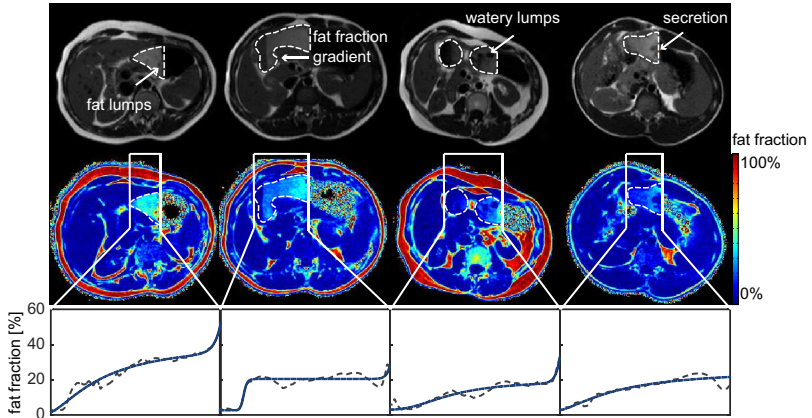
Figure 4 *Gastric content of E4 of four different subjects within the first 60 min. The qualitative fat-selective images (upper panel), the corresponding color-coded fat fraction images (middle panel) and emulsion profiles (lower panel) show the inter-individual variations in intragastric fat distributions. The dashed white curves outline the, intraluminal content. Although both image types are in good agreement with each other, features such as fat lumps or fat fraction gradients are less evident in the first image type. The measured (dashed line) and fitted (solid line) emulsion profiles reflect the differing extents of phase separation and creaming.*

subsequent re-emulsification, varied considerably between subjects, as can be observed in the image series of Figure 4.

Figure 5(a) shows the change in the intragastric fat fraction over time in one subject. Both the fat fraction maps and the emulsion profiles nicely reflected the different properties of E1 and E4. Individual emulsion profiles of E4 revealed large differences between the subjects as visualised in Figure 4. No creaming was observed for E1 with ff_{max} of 21.6 (95% CI 16.4, 26.4)% and G of 0.1 (95% CI –0.1, 0.2)%/mm. Creaming was stronger in E4 compared with E1, where ff_{max} was larger by 21.2 (95% CI 14.8, 28.1)% and G was larger by 0.2 (95% CI 0.04, 0.3)%/mm. The observed highest degree of creaming – that is, the upper range of ff_{max} – was 68% in E4. The extent of phase separation E for E1 was small with 0.1 (95% CI 0.0, 0.3); E4 showed values of E that did not differ compared with E1 (difference: 0.1 (95% CI 0.0, 0.3)).
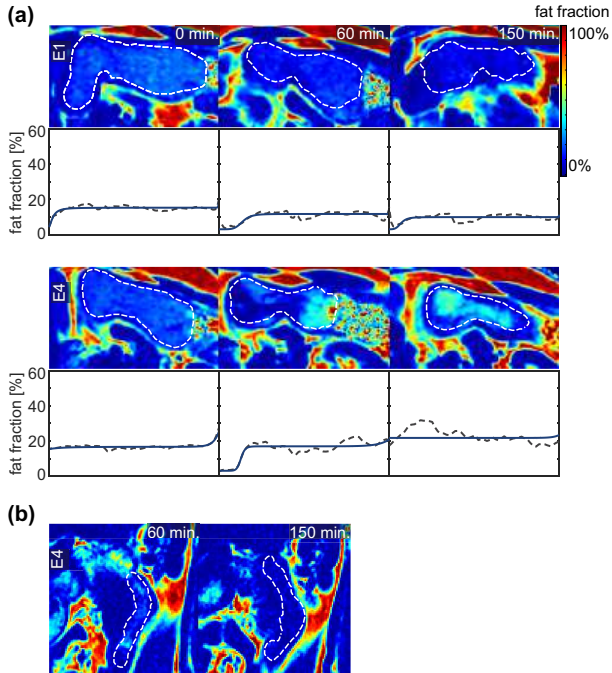
Figure 5 *Gastric and duodenal contents of one subject at different time points. (a) Images showing the cropped and magnified color-coded gastric fat fraction maps of E1 (upper panel) and E4 (middle panel). The corresponding emulsion profile plots show the respective measured (dashed line) and fitted (solid line) intragastric fat fraction profiles (lower panel). (b) Images showing the cropped and magnified color-coded duodenal fat fraction maps of E4 (upper panel). E1 exhibited homogeneous fat distributions, and is therefore not shown. The dashed white curves outline the intraluminal content. It is to be noted that the whole stomach volume rather than a single slice was used for the calculation of the emulsion profiles. Therefore, they cannot be directly compared with the corresponding fat fraction maps.*

The different structuring of intraluminal content described above resulted in different emptying patterns of E1 and E4. Individual gastric emptying curves of TCV and FV grouped per fat emulsion are presented in Figure 6. Initial TCV - that is, the content volume directly after meal intake – showed large differences between subjects. This was attributed to the effect of TCV-1 with a difference of 0.9 (95% CI 0.7, 1.2) mL, rather than
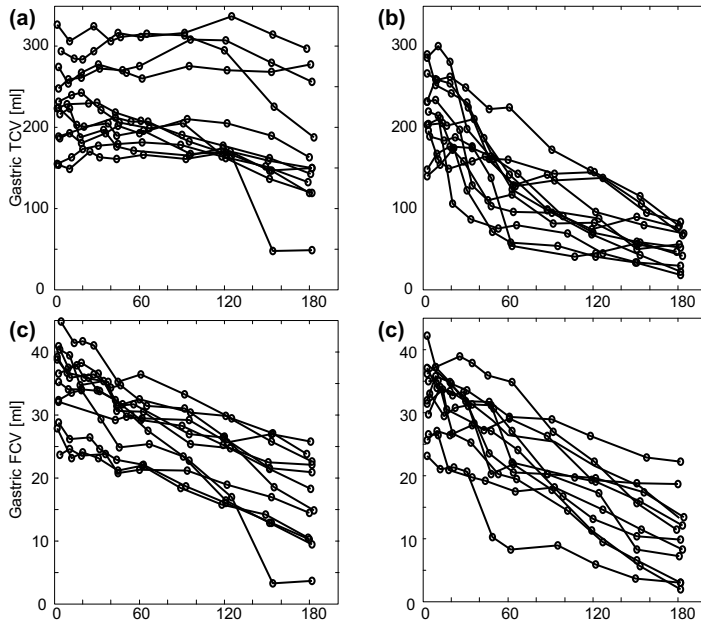
Figure 6 *Change of gastric TCV and FV during emptying. Individual changes in gastric TCV (upper row) and FV (lower row) over time are grouped by E1 (left column) and E4 (right column). Despite the large inter-individual differences and patterns in gastric TCV, resulting gastric FV curves showed a somewhat steady fat emptying for both emulsions.*

the effect of the emulsion type with a difference of –2.2 (95% CI –13.6, 9.1) mL. Therefore, 1 mL of TCV-1 caused an increase in initial TCV by 0.9 mL, which indicates that most residual gastric content still remained in the stomach after intake. TCV of the acid-stable E1 remained high until the end of the scanning period, supporting the observations for the intragastric fat distribution of continuous and intensive dilution with gastric secretion. In several cases, an increase in TCV was observed where the amount of released secretion exceeded that of gastric content emptying. In contrast, TCV of the acid-unstable E4 revealed a distinct non-linear content emptying pattern with rapid decreases during the scanning period. Consequently, TCV emptying for E1 (17 (95% CI 12, 22) mL/h) was slower by 40 (95% CI 33, 48) mL/h compared with E4.

Although gastric content emptying curves exhibited large variations among subjects, which were reflected in the large CI values of TCV, FV curves of both emulsions decreased steadily and yielded smaller CI values. Fat emptying of E1 was 8.6 (95% CI 9.5, 7.7) mL/h, which was slower by 2.5 (95% CI 1.7, 3.3) mL/h compared with E4.

Duodenum

Duodenal fat fractions were lower compared with gastric fat fractions. Similar to the gastric content distributions, duodenal contents for E1 appeared more homogeneous. For E4, the duodenum was irregularly flushed with portions of high fat content from the stomach, as depicted in Figure 5(b).

Figure 7 demonstrates the duodenal curves for the measures of TCV and FV, which exhibited less structure than their gastric counterparts. Time did not significantly predict any of the three measures (TCV: 0.01 (95% CI −0.01, 0.04) mL/h; FV: 0.001 (95% CI −0.001, 0.003) mL/h; fat fraction: 0.0 (95% CI −0.008, 0.008) %), and was therefore removed as a fixed effect in subsequent models. After initial passage of the emulsion through the duodenum, duodenal fat fraction ranged between 5 and 10% for E1. Duodenal TCV for E1 was 22 (95% CI 17, 27) mL, which was larger by 6.3 (95% CI 3.0, 9.3) mL compared with E4. For duodenal FV, E1 was 1.7 (95% CI 1.4, 2.1) mL and also exhibited larger volumes compared with E4 with a difference of 0.5 (95% CI 0.2, 0.8) mL.

5.4   Discussion

This study has demonstrated that with IDEAL it was possible (1) to simultaneously visualize the intragastric and duodenal fat distribution and (2) to quantify the differences in emptying, phase separation and creaming of an acid-stable and acid-unstable emulsion.

The IDEAL method was validated both in vitro and in vivo. The in vitro MR measurements showed an excellent linear dependency and agree-
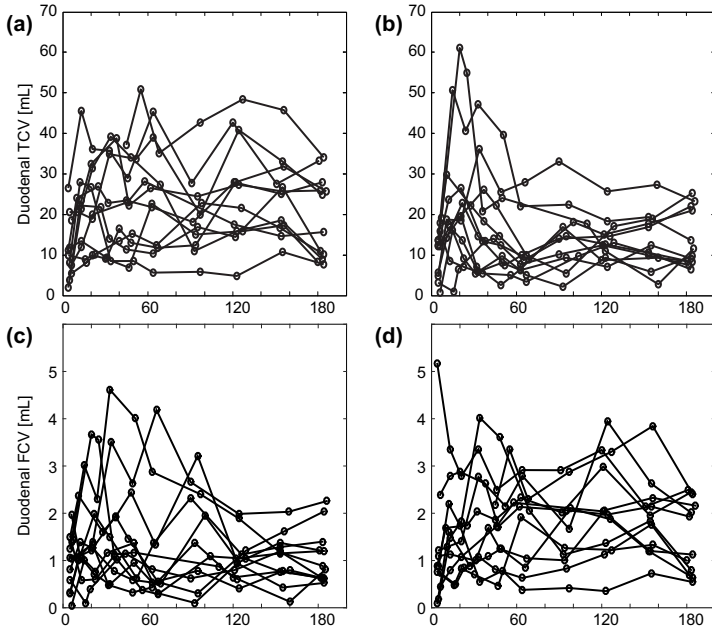
Figure 7 *Change of duodenal TCV and FV during emptying. Individual changes in duodenal TCV (upper row) and FV (lower row) over time are grouped by E1 (left column) and E4 (right column).*

ment between nominal and IDEAL fat fractions. The in vivo validation measurements using the gastric aspirates, however, resulted in lower Lin's concordance, exhibiting larger and more varying differences. These differences were caused by the following systematic measurement biases. First, the weight of the emulsifiers was included in the final weight after drying. Experiments confirmed that this caused the slope of the regression line between laboratory and nominal fat fractions to decrease by up to 10%. Second, experiments further confirmed that gastric juice contained up to 2% of particles other than water, which also remained as residual weight after drying. At 0% fat fraction, this overestimated the measured value, therefore causing a positive intercept of the regression line. Finally, the large spread of residuals was due to the measurement procedure.

Although only those samples with a clear identifiable catheter tip position were included in the analysis, little deviations from the true location of the sample within the stomach could lead to large measurement errors, especially in inhomogeneous regions or regions close to the gastric wall. Despite all these limitations, the detected in vivo correlation was higher than that previously reported for an inversion-recovery-based MRI quantification method [136].

The different intragastric stability of the fat emulsions affected the distribution of the intraluminal content, which could be visualised with both fat-selective images and the quantitative fat fraction maps. The two image types revealed similar structuring of fat emulsion and were in general in good agreement with each other. However, the fat-selective images could not reveal all the features of inhomogeneity evident in the fat fraction maps. In contrast to fat-selective images, fat fraction maps allowed an assessment of the degree of phase separation and creaming and the resulting emptying rate of fat content. The stable fat emulsion always showed a homogeneous gastric fat distribution where fat was increasingly diluted with gastric secretion. The unstable fat emulsion showed highly variable gastric fat distributions with associated bi-phasic layering.

The differences in structuring of intragastric content caused by the different intragastric stability of the fat emulsions were also reflected in the emptying patterns. The stable fat emulsion exhibited very slow gastric content emptying among all subjects, whereas the unstable emulsion showed inter-individual bi-phasic emptying patterns with faster emptying of the separating phase of lower fat content. These observations correspond to findings reported from a previous study [19] using the same fat emulsions. Large inter-individual differences were observed for the initial content volumes. However, these were attributed to the residual content volumes in the fasted stomach rather than to the emulsion type.

Owing to the steady emptying pattern of the fat in both emulsions, the emptying was approximated by a linear model. The fat-emptying rate of the unstable emulsion was faster than the stable emulsion by approximately

41%. This may be due to a larger fat droplet size of the re-emulsified high-fat content phase compared with the artificially small original droplet sizes of the emulsions. Previous data have confirmed that a reduction in droplet size of fat emulsions delays gastric emptying due to more effective lipase activity and increased intestinal sensing and feedback [121].

The model derived from the observed bi-phasic layering of intragastric content yielded a good fit to the emulsion profiles. Although the degree of phase separation was not different between the emulsions, the acid-unstable E4 exhibited a strong degree of creaming. Maximum fat fraction values were twice as large and had a four times larger gradient. Moreover, large variations in emulsion profiles were observed in E4, indicating inter-individual differences in the composition and acidity of gastric secretion. The fluctuations in the emulsion profiles visible in many profiles may be indicators of flocculation of fat droplets, which affect gastric emptying and satiation as previously shown [19]. A thorough analysis on this topic was, however, beyond the scope of this study.

Duodenal emptying curves exhibited less structure than their gastric counterparts; a temporal effect of the curves could not be detected. Although the dynamics of gastric emptying are mainly influenced by content emptying into the duodenum on the one hand and release of gastric secretion on the other hand, duodenal emptying is affected by the incoming content from the stomach, emptying into the small intestine and release of bile. This additional complexity seems to be reflected in the duodenal volume curves that exhibited higher fluctuations than their associated gastric curves. The peaks in duodenal FV may be partly attributed to changes in the subject's body position that occurred in between the scans. A sudden shift of high fat content towards the distal part of the stomach could have caused the duodenum to be flushed with high fat content. A thorough analysis on how body position affects duodenal fat volume was beyond the scope of this study.

Duodenal volumes of total content and fat were both larger for the stable emulsion – that is, by a factor of 34 and 30% respectively – whereas

mean fat fractions remained at similar levels. Although the larger duodenal TCV for E1 indicates increased gallbladder secretion due to increased fat sensing, the larger FV may be explained by a delayed fat transport due to a reduced number of duodenal pressure waves [121].

Two fat emulsions of highly artificial composition were used in order to validate the quantitative MRI methodology. However, the application of IDEAL is not limited to these emulsion types. The application to other fat emulsions is straightforward by substituting the fat model acquired for the rapeseed oil with the appropriate fat model, offering the possibility to choose from a broad range of vegetable or dairy oils. Problems could, however, arise for solid meals or meals generating solid particles within the GI tract. Solid materials cause signal voids in the MR images, resulting in undetectable intraluminal contents.

A major constraint of this method is the rather long maximum breath-hold time used in the study protocol of 34 s, which currently limits the application to healthy individuals. In the future, under-sampling strategies to accelerate data acquisition will reduce scan duration per breath-hold, enabling studies in patients as well [76]. Instead of reducing the breath-hold time, accelerated data acquisition could also be utilized to cover larger fields of view – for example, subjects with larger waist circumferences – and for simultaneous acquisition of gastric and intestinal data. Images covering the entire intestinal tract are useful to provide additional insights into food transit and fat digestion in the lower GI tract. The feasibility of fat quantification in these parts still needs to be investigated because of two factors: first, lower fat contents due to continuous dilution by gastric and duodenal juice, causing the fat fractions to fall below the limit of detection or accuracy, and, second, the disintegration of fat due to digestive enzymes, causing the fat model to be no longer valid. A spectroscopic approach [127] could be potentially applied for analyzing the fat model and its validation in the lower GI tract.

In conclusion, MRI was validated and applied for quantifying the in vivo processing of fat emulsions in the upper GI tract using the water–fat

separation method IDEAL. This not only revealed information about the complexity of food structuring during digestion, but also gave insight into the fate of the fat component with regard to emptying and its characteristics under forces such as trituration and peristaltic activity. These methods have great potential to improve the in vitro–in vivo correlation of current digestive models and to be applied in the process of developing effective functional foods that control energy intake and homeostasis. Both aspects are of key importance in the field of nutrition-related healthcare and eating disorder treatment.

5.5   Appendix

A   Figures
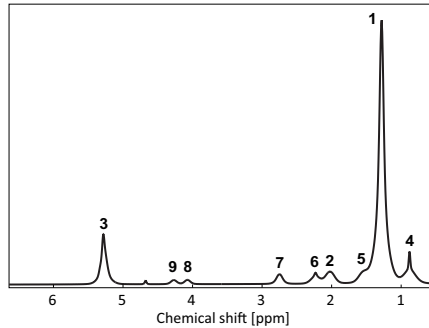
Figure A.1 *MR spectrum of rapeseed oil. The fat peaks are indicated by bold numbers sorted in descending order of amplitude. The chemical shift and relative area of all nine fat peak were included into the fat model.*

Figure A.2 *Aspirated gastric samples. Gastric samples of E1 (left) and E4 (right) of one subject, sorted from left to right in ascending order of aspiration time. Samples of E1 had a homogenous milky appearance whereas in samples of E4 the fat and aqueous phase were largely separated.*
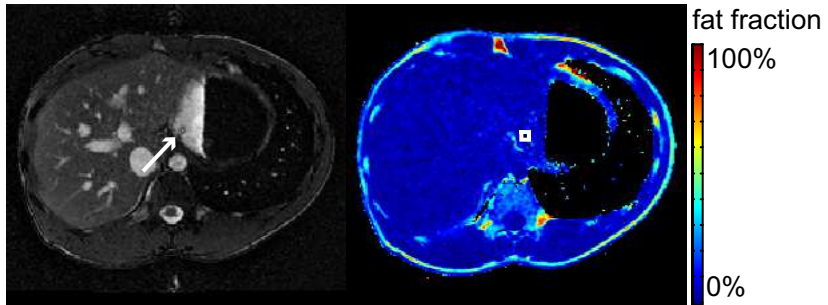
Figure A.3 *Detection of the tip of the nasogastric tube in the image data. The detected tip of the nasogastric tube is indicated by the white arrow in the high resolution volume image data (left). The corresponding ROI used for fat fraction calculations in the fat fraction map (right) is indicated by the white rectangle.*

B   Emulsion preparation

The fat emulsions E1 and E4 were prepared as follows to obtain the desired properties: E1 was prepared by mixing 240 g rapeseed oil with 360 g of a 2.7-weight percent polysorbate 80 (Palsgaard) solution by using a rotor stator homogenizer (MICCRA D 15, 25-mm rotor stator; MICCRA) at 10,500 × g and 50°C for 5 min. A fine emulsion was created by passing this mixture through a microfluidizer 3 times at 200 bar (model M110Y equipped with an H30Z 200-mm and F20Y 75-mm chamber, Microfluidics). This fine emulsion was diluted 1 to 1 with water to achieve the final composition.

E4 was prepared by mixing 240 g rapeseed oil and 3 g distilled mono-glyceride (Dimodan HP-M; DuPont Danisco) with 957 g 1.25-weight percent sodium caseinate (DMV International) solution by using the rotor stator homogenizer at 10,500 × g and 70°C for 5 min. A fine emulsion was created by passing these mixtures through the microfluidizer twice at 300 bar.

C   MR sequence parameters

1. Volume scans
   Steady-state free-precession sequence; echo time 1.31 s, repetition

time 2.6 ms, flip angle 60°, voxel size 2.3x2.0 mm^2

   (a) Gastric
       20 transverse slices, slice thickness 8 mm, field of view 350x258 mm^2, scan duration 7 s

   (b) Duodenal
       7 sagittal slices; slice thickness 6 mm, field of view 350x258 mm^2, scan duration 5 s

2. IDEAL scans
   6-point multi-echo gradient echo sequence with flyback gradients; first echo time 1.25 ms, echo time spacing 1.54 ms; repetition time 10 ms, flip angle 10°, voxel size 2.3x2.0 mm^2

   (a) Gastric
       20 transverse slices, slice thickness 8 mm, field of view 350x258 mm^2, scan duration 34 s

   (b) Duodenal
       7 sagittal slices; slice thickness 6 mm, field of view 350x258 mm^2, 2 averages, scan duration 21 s

3. Fat-selective scan (gastric)
   Single-shot turbo spin-echo sequence with a spectral inversion recovery pre-pulse for water suppression; echo time 80 ms, repetition time 732 ms, flip angle 90°, voxel size 2.3x2.0 mm^2, 20 transverse slices, slice thickness 8 mm, field of view 350x258 mm^2, scan duration 15 s

4. High-resolution volume scan (gastric)
   Steady-state free-precession sequence; echo time 1.7 s; repetition time 3.4 ms, flip angle 60°, voxel size 1.5x1.5 mm^2, 30 transverse slices, slice thickness 6 mm, field of view 350x259 mm^2, scan duration 19 s

D   Model equation

Fat layering was modeled with a robust 5-parameter fit according to

$$\mathrm{ff}(x) = \mathrm{ff}_0 + \mathrm{ff}_1 \left(\frac{x^n}{x^n + x_0^n} + e^{(x - x_F)S} \right).$$

6 Intragastric fat and secretion

6.1 Introduction

Lipids are omnipresent in today's processed foods, because they enhance taste, texture and mouthfeel. However, the excessive intake of fat in Western societies is considered to be a key determinant in the development of obesity and other diet-related chronic diseases [139]. Controlling gastrointestinal (GI) digestion and release of fat in the form of oil-in-water emulsions in order to benefit human health has become a key topic for nutrition sciences, the food industry and the pharmaceutical industry [140, 141].

Much of the nutritional research conducted on oil-in-water emulsion digestion involves the use of in vitro digestion models that simulate the effect of different gastric and intestinal conditions on the metabolism of emulsified fat [33, 142]. Moreover, only a small number of studies have begun to examine gastric fat digestion in detail [38, 143]. However, findings have demonstrated that gastric secretion has a large impact on ingested emulsions. Biophysical factors, such as gastric acidity, gastric mucosa, gastric motor activity (including mixing and shear stress), and dissolved biopolymers can destabilize the emulsion structure. These biophysical factors contribute to creaming, flocculation and separation of the water and fat phase of the emulsion [122]. It has been well documented that gastric secretion is stimulated in the gastric and intestinal environment by the presence and sensing of nutrients [144]. Therefore, the fat-induced stimulation of gastric secretion and the secretion-induced destabilization of the emulsion are key factors for intestinal bioavailability and the sensing

of ingested emulsified fat.

Magnetic resonance imaging (MRI) provides a comprehensive and non-invasive technique for the analysis of food emulsion processing in vivo. Therefore, it has the potential to bridge the gap between current in vitro models and in vivo studies [16, 19]. Standard MRI techniques have been applied frequently to assess gastric content emptying for a wide range of foods [145–149]. Two quantitative MRI techniques have been developed recently that enable the visualization of fat and secretion within the total gastric content. Hence, by "mapping" fat fractions or secretion concentrations inside the stomach, the effects of different emulsions or pathologies on the volume and distribution of fat [71, 110] or secretion [25, 65, 66, 131] can be investigated. Combining MRI fat fraction and secretion mapping technologies is technically challenging: the latter method is limited to aqueous objects with mono-exponential T_1 relaxation times. However, oil-in-water emulsions have a bi-exponential relaxation behavior, which demands an additional correction.

Therefore, this required the development and evaluation of a combined MRI fat fraction and secretion mapping scheme. Thus, the overarching aim of this study was to apply a novel imaging scheme in order to noninvasively determine 1) how emulsion stability modulates intragastric volumes, layering and mixing of emulsified fat and secretion and 2) how the corresponding parameters are interrelated.

6.2   Methods

6.2.1   Emulsion preparation

Two oil-in-water emulsions with differing acid stabilities were used in this study (20% fat fraction and 0.3 mm droplet sizes): an acid stable emulsion (E1) and an unstable emulsion (E4), which have been previously utilized in other studies [19, 38, 110, 150]. The emulsions were labeled with 1 mM of the MRI contrast agent Gd-DOTA (DOTAREM®, Guerbet, France) in order to reduce the initial T_1 values of the emulsions.

6.2.2   Study design

Study population

This study was approved by the local ethics committee and was part of a clinical study registered at ClinicalTrials.gov with identifier NCT02602158. This study was a randomized, single-blinded, parallel study design. Written informed consent was obtained from healthy subjects before the start of the study. At a screening visit, subject eligibility criteria were assessed. Those subjects with current health problems or a history of GI disease or abdominal surgery (excluding appendectomy or hernia repair) were excluded. Subjects also must have provided a negative pregnancy test if applicable, had a body mass index (BMI) between 18 and 25 kg/m^2, been a nonsmoker or a nonregular smoker, been aged between 18 and 50 years, and had no contraindication to MRI. Subjects received either E1 or E4 according to a computer-generated randomization sequence, which was defined by permutated blocks. The emulsions had the same visual appearance, which ensured blinding of the subjects. All subjects underwent MRI scans on each of the two different study days. The first and second study days were identical and were used to assess the variability between two measurements within one subject.

The study was powered on the results from a previous study [66] that provided the variability in secretion volume (SV) for a liquid meal. On the basis that 20 mL would be a feasible estimate of the SD for emulsions, we estimated that a total of 11 subjects would be needed to detect a difference of 22 mL secretion, with a defined power of 0.9.

Measurements

On each study day, subjects arrived in the morning at the magnetic resonance (MR) center of the University Hospital Zurich after 8 h of fasting. All images were acquired in the right decubitus position with the use of a 1.5T MRI scanner (Achieva, Philips Healthcare) and an abdominal phased array coil (4-channel SENSE body coil, Philips Healthcare). During scan

pauses, subjects were allowed to assume a sitting position to ensure that intragastric gas accumulated in the fundus and was excluded from the antrum [134]. 200 mL (380 kcal) of each emulsion was ingested within 1-2 min in the seated position. Postprandial MR images were acquired in a total of eight scan blocks; these were performed at time points t=0 (end of ingestion), 20, 40, 60, 90, 120, 150 and 180 min. In each scan block, three image types were acquired: 1) a volume scan for obtaining intragastric total content volumes, 2) a water-fat scan for fat fraction mapping and 3) a T_1 scan for T_1 mapping and subsequent secretion concentration mapping (Appendix B).

6.2.3   Image reconstruction

Fat fraction maps

Water-fat scan data were reconstructed with the use of the iterative decomposition with echo asymmetry and least squares estimation (IDEAL) approach [133] as implemented in [151] and a T_1 correction [152]. Quantitative maps of fat fraction [%] were calculated by taking the ratio of the reconstructed water and fat images.

T_1 and secretion concentration maps

T_1 scan data were reconstructed with the use of a B_1 correction [62,153] and fat correction (Appendix C and Figure A.1). An in vitro experiment was performed in order to determine the relation between T_1 and the degree of emulsion dilution caused by gastric secretion [25]. The resulting calibration curves as presented in Figure 1 were subsequently used in order to quantify secretion concentration [%], i.e. the volume ratio between secretion and the total content. A color coding was applied for the fat fraction and secretion concentration maps, where blue and red indicate 0% and 100% fat fraction or secretion concentration, respectively.
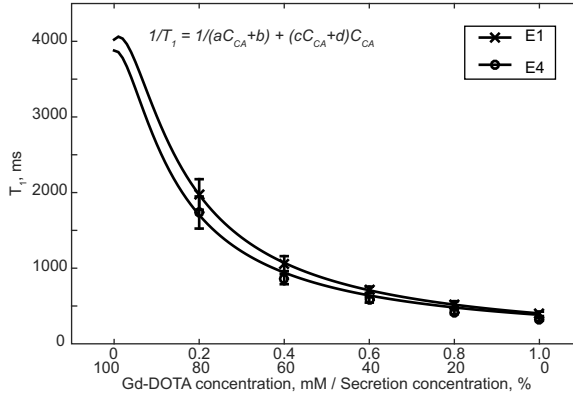
Figure 1 *In vitro calibration of T_1-secretion relationship for E1 and E4. Measured T_1 values are mean ± SD with their corresponding nonlinear least squares fits. The T_1-secretion relationship follows the depicted equation with $a = 4.07 \cdot 10^4$ ms·mM, $b = 4023$ ms, $c = 4.25 \cdot 10^{-4}$ ms^{-1}·mM^{-2}, $d = 2.04 \cdot 10^{-3}$ ms^{-1}·mM^{-1}, $R^2 > 0.99$ for E1 and $a = 3.89 \cdot 10^4$ ms·mM, $b = 3878$ ms, $c = 0.97 \cdot 10^{-4}$ ms^{-1}·mM^{-2}, $d = 2.49 \cdot 10^{-3}$ ms^{-1}·mM^{-1}, $R^2 > 0.99$ for E4.*

6.2.4   Visualization of distribution

A custom software tool written in MATLAB 2012b (The MathWorks, Natick, MA, USA) was used for image segmentation and related volume calculation. Intragastric total content volumes, which are defined as total stomach volumes without intraluminal air, were derived by semi-automatically segmenting the content of each volume scan [137] and applying these contours to the fat fraction maps and secretion concentration maps, respectively. Fat volume (FV) was calculated at each time point and plotted over time to generate volume emptying curves [110]. SV was calculated analogously from the secretion concentration maps.

Intragastric fat distribution was characterized by the layering of the creamed fat of the emulsion. Therefore, fat layer profiles were computed along the extent x of the stomach in the direction of gravity [110], which depicts the change in fat fractions from the distal (small x-values) toward the proximal stomach (large x-values).

The mixing of fat and secretion content was quantified by the intragastric dominance (D), which was defined as the difference between the fat fraction and secretion concentration maps, i.e. D = fat fraction [%] – secretion concentration [%]. Large positive or negative values for D therefore corresponded to a dominance in fat or secretion, respectively. Profiles of D were reconstructed along x and combined into color-coded "mixing graphs" similar to the layer graphs described in [66] in order to visualize both the change of D along the stomach extent and time.

6.2.5   Parameter modeling

Intragastric fat distribution was represented by two layer parameters extracted from the fat layer profiles [110]: the degree of creaming or maximum fat fraction in the stomach (ff_{max}) and the normalized spatial extent of the fat layer (E).

Two mixing parameters reflecting the degree of mixing in the stomach during the emptying process were defined. These parameters included the overall D and content heterogeneity, which were calculated by averaging the mean and the SD of D within intragastric content over the scanning period, respectively.

In order to determine volume emptying, the linear exponential (LinExp) model [147] was applied to mathematically describe both FV and SV curves as follows,

$$V(t) = V_0\Big(1 + \frac{kt}{T}\Big)e^{-t/T}\,, \tag{6.1}$$

with the three fitted volume parameters for the initial postprandial volume V_0, the initial volume increase k and the subsequent volume emptying time T. Indexes f and s were used to indicate the parameters for fat and secretion, respectively. In the case of FV, k_f describes an emptying delay rather than an initial increase, because no further fat enters the stomach after ingestion.

6.2.6   Statistical analysis

Statistical analyses were carried out with program R, version 3.1.3 [138]. Layer and mixing parameters were tested by linear modeling with emulsion as a fixed effect to evaluate the influence of emulsion stability. In order to further test for the emulsion-dependent differences of mixing in ff_{max}, linear models with the SD of D as fixed effect were computed separately for each emulsion. The function lm was used for the linear models. The resulting estimates were presented as means (95% confidence intervals (CIs)).

Volume parameters were extracted from the fitted curves in a hierarchical Bayesian Markov chain Monte Carlo sampling strategy with R package rstan (version 2.8.2) [19]. A varying intercepts mixed-effects model [154] was used with emulsion as a fixed effect and study day and subject as random effects. Volume parameter estimates were presented as means (95% highest posterior density CIs. To determine the dependency between volumes and fat layering, pairwise correlations were performed between the layer and volume parameters. Spearman's rank coefficient r was used because of the non-normal distributions.

The inclusion of the random effects for the volume parameters enabled the extraction of the variability of each effect, which was determined by the coefficient of variation (%CV) based on the respective sample mean [155]. This yielded estimates for the intra-subject %CV and inter-subject %CV (Appendix D).

6.3   Results

In total, 22 subjects were included in the study. MRI scans were performed on all 22 subjects (13 men, 9 women; mean ± SD age: 22.5 ± 2.5 years; mean ± SD BMI: 22.7 ± 1.8 kg/m^2). Data from one scan block was missing because of technical errors. Data from one subject, who arrived on both study days with a substantial amount of intragastric content, was excluded from the analysis. Intragastric volumes were successfully deter-

mined in all remaining subjects. Statistical analyses were performed on 355 observations for fitting volume emptying curves. Layer parameters were analyzed for each emptying curve, yielding 42 observations.
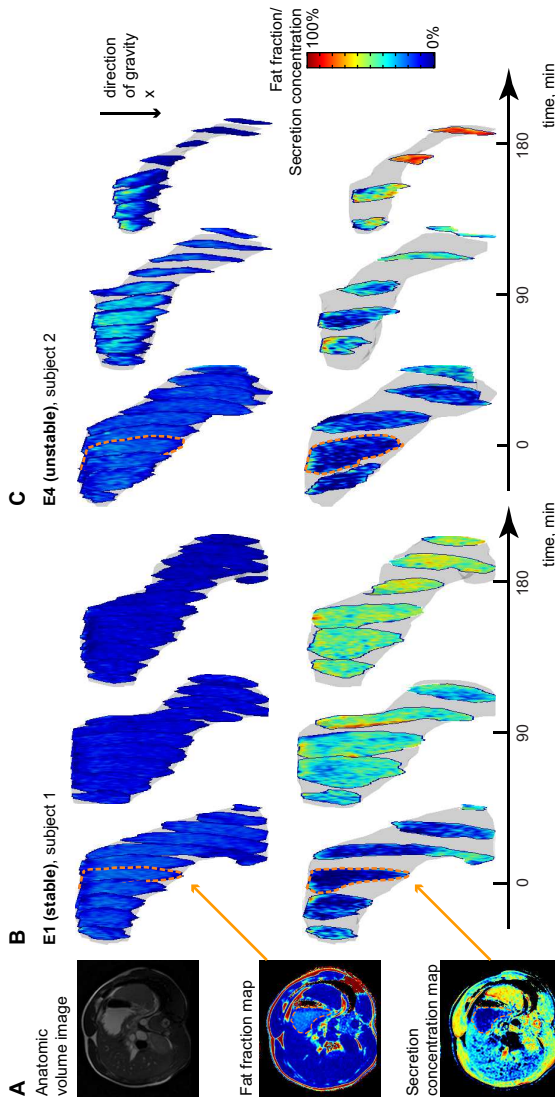
Figure 2 *Temporal development of intragastric content. (a) Exemplary transverse slices with delineated stomach (dashed orange line) of an anatomic volume image, fat fraction map and secretion concentration map at time point 0 min of one subject after intake of E1. (b) Entire gastric content of fat fraction and secretion concentration at time points 0, 90 and 180 min. of the same subject and (c) of a second subject after intake of E4.*

6.3.1   Influence of emulsion stability

Intragastric distribution

The different intragastric stabilities of the emulsions resulted in different distributions of intragastric content, where fat and secretion revealed distinct structuring patterns. Typical intragastric distributions of the acid stable emulsion E1 and the acid unstable emulsion E4 are displayed in Figure 2. The ingested E1 largely maintained its stability throughout the 180-min scanning period and showed a homogenous mixing of secretion and fat. Phase separation of E1 was not observed in the fat layer profiles or in the mixing graphs (Figure 3). The overall steady decrease in fat fraction values and continuous dilution of intragastric content by gastric secretion was illustrated by a general change of D, i.e. difference between fat fraction and secretion concentration, toward more negative values over time. This demonstrated the homogenous mixing processes of E1, where the intragastric content was continuously and increasingly mixed with gastric secretion.

Conversely, E4 underwent clear structural changes under the acidic gastric conditions, resulting in less homogeneous distributions. Shortly after ingestion, E4 exhibited fat creaming, leading to a bi-phasic fat distribution: a layer of higher fat fraction with typically positive values for D developed on top of the remaining, more aqueous content in the antrum with negative values. Although the dynamics of this bi-phasic structuring varied considerably between subjects, a general pattern still could be observed. Initially the subjacent aqueous layer mostly consisted of water from the emulsion. However, as gastric content emptied from the antrum into the duodenum, the extent of this aqueous layer gradually decreased. Concurrently, gastric secretion was excreted from the stomach wall and into the stomach. This mixed with the intragastric contents to varying degrees, depending on the subject. Therefore, the aqueous layer gradually changed its composition because of the accumulation of secretion.
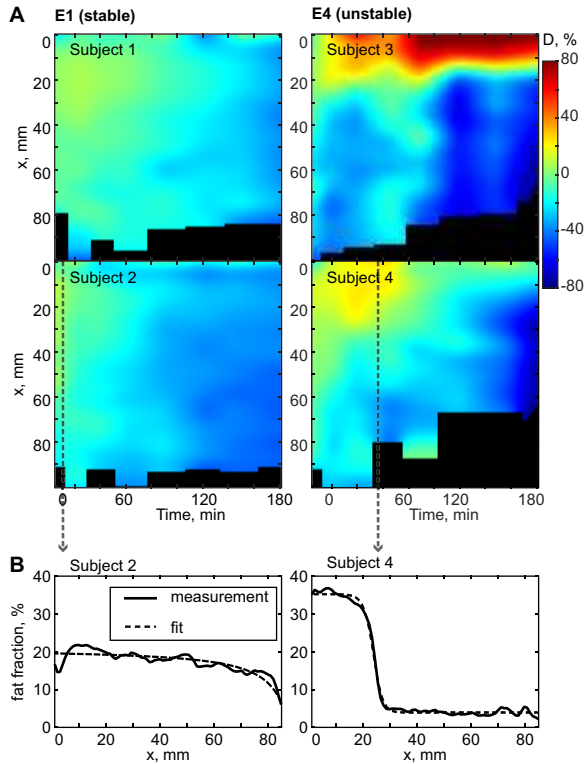
Figure 3 *Intragastric distribution and layering for E1 and E4. (a) Exemplary intragastric mixing graphs of two subjects per emulsion, which are arranged such that x is aligned along the direction of gravity. A dominance of fat can thus be observed on top of the stomach content, i.e. for small x values. The dashed arrow indicates the time point of maximum layering. (b) Exemplary fat layer plots of one subject per emulsion at the time point of maximum layering. The corresponding fits were used for extracting the layer parameters.*

Fat layering

The layer formation was reflected in the different layer parameters of E1 and E4, which are summarized in Table 6.1. The degree of creaming and fat layer extent were both larger for E4 Δff_{max}=37.2 (26.7, 47.6)%, ΔE=0.61 (0.49 , 0.73)], whereas E1 showed only limited creaming of ff_{max}=23.1 (15.5, 30.6)%.

	Parameter	Intercept	Emulsion difference
Layering	ff$_{max}$ [%]	23.1 (15.5, 30.6)	37.1 (26.7, 47.6)
	E	0.12 (0.04, 0.21)	0.61 (0.49, 0.73)
Mixing	mean of D [%]	-19.5 (-24.1, -14.8)	2.7 (-3.7, 9.1)
	SD of D [%]	15.4 (11.9, 18.9)	17.1 (12.3, 21.9)

Table 6.1 *Comparison of the layer and mixing parameter estimates for E1 and E4. Values are means (95% CI), n=42.*

Volume emptying

Similar to the intragastric distributions, the content emptying patterns differed for E1 and E4. Individual volume emptying curves of FV and SV grouped per emulsion are presented in Figure 4. Whereas FV depicts the emptying process of the ingested fat, SV depicts the positive net balance of secretion production and emptying. The differences in the volume parameters of the LinExp model are summarized in Table 6.2. Individual volume emptying curves and corresponding fits are presented in Figure A.2. There was an emulsion effect on the emptying time of fat (T_f) and initial emptying delay of fat (k_f) [ΔT_f=-26.5 (-50.5, -3.6) min, Δk_f=0.4 (0.1, 0.6)] indicating that for E4, the initial delay of fat emptying was longer but, subsequently, FV was emptied faster. An emulsion effect was also detected for the initial increase of secretion (k_s), indicating less accumulation of secretion for E4 [Δk_s=-2.3 (-3.9, -0.7)].

Mixing

Overall content dominance (mean of D) was -19.5 (-24.1, -14.8)% for the stable emulsion E1 and did not differ for E4. The negative D values demonstrate that for both emulsions, secretion eventually dominated in the mixing process. The degree of mixing of the two emulsions were classified into two distinct content heterogeneity (SD of D) ranges. Low heterogeneity levels were detected for E1 ranging from 12% to 22% and characteristically higher levels were detected for E4 ranging from 15% to 54%. On average,

Parameter	Intercept	Emulsion difference	Study day difference
k_f	0.8 (0.7, 1.0)	0.4 (0.1, 1.6)	0.1 (-0.01, 0.3)
T_f [min]	90 (88, 92)	-26 (-51, -4)	-2 (-10, 11)
V_{0f} [mL]	36.3 (34.8, 37.3)	-1.4 (-3.3, 1.3)	0.3 (-0.9, 2.4)
k_s	3.0 (1.5, 4.4)	-2.3 (-3.9, -0.7)	0.4 (-0.6, 1.2)
T_s [min]	141 (100, 184)	-38 (-88, 18)	-13 (-46, 15)
V_{0s} [mL]	36.1 (34.5, 38.2)	2.5 (-13.2, 20.0)	-5.2 (-14.1, 6.8)

Table 6.2 *Comparison of volume parameter estimates for E1 and E4. Values are means (95% CI), n=42.*

the content heterogeneity of E1 was SD of D = 15.4 (11.9, 18.9)%; this was considerably larger for E4 [ΔSD of D=17.1 (12.3, 21.9)%].

6.3.2   Interrelation of parameters

The relation between the degree of creaming ff_{max} and content hetero-geneity SD of D differed distinctly between the emulsions. The analysis showed that for E1, the degree of creaming was independent of the de-gree of mixing, with an intercept of 16.6 (6.5, 26.8)% and a non-significant slope of 0.42 (-0.23, 1.07). In contrast, E4 showed a stronger creaming with increased mixing, with an intercept of 9.1 (-15.3, 33.5)% and a slope of 1.57 (0.86, 2.29). The intercepts represent the theoretical degree of creaming that would occur for completely homogeneous mixing conditions, i.e. for zero-valued heterogeneity. The two linear models are presented in Figure 5.

Correlations were found between the inverse of k_s and ff_{max} (r=0.62, P<0.001) and between k_f and E (r=0.78, P<0.001). These indicated the presence of smaller SVs during stronger creaming and longer delays in fat emptying for stronger layering.
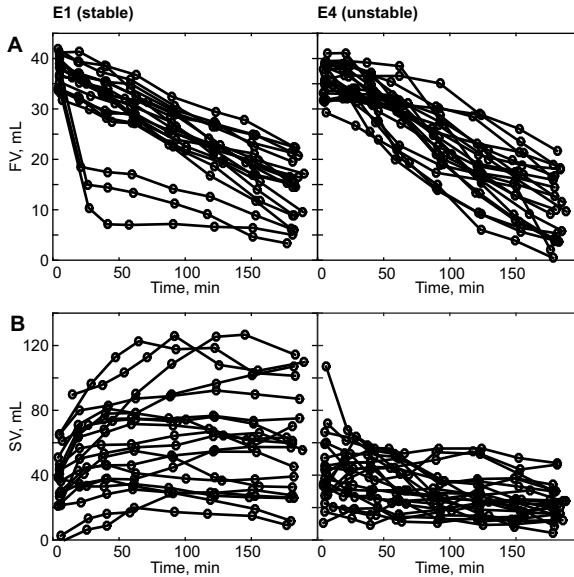
Figure 4 *Individual volume emptying curves in healthy subjects of (a) FV and (b) SV, grouped by E1 and E4.*

6.4   Discussion

In this study, the intragastric distribution of gastric secretion and emulsified fat was noninvasively determined by means of a combined quantitative MRI methodology that enabled the mapping of fat and secretion concentration inside the stomach. The effects of emulsion stability on gastric SV, fat layering and emptying, as well as intragastric mixing, were quantified. Additional insights were derived on the degree of influence that these parameters have on each other during the gastric emptying period.

Previous MRI studies that assessed only the intragastric secretion distribution in liquid test meals demonstrated that secretion can accumulate as a layer on top of the meal [66]. A more recent MRI study assessing fat fractions in oil-in-water emulsions revealed a homogeneous gastric fat distribution in stable emulsions and highly variable, bi-phasic fat distribu-
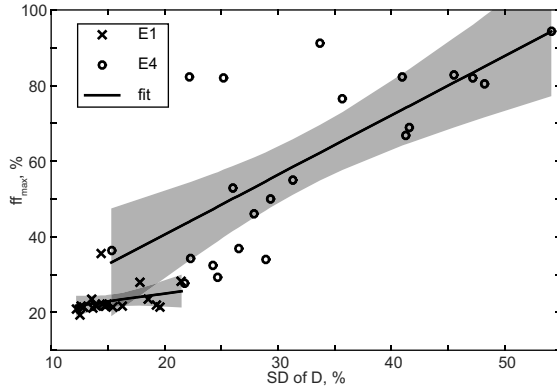
Figure 5 *Correlation plot between the content heterogeneity SD of D and the degree of creaming* ff$_{max}$, *showing the linear model for E1 and E4, with the gray area as 95% CI.*

tion in unstable emulsions [110]. In the current study gastric secretion and intragastric fat fraction were assessed concurrently. It was demonstrated that accumulated gastric secretion distributed differently dependent upon the acid stability of the emulsions. Following ingestion of the acid stable emulsion, secretion homogeneously diluted intragastric fat content. This was observed consistently for all volunteers on both study days. Conversely, the distribution of secretion of the unstable emulsion was highly heterogeneous and varied considerably between subjects and study days. There was no bias between the two study days. The secretion accumulated predominantly in the aqueous layer located in the gastric antrum, whereas fat underwent large amounts of creaming and, as such, moved upwards to form an overlying fat layer. This phenomenon was not surprising, because emulsion water and secretion have a higher density than does fat. These features of continuous fat dilution and bi-phasic fat layering correlate with the findings from the previous MRI study [110].

Emulsion stability also had an effect on the volumes of gastric secretion and intragastric fat. The stable emulsion generated an increased accumulation of secretion and a slower emptying of fat. In contrast, the unstable emulsion generated a lower accumulation of SVs and hence faster

fat emptying. Although there exists limited information on the effect of different emulsion properties on plasma profiles of GI hormones [150], previous studies have shown that stable emulsions are associated with slower gastric content emptying and increased release of the GI hormone cholycystokinin (CCK) [17]. This may be due to the intragastric preservation of small fat droplet sizes and more efficient sensing of fat in the duodenum [121]. This in turn may enhance inhibitory signals, including contraction of the pyloric sphincter. However, increased circulating CCK is associated with an inhibitory effect on gastric secretion. Therefore, our findings suggest that the differences between the accumulation of SVs by the two emulsions may be due to slower secretion emptying than an increase in secretion production. However, only net intragastric secretion accumulation can be assessed currently by imaging and, hence, direct information regarding the differences in production and emptying rate of secretion remain difficult to obtain.

Despite the influence of emulsion stability on gastric SVs, the overall D value stayed negative and was not influenced by emulsion stability. This implies that secretion dominated the intragastric content for both emulsions throughout the gastric emptying process. This finding suggests that the emptying of fat and the accumulation of secretion were somewhat in balance, such that the overall dominance remained at a consistent level.

The overall D did not modulate fat creaming. However, strong creaming was related to small SVs and content heterogeneity. Strong creaming in the unstable emulsion induced the emulsified fat to move upwards and allowed more secretion to accumulate within the distal aqueous layer. Therefore, this may have promoted faster emptying of the SV that accumulated in the antrum and, hence, lowered the overall observed SVs. Thus small accumulated SVs were sufficient to create the acidic environment required for the creaming processes of the emulsified fat.

The intragastric behavior of emulsions was characterized by different intragastric degrees of mixing leading to different content heterogeneities. Stable and unstable emulsion classified into two distinguishable ranges of

heterogeneity. Within these two heterogeneity ranges, the ingested fat was associated with different creaming processes. The fat within the stable emulsion mixed well with secretion and no creaming was evident. The unstable emulsion underwent a particularly lower degree of mixing. In particular, less well-mixed intragastric content demonstrated larger amounts of creaming. Interestingly, the zero-valued intercept of the regression curve for the unstable emulsion suggested that completely homogeneous mixing conditions could only be achieved if maximum fat fractions were zero, i.e. in the absence of emulsified fat. Therefore, the interaction of secretion with the unstable emulsion will in practice always induce creaming, resulting in heterogeneous mixing conditions. In summary, the intragastric fat layering was mainly influenced by the degree of mixing rather than the overall dominance. The stable emulsion impeded the creaming process and generated a higher accumulation of secretion, which in turn facilitated homogeneous mixing of intragastric content in comparison with its unstable counterpart. These properties could contribute to the previously reported enhanced satiation of stable emulsions [19, 71].

A previous MRI study demonstrated that FV emptying was dependent upon emulsion stability. Thus, fat emptying of the unstable emulsion was 40% faster than fat emptying of the stable emulsion [110]. This estimate was computed by a linear emptying model because of the approximately steady decrease in the measured FVs. This study applied the LinExp model, which provided a more differential insight into fat emptying dynamics. The LinExp model confirmed the faster FV emptying of the unstable emulsion and, in addition, detected a longer emptying delay. This emptying delay was correlated to the extent of the fat layer and is thus reflective of the bi-phasic layering pattern. Hence, as the ingested unstable emulsion separated the creamed fat moved upwards toward the proximal stomach and away from the pylorus. Therefore, the larger the layer extent, the less fat was subsequently available within the subjacent aqueous layer and thus the less fat was initially emptied.

The largest source of measurement bias potentially arose from the in-

creased measurement inaccuracies at high T_1 values, which corresponded to a reduced measurement accuracy of high secretion concentrations. The good mixing for the stable emulsion ensured that high secretion concentrations rarely occurred. High secretion concentrations were observed predominantly in the unstable emulsion. This may have led to some overestimation of the observed differences. However, critically high concentrations mostly occurred in largely reduced total content volumes during the late phase of gastric emptying; therefore, the impact of the errors was limited.

These previously well-described emulsions with known differences in intragastric stability enabled the authors to independently assess both fat processing and secretion but also, notably, how these factors interrelate with one another. Future study designs will apply the MRI measurements described to more complex emulsion compositions, along with complementary measurements, e.g. plasma profiles of GI hormones and appetite measures.

The behavior of oil-in-water emulsions in the human stomach can be described in detail by using quantitative MRI methods presented in this paper. Such thorough, in vivo description of how food interacts with digestive processes is a major step toward tailoring new foods with the intention of controlling the intake of different ingredients.

6.5   Appendix

A   Figures
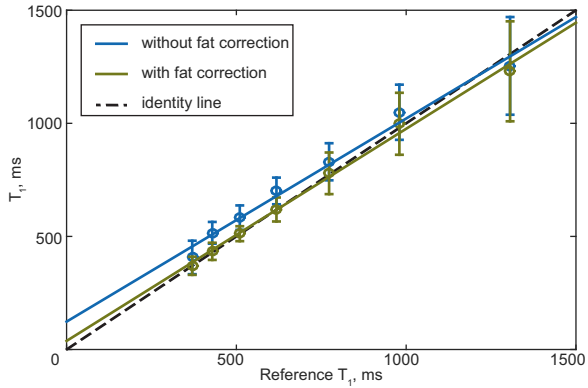
Figure A.1 *In vitro correlation of T_1 measurements without (y = 0.855x + 150.3, R^2 = 0.98) and with fat correction (y = 0.934x + 40.6, R^2 = 0.99). Values are mean ± SD.*
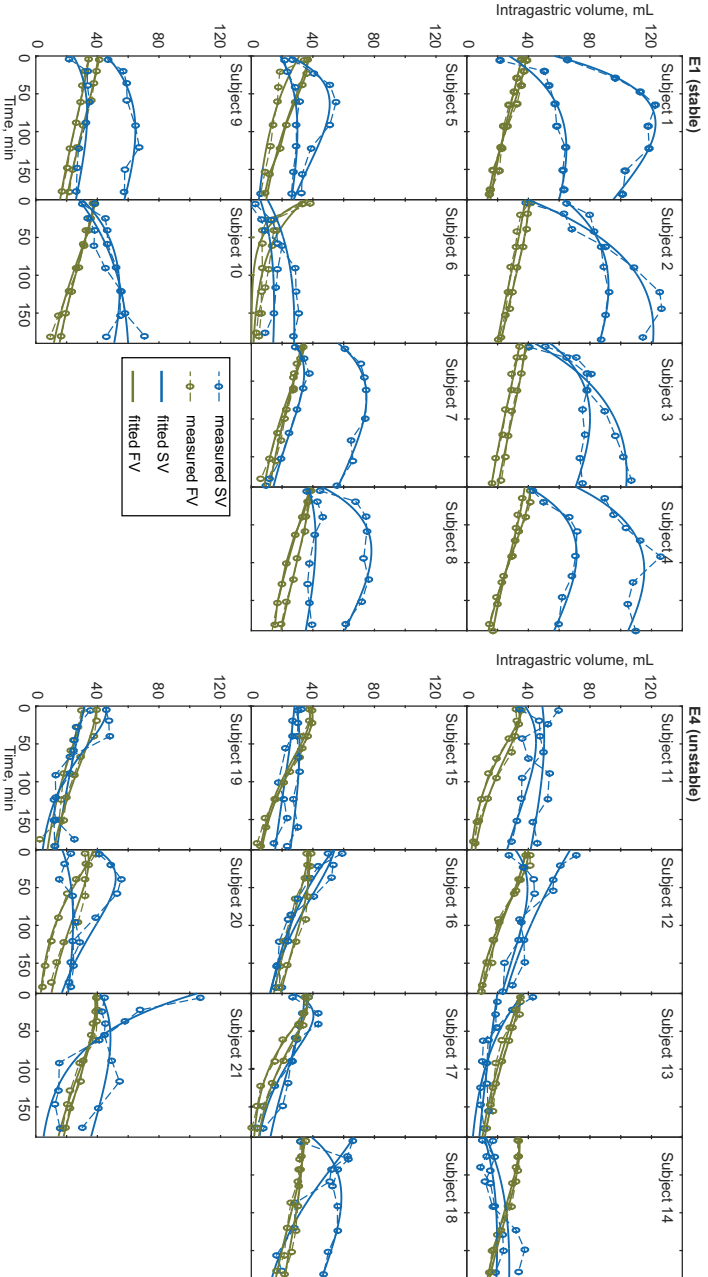
Figure A.2 *Individual volume emptying curves of E1 (left) and E4 (right). Each panel shows the measurements and corresponding fits using the LinExp model of one subject on the two study days of SV and FV, respectively.*

B   MR scan parameters

C   Fat correction

The T_1 scan data was reconstructed using a combined T_1 and B_1 mapping approach [153] with B_1 measurements based on the dubbed dual refocusing echo acquisition mode (DREAM) sequence (29). For an emulsion, the measured MR signal consists of a water component S_w and a fat component S_f according to,

$$S = S_w + S_f \,.$$

In order to estimate S_f, IDEAL scan data was reconstructed with Hierarchical IDEAL [133], which incorporates a spectral fat model of rapeseed oil with the relative amplitude a_p and chemical shift f_p of each peak p. The reconstruction estimated a complex field map $\hat{\psi}$ and separated the total signal into its water and fat density, W and F, respectively, from which quantitative fat fraction maps were obtained. Given the estimate for F and $\hat{\psi}$ from the water-fat separation, S_f can be computed for the T_1 scan data according to

$$S_f = F \, \frac{\sin \beta (1 - E_{1f})}{1 - E_{1f} \cos \beta} \sum_p a_p e^{i2\pi f_p} \, e^{i2\pi \hat{\psi}} \,,$$

where β is the flip angle and $E_{1f} = e^{-TR/200\text{ms}}$ is the predefined T_1 decay of fat. Subtracting S_f from S finally removes the bi-exponential component from the signal. For the resulting S_w, a mono-exponential T_1 fitting procedure was applied. The final T_1 maps were used for obtaining secretion maps. As a positive side effect, the T_1-bias in the fat fraction maps could be corrected by removing the T_1-weighted fraction in [A.2] for fat.

For the in vitro experiment, water was used to simulate gastric secretion as T_1 values of water and gastric secretion are comparable [25]. Each emulsion underwent a serial dilution with water in order to obtain five homogenous solutions. The T_1 of the solutions were then measured with

the imaging protocol described in Appendix B. The dilution of the emulsion altered the Gd-DOTA concentration and thus the T_1 of each solution.

Figure A.1 shows the agreement of in vitro T_1 values with and without fat correction. For secretion concentrations, the influence of the fat correction was most evident at higher fat fractions, i.e. low T_1 values, where the fat component played a larger role in the overall signal. For the fat fraction maps, the influence of the T_1-bias correction was most evident at lower fat fractions. Therefore, both corrections are important for an accurate quantification of fat and secretion at both low and high fat fractions.

D   Variability measurements

Volume parameter	Inter-subject %CV	Intra-subject %CV
k_f	17.1	10.5
T_f	6.7	1.2
V_{0f}	1.1	0.9
k_s	28.8	9.9
T_s	15.7	7.5
V_{0s}	26.1	9.8

The high inter-subject variability observed in the intragastric distributions were reflected in the high variability of volume parameters. Inter-subject variations were larger than intra-subject variations, which were both within the range of intragastric volume variations measured in previous MRI studies [147]. In part, the high inter-subject variability must be attributed to three gastric dumping cases which showed immediate rapid decrease in gastric content and FV. Nevertheless, since these cases did not have a large impact on the results, which further emphasizes the robustness of the study and analysis approach, the measurements were retained in the analysis. The derived coefficients of variation can be used to estimate the required sample sizes for similar future studies.

7 Accelerated fat quantification

7.1 Introduction

Magnetic resonance imaging (MRI) in conjunction with water-fat separation techniques provides a robust measurement method of in vivo fat fractions [73, 74, 156]. Fat fraction mapping using iterative decomposition with echo asymmetry and least squares estimation (IDEAL) has proven useful in studies which quantified fat content of the liver [157–159] and skeletal muscle [160, 161].

MRI of gastrointestinal (GI) function is an established modality to assess intragastric food distribution and emptying [56] where the in vivo fat quantification plays a key role. To this end, MRI has the ability to apply quantitative measures of how ingested fat is processed and emptied from the stomach [136, 149]. In particular, information regarding the creaming of ingested fat emulsions can be non-invasively obtained [19, 71], which provides information that is of interest from both a food engineering and clinical perspective [139, 162, 163].

Although magnetic resonance (MR) GI tract imaging has many advantages, scan duration in abdominal imaging is often constrained. This constraint is due to breath holding, which is required to suppress respiratory motion. Long breath hold times can be difficult for some patients resulting in reduced subject compliance and hence reduced image quality. Therefore, imaging efficiency must be improved by employing undersampling schemes. Parallel imaging (PI) [164] and compressed sensing (CS) [79] reconstruction exploit the spatial sensitivities of multiple receiver elements

and the sparsity of the images, respectively. They provide the basis for elegant joint schemes, which incorporate water-fat separation directly into the reconstruction process [165–168]. So far, only one prospective undersampled fat fraction quantification technique has been investigated and used to quantify muscle fat in the leg [169]. Although promising, employing undersampling techniques in gastric imaging creates new image processing challenges since the stomach contracts at irregular intervals and there is continuous movement or emptying of intragastric content [55].

The conventional CS framework assumes sparsity in image space or a transformation thereof using a fixed, global sparsity transform such as Wavelets [79]. The use of one particular transform domain for very different anatomical configurations is, however, not optimal and thus might compromise image quality. The use of signal model-based dictionaries has recently gained interest as an alternative to the conventional CS framework [84], allowing the sparsity to be tailored to a specific class of images [83, 85]. The sparsity is enforced in image space, assuming that local image features can be described by a set of patches in a sparsifying dictionary. MR parameter mapping, where multiple acquisitions are collected to derive quantitative maps, is an application of this concept. Similar to the time domain in dynamic imaging, these multiple acquisitions, each acquired at a different parameter value, span a third encoding dimension. By applying prior knowledge along this parameter encoding dimension using a signal model, sparsity can thus be enforced. This variant of CS in parameter space has been applied to the mapping of relaxation times [87–89, 170], where e.g. T_1 maps are reconstructed using an inversion-recovery signal model.

In the present study, the reconstruction of fat fraction maps by applying a water-fat signal model along the echo time dimension is proposed to enable improved intragastric fat quantification in terms of volume and distribution. The method is demonstrated on retrospectively and prospectively undersampled data obtained in healthy subjects after intake of a lipid emulsion drink and compared to conventional parallel imaging reconstruction.

7.2   Methods

7.2.1   Sampling pattern

Prospectively undersampled data was acquired at a reduction factor $R = 4$ using a one-dimensional (1D) undersampling pattern as depicted in Figure 1a, which was identical for all echoes. Since PI reconstruction performance depends on the sampling pattern [171], a uniform under-sampling pattern, which acquires every R-th phase-encoding k_y-line, was modified by randomly shifting k_y-lines by -1, 0, or +1 position along k_y for the outer (82%) of k-space. This allowed for a conventional PI reconstruction approach while exploiting incoherence required for CS schemes.

7.2.2   Signal model-based dictionary

The signal evolution in a multiple echo image series with N different echo times TE_n can be described by a signal model that is based on the spectral multipeak model of the fat of interest with its relative amplitudes β_p and chemical shifts Δf_p of the p-th peak. To this end, the spectral fat model was adapted to the spectrum of rapeseed oil (Figure 1b) as used in the emulsion for in vivo imaging in the present study with its multiple peaks assigned according to [68]. The resulting signal model for each voxel consists of a water and fat component, weighted by their respective water densities ρ_w and fat density ρ_f [74],

$$ s_n = \left(\rho_w + \rho_f \cdot \sum_{p=1}^{P} \beta_p e^{i2\pi \Delta f_p \text{TE}_n} \right) e^{j\left(\psi + j \frac{1}{T_2^*} \right) \text{TE}_n} \, , \qquad (7.1) $$
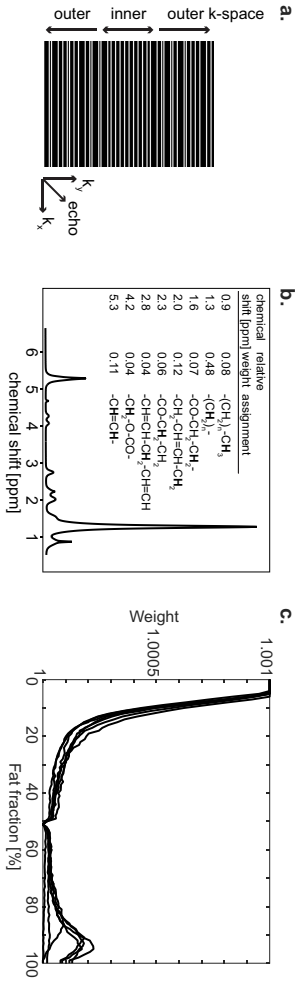
Figure 1 (a) Data acquisition scheme in Cartesian space. A regular undersampling pattern in the center and randomly shifted phase-encoding k_y-lines in outer k-space was applied, which was identical for all echoes. Acquired data lines are shown in white. (b) Spectrum of rapeseed oil. An 8-peak fat model was identified with the corresponding chemical shifts. (c) Individual data-driven weighting functions derived from fat fraction histograms.

where the phase term represents the complex field map and accounts for T_2^* decay and B_0 inhomogeneity ψ of each voxel. Relative fat and water ratios can be replaced in Eq. 7.1 by the fat fraction $\text{ff} = \rho_f/(\rho_f + \rho_w)$ of the voxel to yield the dimensionless signal model,

$$s_n'(\text{ff}, \psi, T_2^*) = \left((1 - \text{ff}) + \text{ff} \cdot \sum_{p=1}^{P} \beta_p e^{j2\pi\Delta f_p \text{TE}_n}\right) e^{j\left(\psi + j\frac{1}{T_2^*}\right)\text{TE}_n} , \qquad (7.2)$$

and expressed by $\boldsymbol{s}'(\text{ff}, \psi, T_2^*) = [s_1'(\text{ff}_1, \psi_1, T_{2,1}^*) \quad \cdots \quad s_N'(\text{ff}_1, \psi_1, T_{2,1}^*)]^T$ as a vector. In practice, $\boldsymbol{s}'(\text{ff}, \psi, T_2^*)$ needs to be normalized, which is already assumed here for simplicity ($\|\boldsymbol{s}'(\text{ff}, \psi, T_2^*)\| = 1$). This 3-parameter model can be represented using an overcomplete dictionary by inserting it into the following equation,

$$\begin{bmatrix} s_1 \\ \vdots \\ s_N \end{bmatrix} = \boldsymbol{D}\boldsymbol{\alpha} \\ = \begin{bmatrix} \boldsymbol{s}'(\text{ff}_1, \psi_1, T_{2,1}^*) \cdots \boldsymbol{s}'(\text{ff}_{L_1}, \psi_{L_2}, T_{2,L_3}^*) \end{bmatrix} \cdot \begin{bmatrix} \alpha_{111} \\ \vdots \\ \alpha_{L_1 L_2 L_3} \end{bmatrix} , \qquad (7.3)$$

where $\boldsymbol{\alpha}$ is the transform domain corresponding to the signal magnitude, $\boldsymbol{D}$ is the transform matrix or dictionary and the parameters ff, ψ, T_2^* are discretized into the respective lengths L_1, L_2 and L_3. Each atom in the dictionary thus represents one possible normalized signal evolution corresponding to a specific ff, ψ and T_2^* value and $\boldsymbol{\alpha}$ represents the scaling factor related to the signal magnitude. By finding the dictionary atom with the best match to the measured echo image series, contributions from aliased signals arising from undersampling can be removed.

7.2.3   Reconstruction of echo images

Reconstruction was performed using Matlab R2015a (MathWorks, Natick, MA). For conventional PI reconstruction, conjugate gradient SENSE (CG-SENSE) [164] with Tikhonov regularization [172] to improve stability

was used, which solves the minimization problem,

$$\arg\min_{\boldsymbol{i}}\|\boldsymbol{F}_u\boldsymbol{S}\boldsymbol{i} - \boldsymbol{d}\|_2^2 + +\lambda_T\|\boldsymbol{i}\|_2\,, \tag{7.4}$$

where $\boldsymbol{d}$ is the acquired k-space data, $\boldsymbol{i}$ is the reconstructed image, $\boldsymbol{S}$ are coil sensitivities for a sensitivity-weighted multicoil image combination [173] and $\boldsymbol{F}_u$ is the undersampled Fourier transform operator, which selects only those k-space locations where data has been acquired. λ_T is the weighting term of the Tikhonov regularization. The minimization was iteratively solved with the conjugate gradient algorithm.

In order to exploit CS in parameter space, the dictionary is incorporated into the reconstruction as an additional dictionary term (DICT),

$$\arg\min_{\boldsymbol{i}}\|\boldsymbol{F}_u\boldsymbol{S}\boldsymbol{i} - \boldsymbol{d}\|_2^2 + +\lambda_T\|\boldsymbol{i}\|_2 + \lambda_D\|\boldsymbol{D}\boldsymbol{\alpha} - \boldsymbol{i}\|_2^2 \,\text{s.t}\,\|\boldsymbol{\alpha}\|_0 \leq 1\,, \tag{7.5}$$

where λ_D is the weighting factor of the dictionary term. The simultaneous search for $\boldsymbol{i}$ and $\boldsymbol{\alpha}$ was implemented by an alternating update of these terms: after each fifth CG-iteration, an orthogonal matching pursuit (OMP) algorithm was added, which searched for the dictionary entry in $\boldsymbol{D}$ with the highest correlation to $\boldsymbol{i}$ and, afterwards updated i accordingly. After the last iteration, the reconstructed image voxels were substituted with a final update of best matching dictionary atoms.

The normalization of each image to its maximum signal intensity allowed the weighting terms to have similar scaling. Figure 2 depicts the ordering in which these steps are performed in the DICT reconstruction.

7.2.4 Selection of DICT parameters

The DICT parameter ranges were based on the IDEAL reconstructions of the fully sampled data, which provided typical estimates for ff, ψ and T_2^*. For ff, the full range from 0 to 100% was used. For ψ and T_2^*, a range from -200 to 200 Hz and 10 to 100 ms was chosen on the basis of the reconstructed complex field maps, respectively. Since signal evolutions for T_2^* values
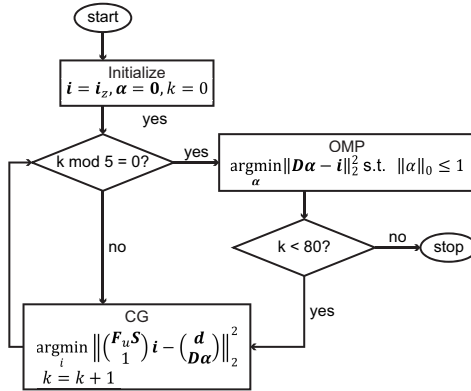
Figure 2 *Algorithm flowchart for DICT reconstruction. After initialization, image i was iteratively updated with the conjugate gradient (CG) algorithm. At every fifth iteration, the dictionary transform domain α was updated using an OMP algorithm. After 80 iterations, the reconstructed image was substituted with a final update of best matching dictionary atoms.*

larger than 100 ms were very similar to each other for the applied echo times, an additional inclusion of $T_2^* = \infty$ into the dictionary sufficiently described voxels with long T_2^*. Using these ranges, the different resolutions were then tested by evaluating the corresponding root mean square error (RMSE) values. Dictionary dimensions were $N = 6$, $L_1 = L_2 = 101$ and $L_3 = 11$, yielding a dictionary with size 6x112211.

To achieve a balance between data consistency and sparsity, L-curve analysis [174] of retrospectively undersampled data was performed and showed that RMSE values were minimized for $\lambda_T = \lambda_D = 0.1$. Alongside, convergence of the iterative image reconstruction was studied yielding a maximum of 80 iterations for both reconstruction methods.

7.2.5 Reconstruction of fat fraction maps

For quantification of fat fraction maps, IDEAL [73] was applied on the echo images reconstructed with both CG-SENSE and DICT.

In order to ensure accurate fat fraction estimation, an additional compu-
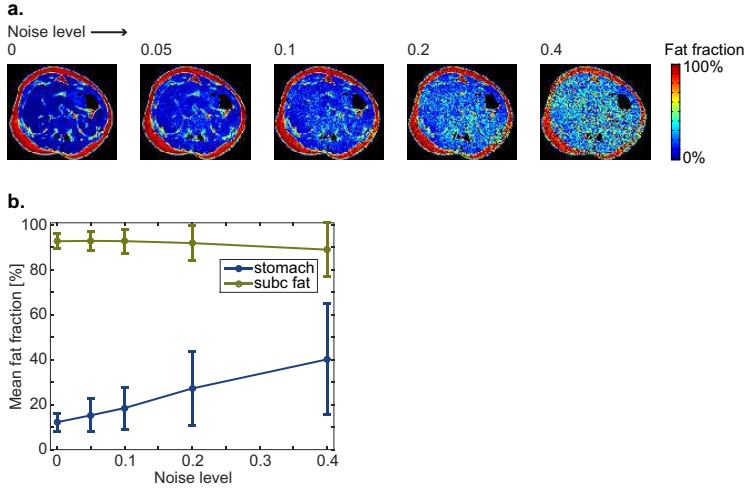
Figure 3 *The effect of different noise levels in the undersampled data on fat fraction quantification. (a) Transverse fat fraction map with different simulated noise levels reconstructed using CG-SENSE. (b) Mean fat fractions in the region of interests (ROIs) of gastric (blue) and subcutaneous (green) fat at the corresponding noise levels. While fat quantification was relatively stable at high fat fractions, low-level fat regions were strongly affected by an increase in noise level.*

tation step was introduced. This step was motivated by the fact that image reconstruction, regardless whether using CG-SENSE or DICT, is dependent on the signal-to-noise ratio (SNR). This dependency was quantified by adding different simulated levels of complex-valued Gaussian noise to the acquired data prior to reconstruction using CG-SENSE. Fat quantification was stable at high fat fractions such as those found in subcutaneous fat. However, low fat fractions as typically found in intragastric content or in the liver were affected and a considerable positive fat fraction bias was introduced as seen in Figure 3.

Knowledge on a priori distributions are frequently incorporated in approaches using Bayesian probability statistics [175]. With dictionaries, this knowledge can be easily implemented by multiplying its normalized atoms with a data-driven weighting function based on the fat fraction histogram,

which favors those entries with a higher weight during the search for the best matching atom in the OMP algorithm. To this end and prior to DICT reconstruction, the fat fraction histogram was derived based on a CG-SENSE reconstruction and comprised all fat fraction values of abdominal tissue (the masking will be described in section 2.7). It reflected the low fat fractions of most abdominal tissue with a small share of high fat fractions due to subcutaneous fat. Larger weights were assigned to dictionary atoms with higher fat fraction probability, i.e. reflecting fat fractions with higher count in the histogram. Weights were maximum 1.001 and minimum 1. Due to the positive fat fraction bias, the fat fraction with the highest count had a higher value in comparison to the fully sampled reference. In order to ensure an adequate representation of the fat fractions lower than this fat fraction, their corresponding weights were adapted to the maximum weight, which resulted in a small plateau of the weighting function. Examples of the resulting weights are shown in Figure 1.

7.2.6 Experiments

This prospective study was approved by institutional and local ethics committees (Cantonal Ethics Commission Zurich). Written informed consent was obtained from all subjects. Seven healthy subjects (mean age ± standard deviation (SD), 24.1 ± 2.7 years; mean body mass index (BMI) ± SD, 21.3 ± 1.0 kg/m^2; two men) were enrolled in the study.

All measurements were performed on a 1.5T whole-body MRI system (Achieva, Philips Healthcare, Best, Netherlands) using a 32-channel phased array torso coil. The subjects were imaged after a minimum of an eight hour fasting period and in right decubitus position. The meal consisted of 200 mL of a rapeseed oil-based emulsion (named lipid emulsion E4 in [19]). After ingestion, the subjects were imaged at three different time points during the gastric emptying process for up to 120 min, yielding a total of 21 datasets. These different states of fat digestion enabled the assessment of a variety of fat fraction values ranging from 0-50%.

All scans were acquired in breathholds using transverse image planes

	Coil calibration	Fully sampled reference	Prospectively undersampled $R = 4$
FOV [mm^3]	350 x 269 x 320	350 x 258 x 160	350 x 258 x 160
Voxel size [mm^2]	6.7 x 6.0	2.3 x 2.3	2.3 x 2.3
Slice thickness [mm]	16	8	8
Matrix size	52 x 45 x 20	152 x 112 x 20	152 x 112 x 20
Phase encoding direction	A→P	R→L	R→L
TR [ms]	4.0	10.0	10.0
# Echoes	1	6	6
TE1 / dTE [ms]	0.7	1.0 / 1.6	1.0 / 1.6
FA [°]	7	10	10
Total scan duration [s]	14	36	8 (+4*)
# Breath holds	1	2	1

Table 7.1 *Imaging parameters.*
* Due to the fewer phase-encoding lines, an optimized startup cycle prior to data acquisition was performed in order to reach a steady-state (13 dummy cycles at flip angles 25° and a 200 ms pause before acquisition).

with parameters given in Table 7.1. Due to the fewer phase-encoding lines in prospectively undersamped imaging, dummy cycles prior to data acquisition were performed in order to establish steady-state. The resulting optimized startup for typical intragastric T_1 and T_2 values ($T_1 = 200$-3000 ms, $T_2 = 50$-2000 ms) consisted of 13 dummy cycles at flip angles 25°, followed by a 200 ms recovery period [176]. For the measurement of fat fraction maps, fully sampled reference and prospectively undersampled data using a two-dimensional (2D) spoiled multi-gradient echo sequence with 6 echo times and flyback gradients were acquired. Coil sensitivities were estimated using a separate coil calibration scan. In order to ensure similar breathhold positions between coil calibration and target scans, pencil beam respiratory navigator gating on the right hemi-diaphragm [177] was used to trigger each scan.

7.2.7   Data analysis and statistics

Datasets consisted of the prospectively undersampled data and the retrospectively undersampled data, with the latter derived by retrospectively undersampling of the fully sampled reference. Both datasets were reconstructed with the two methods, CG-SENSE and DICT for comparison. For the assessment of reconstruction performance of each echo time image, comparisons were performed between the retrospectively undersampled data and the fully sampled reference. Prospective data was acquired in a separate scan and hence a voxel-by-voxel comparison was not possible due to physiological differences. Instead an error analysis was performed for two ROIs: segmented intragastric content and abdominal tissue in general. For the latter ROI, transverse abdominal image slices were thresholded based on 0.2 of the maximum magnitude signal intensity. This signal threshold was chosen to mask out the background and air in-between tissues. Only slices with GI content were used for analysis. Segmentation of intragastric content was performed with a custom-built semiautomatic segmentation tool [137]. Error quantification was based on the normalized RMSE of each slice,

$$
\text{RMSE} = \log \left(\frac{\sqrt{\sum_i |\boldsymbol{I}_i - \boldsymbol{R}_i|^2}}{\sqrt{\sum_i |\boldsymbol{R}_i|^2}} \right), \tag{7.6}
$$

where R_i is the fully sampled reference and I_i the retrospectively undersampled data reconstructed with either CG-SENSE or DICT of the i-th voxel in the ROI. The log-transformation was used in order to correct for distributional abnormality. Differences between the two reconstruction methods were analyzed by linear effects modeling, taking into account method and echo time as fixed effects. Model parameters are presented as mean ± standard error of the estimates. All statistical analysis was performed using R 3.1.3 [138].

The agreement of calculated fat volumes from retrospectively or prospectively undersampled data relative to the fully sampled reference was

tested using Bland-Altman analysis [178]. Again, the analysis was per-formed separately for CG-SENSE and DICT reconstruction.

In order to test the agreement in the measured fat distributions, fat fractions were averaged at each level along the direction of gravity. This step generated so-called intragastric fat fraction profile plots [110]. The fat fraction profiles were then compared against the reference by linear regression. Resulting estimates were presented as mean (95% confidence interval (CI)).

7.3   Results

Each of the 21 datasets yielded 10 to 19 slices of abdominal tissue, 7 to 17 slices of intragastric content and 26 to 47 levels along the direction of gravity, depending on the subject. A total of 329 ROIs of abdominal tissue, 270 ROIs of intragastric content and 752 levels of intragastric emulsion profiles were thus available for statistical analysis. Image reconstruction per dataset required approximately 10 minutes for CG-SENSE and 40 minutes for DICT on standard desktop computer hardware (CPU 3.6 GHz, 16 GB RAM).

7.3.1   Echo images

Figure 4 demonstrates reconstructions of individual echo images from CG-SENSE and DICT. The CG-SENSE images exhibit enhanced noise in the central part of the abdomen which obscures anatomic features such as ves-sels in the liver. In contrast, the DICT approach reduced noise and reveals details in these regions, offering a higher quality of image reconstruction than the conventional CG-SENSE method.
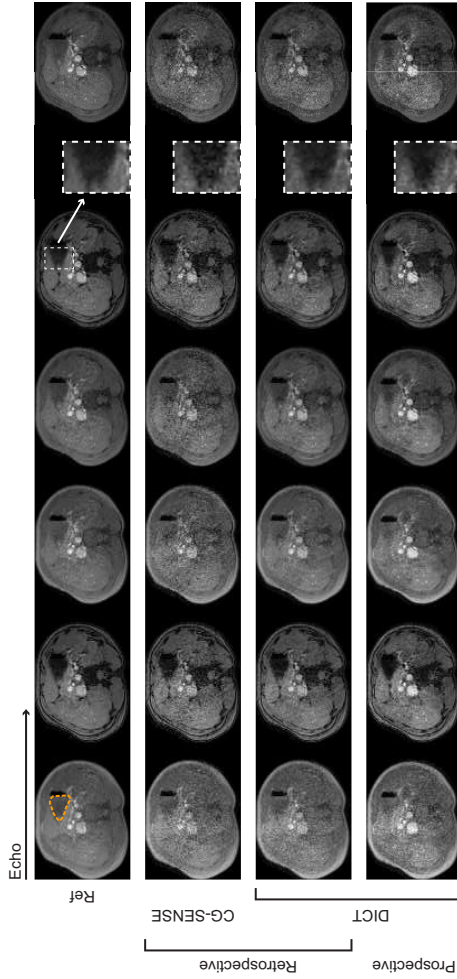
Figure 4 *Individual echo image series of one subject. The fully sampled reference (top row) and the different reconstructions of retrospectively undersampled data (subsequent rows) are shown. The gastric content is delineated by the dashed orange line. Zoomed-in images of the fifth echo show that the DICT reconstruction resulted in reduced noise and better revealed anatomic details when compared to CG-SENSE.*
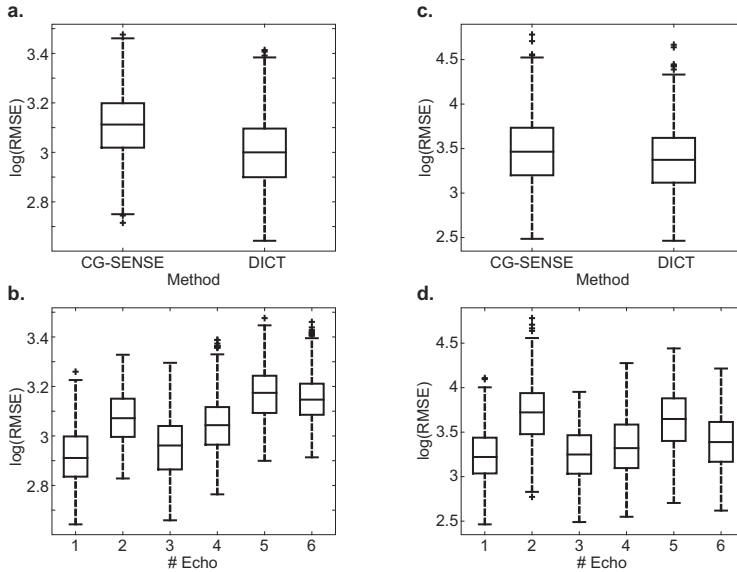
Figure 5 *Summary of the error analysis on the log-transformed RMSE values. The box plots show the comparison of the RMSE generated by the two reconstruction methods (a, c) and the individual echoes (b, d) for abdominal tissue (a, b) and intragastric content (c, d). RMSE values were lower for the DICT reconstruction.*

Figure 5 presents the log-transformed RMSE values generated by CG-SENSE and DICT for the two ROIs indicated in Figure 4. The RMSE for abdominal tissue reconstructed by CG-SENSE was 2.97 ± 0.03. There was a significant decrease of RMSE values for DICT with a difference of ΔRMSE=0.10 ± 0.003 (P<0.001). RMSE increased by 0.05 ± 0.001 with increasing echo number (P<0.001). The RMSE for intragastric content using CG-SENSE was 3.35 ± 0.05 while a significant decrease was observed for DICT, ΔRMSE=0.170 ± 0.01 (P<0.001). Although an increase of RMSE by 0.02 ± 0.003 (P<0.001) with increasing echo number was also significant (P<0.001), echo #2 produced the largest errors (RMSE=3.64 ± 0.01) followed by echo #5 (RMSE=3.56 ± 0.01) when intragastric content was considered.

7.3.2   Fat fraction maps

Figure 6 demonstrates the reconstructed fat fraction maps of subjects with different intragastric fat distributions. Fat fraction maps of the intragastric content of the undersampled acqusitions are noisier in comparison to the signal distribution of the fully sampled reference. However, both retrospectively and prospectively undersampled DICT reconstructions were in agreement with the fully sampled reference maps. In contrast, fat fractions from CG-SENSE yielded a positive offset, i.e. higher values than in the reference. This was predominantly caused by a "noise floor" that was produced at low fat fractions. The agreement between the quantified intragastric fat volumes extracted from the fully sampled and undersampled data sets is assessed using Bland-Altman plots in Figure 7. In accordance to the observations made in the fat fraction maps, CG-SENSE produced a positive bias of 2.1 ± 1.3 mL and upper and lower confidence limits of 5.4 and -1.1 mL, respectively, indicating an overestimation of fat volumes. An overestimation did not occur with the DICT reconstruction where the bias was at -0.1 ± 0.7 mL with upper and lower confidence limits of 1.8 and -2.0 mL, respectively. The prospectively undersampled data with DICT reconstruction also showed no overestimation with a bias of -0.01 ± 1.5 mL, however, the upper and lower confidence limits at 3.9 and -4.0 mL were larger.
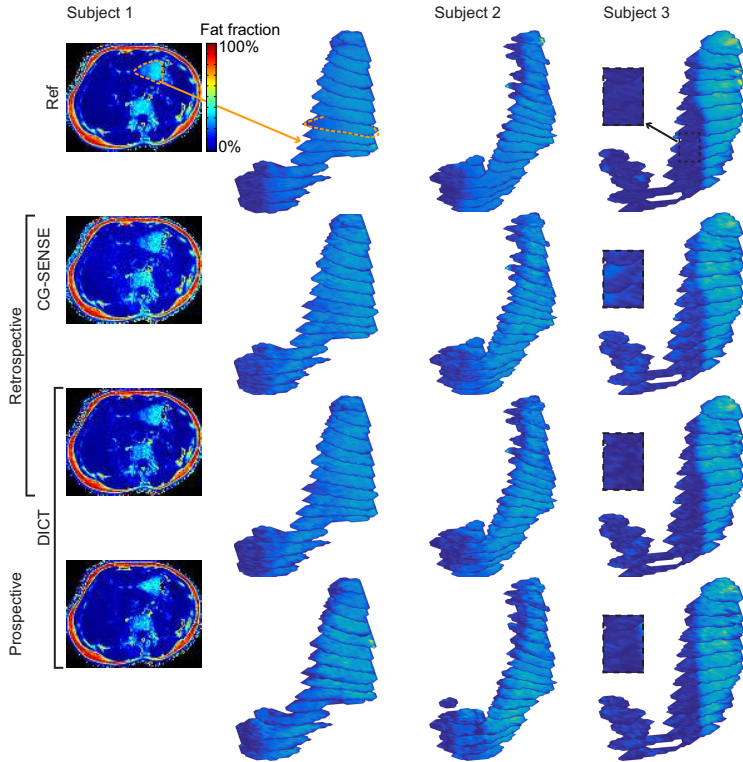
Figure 6 *Reconstructed fat fraction maps, showing the fully sampled reference, the CG-SENSE reconstruction, the DICT reconstruction of retrospective and prospective data (top to bottom rows). An exemplary transverse slice with delineated stomach (dashed orange line) and the corresponding entire gastric content volume are presented in the first and second column, respectively. Two additional exemplary gastric content volumes showing different intragastric fat distributions are presented in the third and fourth column. Zoomed-in gastric content volumes show that whereas a noise floor is observed with the CG-SENSE reconstruction at low fat fractions, the DICT reconstruction was in agreement to the reference.*

Reconstructed fat fraction maps, showing the fully sampled reference, the CG-SENSE reconstruction, the dictionary (DICT) reconstruction and the DICT reconstruction of prospective data (top to bottom rows). An exemplary transverse slice with delineated stomach (dashed orange line) and the corresponding entire gastric content volume are presented in the first and second column, respectively. Two additional exemplary gastric content volumes showing different intragastric fat distributions are presented in the third and fourth column. Zoomed-in gastric content volumes show that whereas a noise floor is observed with the CG-SENSE reconstruction at low fat fractions, the DICT reconstruction was in agreement to the reference.

Figure 8a demonstrates the correlation between the fat fraction profiles from DICT reconstruction and the reference. The linear fit resulted in a slope of 1.01 (0.99 to 1.02) and an offset of -0.5 (-0.81 to -0.22), respectively, and a correlation coefficient R^2=0.956, P<0.001. In comparison, the linear fit of CG-SENSE resulted in a slope of 1.05 (1.03 to 1.07) and offset -2.9 (-3.3 to -2.6), R^2=0.952, P<0.001. An example of an intragastric emulsion profile plot is given in Figure 8b and illustrates how the ingested unstable emulsion underwent creaming and separated into two layers. Although the overall trend of creaming was distinguishable in the emulsion profiles, the undersampled data produced additional noise on the fat fraction values, causing local biases in the profile curves.

7.4   Discussion

In this work an accelerated MRI acquisition with a dictionary-based re-construction approach (DICT) in the parameter domain has been proposed for intragastric fat quantification. Improved image quality and accuracy in gastric fat fraction quantification compared to conventional parallel imaging (CG-SENSE) was achieved.
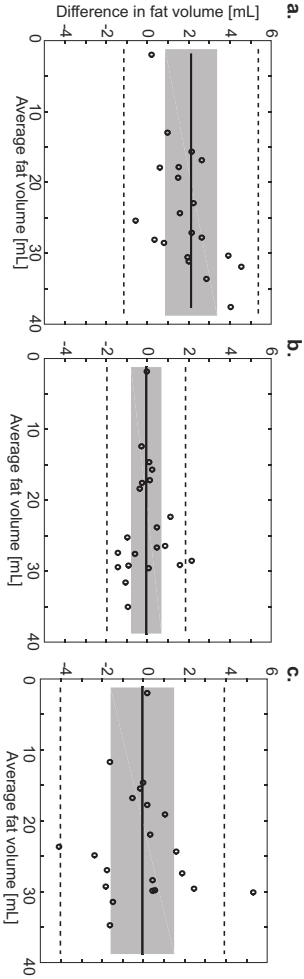
Figure 7 *Agreement of quantified intragastric fat volumes. Bland-Altman plots comparing the fully sampled reference and (a) CG-SENSE reconstruction, (b) retrospectively undersampled DICT reconstruction and (c) prospectively undersampled DICT reconstruction, respectively. Bias (solid line) and standard error (shaded area) show that the DICT approach is in agreement with the reference. The larger lower and upper limits of agreement (dashed lines) of the prospectively undersampled DICT reconstruction indicate a larger variance in fat quantification.*

For good reconstruction results, the choice of the three parameters ff, ψ and T_2^* in the dictionary with regards to their resolution and range is crucial. If a given parameter value is not included in the dictionary, the reconstruction will yield the closest value in the dictionary. Therefore, it is desirable to cover the whole range present in the data at high resolution. However, the computation time is proportional to the number of atoms in the dictionary. Thus, a compromise must be made to balance the accuracy and the computation time. In this study, a dictionary with size 6x112211 was chosen, which resulted in 4-times longer reconstruction times in comparison to CG-SENSE. A compression of the dictionary using K-SVD to expedite image reconstruction, as it is commonly applied in patch-based dictionary learning algorithms [83, 85, 87], was not used since computation times were not the primary focus of this study.

As indicated in previous works, incoherence in parameter direction could be increased in a gradient echo sequence by randomly shifting k_y-lines with blipping gradients [166], producing a different undersampling pattern for each echo. However, in vitro test measurements showed that gradient blipping resulted in phase distortions probably due to eddy currents, which induced phase errors and thus hampered the estimation of fat fractions. Therefore, the undersampling pattern was chosen to be identical for all echoes.

In conventional PI using CG-SENSE, the acceleration of data acquisition causes an apparent SNR loss. The noise amplification in the echo images was most evident in the center of the abdomen, which corresponds to regions of high g-factor values [179]. The DICT approach resulted in a reduction of the noise in these regions. This aided in the preservation of the details and edges of tissues and decreased the error in the echo images by 11%. The error increased with increasing echo number, i.e. longer echo times (TEs), and consequently larger losses due to T_2^* decay. The increase in error with echo number was further amplified in the out-of-phase echoes (second and fifth echo) due to their lower signal intensities compared to the in-phase echoes. These findings indicate that the SNR dependence of the
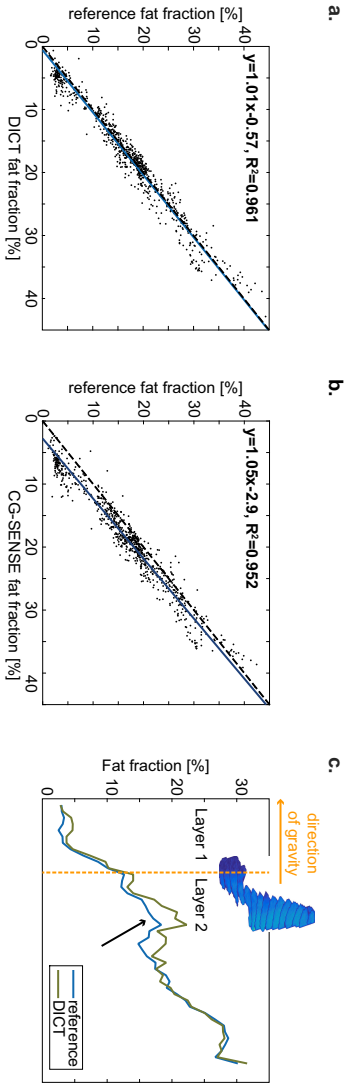
Figure 8 *Comparison of the intragastric fat fraction profiles. Correlation plot with fat fraction values of the reference against those of the (a) DICT reconstruction (dots) and (b) CG-SENSE reconstruction (dots) including the line of identity (dashed line) and the computed linear fit (blue line). (c) Exemplary intragastric profile of the reference (blue) and DICT reconstruction (green). A good agreement for the characteristics of the intragastric profiles was achieved, however, some localized biases are present (black arrow).*

DICT reconstruction performance is modulated by both signal dephasing and water-fat phase shifts as expected. The spatially dependent noise floor in CG-SENSE resulted in an overestimation of intragastric fat volumes at low fat fractions. This is due to the properties of IDEAL at low fat fractions, where complex signal fluctuations that originate from noise may be falsely interpreted as signal and thus lead to an overestimation of the fat fraction.

A Bayesian inspired approach was introduced for the DICT reconstruction to weight the dictionary atoms based on a prior, data-driven probability distribution of fat fraction. This step removed the noise floor and therefore the bias in intragastric fat volume quantification and fat layer analysis. The weighting function was very similar among the investigated healthy subjects, such that the use of one single weighting function for all datasets was considered feasible. However, for the application to obese subjects, e.g. for fatty liver applications, the body composition is expected to change drastically, which influences the shape of the weighting functions. Thus, the use of individual, data-driven weights as used in the present study will preserve the general applicability of the method.

In GI imaging, acquiring two reproducible image datasets is challenging due to differences in breathhold position, continuous gastric motility and gastric emptying. Whereas the effect of breathhold position could be adressed by navigator guided breathholds, the irregularity of the other effects prohibits cyclic acquisition schemes such as employed in cardiac imaging. The error analysis based on a direct voxel-by-voxel comparison and the fat distribution analysis based on profile-by-profile comparisons were therefore not possible between the prospectively and retrospectively undersampled datasets. Nevertheless, the fat volume quantification of prospectively undersampled fat fraction data demonstrates good agreement with the reference values. However, larger limits of agreement were observed in comparison to the retrospectively undersampled data. This can be attributed to the irregular motion as described above, which reduced agreement in the fat volumes with the fully sampled data.

Acceleration of image acquisition inherently implies an SNR penalty.

Hence, compared to the fully sampled data, the fat fraction maps derived from undersampled DICT reconstruction of the intragastric content were noisier. The noise caused local biases reducing the accuracy of the spatial distribution of intragastric fat. Therefore, inference on the degree of intragastric coalescence or flocculation of fat droplets must be made with caution. DICT included prior knowledge of the abdominal MR signal in form of a two-compartment signal model-based dictionary. The fat model spectrum was matched to that of the ingested fat, i.e. rapeseed oil and not to the specta of visceral and subcutaneous fat. It has, however, been argued that the specific choice of fat model has only a minor impact on resulting quantification [180] and hence no further refinement of the fat signal model was attempted in the present study. Another potential limitation relates to the accuracy of absolute fat quantification pertaining to T_1-bias, which is a result of the selection of flip angle (FA) and repetition time (TR) [152]. This did not influence the primary outcome of this study, since T_1-bias equally affected the CG-SENSE and DICT reconstruction. A modification of the present method for removing T_1-bias will, however, be addressed in future work.

In conclusion, accelerated abdominal MRI by means of integrating a dictionary-based signal model into image reconstruction allows for improved quantification of intragastric fat. This approach holds also potential for rapid fat quantification of other abdominal tissues where long breath holds are an issue. The proposed method is of special interest for clinical nutrition in the development and validation of nutritional interventions to curb e.g. type II diabetes and obesity.

8 Discussion & Outlook

8.1 Discussion

In this thesis, fast quantitative methods for in vivo magnetic resonance imaging (MRI) studies on fat emulsions have been presented. The developed techniques include the non-invasive monitoring of fat emulsion processing in the stomach in terms of fat content, gastric secretion content and their interrelation. The immediate applicability of these quantification techniques has been shown on fat emulsions of different stability in human MRI studies with healthy subjects.

Accurate quantification of fat emulsions require the signal model used in the estimation to be consistent with the underlying physics. In fat emulsions, off-resonant compartments due to the different chemical shifts of fat affect the total signal intensity. In particular, it was shown in fast steady-state sequences such as double echo steady-state (DESS) and triple echo steady-state (TESS) that the multi-compartment property of fat emulsions induced periodical signal modulations dependent on the choice of echo time (TE). This presents an important confounding factor for T_2 quantification, which results in erroneous offsets of the estimated values. Although, whenever fat is present, significant implications for quantitative parameter mapping in phantoms and in vivo tissue may be expected, the multi-compartment effect can be leveraged when applying a suitable multi-compartment model, as was shown for the estimation of fat fractions in fat emulsions.

Iterative decomposition with echo asymmetry and least squares estima-

tion (IDEAL) allows for a robust separation of the measured signal into its water and fat compartments. The application of IDEAL for fat quantification in emulsions was validated both in vitro and in vivo by using a series of diluted emulsion samples and gastric aspirates, respectively. IDEAL enabled to visualize gastric and duodenal fat distributions of a stable and an unstable emulsion. For the stable emulsion, fat distributed homogeneously in the stomach and was increasingly diluted with gastric secretion. The unstable emulsion showed highly variable gastric fat distributions and a strong degree of creaming with an associated bi-phasic layering. Its fat emptying rate was faster than the stable emulsion by approximately 41%. In the lower gastrointestinal (GI) tract, feasibility of fat quantification still needs to be investigated since first, fat fractions possibly fall below the limit of accuracy and second, the disintegration of the ingested fat may cause the fat model to be no longer valid. In the upper GI tract, quantitative MRI not only revealed information about the complexity of food structuring during digestion, but also gave insight into the fate of the fat component with regard to emptying and its characteristics under forces such as trituration and peristaltic activity.

   With the combination of fat and T_1 quantification, the mapping of emulsified fat and gastric secretion concentration inside the stomach was achieved. In the corresponding in vivo study, the effects of emulsion stability on gastric secretion volume and intragastric mixing could be additionally revealed. Intragastric fat layering was mainly influenced by the degree of intragastric mixing rather than the overall volume dominance of secretion. The stable fat emulsion triggered a higher accumulation of gastric secretion, which in turn facilitated homogenization of intragastric content in comparison to its unstable counterpart. The applied LinExp model offered a more differential insight into fat emptying dynamics than the linear model applied in the previous IDEAL study, which confirmed the faster fat volume emptying of the unstable emulsion and in addition, detected a longer emptying delay of fat. The largest source of measurement bias potentially arose from the increased measurement inaccuracies at high T_1

values corresponding to high secretion concentrations. However, critically high concentrations mostly occurred in largely reduced stomach volumes during the late phase of gastric emptying, limiting the impact of the errors. Therefore, the behavior of emulsions in interaction with digestive processes in the stomach allows to be described in a detail with the combined fat fraction and secretion mapping scheme.

Acceleration in gastric MRI, where long breath holds are an issue, was addressed by integrating a signal model-based dictionary into image reconstruction at an acceleration factor $R = 4$. Compared to conventional parallel imaging (PI), this allowed for improved image quality and increased accuracy of fat quantification during short breath holds. It was found that PI reconstruction produced a noise floor and therefore, a positive bias in intragastric fat volumes. To this end, a Bayesian inspired approach was introduced for the proposed reconstruction to weight the dictionary with a prior, data-driven probability distribution of fat fractions. Due to the acceleration, a reduced accuracy of the spatial fat distributions was observed in the reconstructions of undersampled data compared to the fully sampled data. Although this implied that inference on the degree of intragastric flocculation of fat droplets must be made with caution, accelerated abdominal MRI by means of the proposed reconstruction scheme allows for improved quantification of intragastric fat volumes.

8.2   Outlook

Quantitative MRI has huge potential to improve the in vitro-in vivo correlation of current digestive models for developing effective functional emulsions. To this day, related methods have been applied in only a handful of studies and therefore, there is still plenty of space for future study designs in order to fully exploit their potential. The studies that have been conducted within the scope of this thesis can be extended in multiple dimensions.

First, combining MRI-based studies with concurrent measurements

using complementary techniques such as blood sampling and subsequent analysis of GI hormone and macronutrient profiles will provide information on the endocrine impact and the metabolization of the fat emulsions. Questionnaires will allow the assessment of visceral sensation and symptom scores (e.g. fullness, hunger, bloating etc.) to study behavioral effects.

Second, the developed methods are in principle, not limited to the gastroduodenal part of the digestive tract. In fact, the next major milestone in fat quantification lies in the small intestine of the lower GI tract. Here, the large flux of intraluminal contents, the complexity of the organ's geometry and inherently lower fat contents compared to those in the stomach due to the dilution by both gastric and intestinal secretions remain the three challenging obstacles for imaging the lower GI tract. Since the small intestine is also the main site of fat absorption and triggers the ileal brake, crucial outcomes are expected from the fat content measurement. For a reliable and robust fat quantification, the current limit of accuracy and detection must be increased. In addition, the disintegration of fat due to digestive enzymes in intestinal secretion causes the fat to be broken up into free fatty acids and thus, the underlying spectral fat model may be no longer valid. Spectroscopic approaches or hybrid spectroscopic imaging approaches [181] could potentially be applied for analyzing the fat spectrum in the lower GI tract. Another approach is to employ reconstruction schemes with a more flexible fat model where, instead of resolving the water and the ensemble of fat peaks, a few fat peaks can be detected independently [182]. In general, the higher accuracies of these approaches come at the cost of higher signal-to-noise ratio (SNR) requirement levels, associated with acquisition times typically longer than one breath hold. Possible techniques to abolish breath hold constraints is to employ prospective motion compensation schemes, such as gated free-breathing acquisitions, or retrospective motion compensation schemes, such as reference interleaves.

Last, follow-up studies that include both healthy subjects and patients in nutritional disease states such as diabetes and obesity will provide a greater understanding in the control of energy intake especially from the clinical

perspective. These findings could facilitate the development of tailored emulsions for eating disorder treatment and related health care. The initial step towards this direction has been laid with the proposed acceleration method that has the potential to be adapted to patients where breath holds are typically restricted to 10-15 s scan durations. The inclusion of obese patients for imaging studies leads to another fundamental consideration related to the static magnetic field strength. A 1.5 T system was used for most of the work described in the thesis. A wide bore 3 T system would offer more space for obese patients that cannot fit into conventional magnetic resonance (MR) scanners. The adaption of the presented methods to 3 T would benefit from elevated SNR levels but the increased influence of B_0 and B_1 inhomogeneities on quantification performance needs to be investigated for these purposes.

For large studies, image post-processing should be optimized. The semi-automatic segmentation of stomach content, which takes 1-2 hours for each exam per subject, constitutes one of the most tedious tasks in data analysis. The main issue arising from it is the often ambiguous delineation of the stomach wall. In the presence of gastric motor activity and different breath hold positions between the scans, this becomes problematic. Thus, when applying the contours of the high-contrast anatomical scans to quantitative fat and secretion maps, contour readjustments are required even if breath hold positions lie within the expected navigator tolerance. Future scan protocols should explore strategies for optimizing the order of data acquisition to achieve the best inter-scan alignment possible.

Although this thesis focused on two fat emulsions of highly artificial composition in order to develop quantitative MRI methods, they are not limited only to these emulsions. Other fat emulsions can be employed as well, offering the possibility to choose between a wide range of vegetable and dairy oils and emulsions found in everyday foods. By replacing the spectral fat model with the appropriate fat under consideration, the substitution of the emulsion becomes straightforward. However, special care needs to be given for foods that form solid particles during passage through the GI

tract, as they might cause signal voids in the MR images and make these structures undetectable.

In conclusion, this work offers scientists and nutritionists robust tools that will help them both to gain a deeper understanding of the human digestive tract, and to perform in vivo monitoring of fat emulsions.

Acronyms

1D	one-dimensional
2D	two-dimensional
3D	three-dimensional
AFI	actual flip angle imaging
BMI	body mass index
CA	contrast agent
CCK	cholycystokinin
CG	conjugate gradient
CI	confidence interval
CS	compressed sensing
DESS	double echo steady-state
DFA	dual flip angle
DREAM	dubbed dual refocusing echo acquisition mode
FA	flip angle
FFT	fast Fourier transform
FOV	field of view
FV	fat volume
Gd	Gadolinium
GI	gastrointestinal
GLP-1	glucagon-like peptide
IDEAL	iterative decomposition with echo asymmetry and least squares estimation
IR	inversion recovery

IST	iterative shrinkage thresholding
LinExp	linear exponential
MR	magnetic resonance
MRI	magnetic resonance imaging
MRS	magnetic resonance spectroscopy
OMP	orthogonal matching pursuit
PI	parallel imaging
PRESS	point resolved spectroscopy
PYY	peptide tyrosine tyrosine
RF	radiofrequency
RMSE	root mean square error
ROI	region of interest
SD	standard deviation
SE	spin echo
SENSE	sensitivity encoding
SGF	simulated gastric fluid
SNR	signal-to-noise ratio
SSFP	steady-state free precession
STEAM	stimulated echo acquisition mode
SV	secretion volume
TCV	total content volume
TE	echo time
TESS	triple echo steady-state
TI	inversion time
TR	repetition time

References

[1] Aken GA. Relating food emulsion structure and composition to the way it is processed in the gastrointestinal tract and physiological responses: what are the opportunities? *Food Biophys*, 5(4):258–283, 2010.

[2] Carey MC, Small DM, and Bliss CM. Lipid digestion and absorption. *Annu Rev Physiol*, 45:651–77, 1983.

[3] Fave G, Coste TC, and Armand M. Physicochemical properties of lipids: new strategies to manage fatty acid bioavailability. *Cell Mol Biol*, 50(7):815–31, 2004.

[4] Porter CJ, Trevaskis NL, and Charman WN. Lipids and lipid-based formulations: optimizing the oral delivery of lipophilic drugs. *Nat Rev Drug Discov*, 6(3):231–48, 2007.

[5] Christensen JO, Schultz K, Mollgaard B, Kristensen HG, and Mullertz A. Solubilisation of poorly water-soluble drugs during in vitro lipolysis of medium- and long-chain triacylglycerols. *Eur J Pharm Sci*, 23(3):287–96, 2004.

[6] Borel P, Grolier P, Armand M, Partier A, Lafont H, Lairon D, and Azais-Braesco V. Carotenoids in biological emulsions: solubility, surface-to-core distribution, and release from lipid droplets. *J Lipid Res*, 37(2):250–61, 1996.

[7] Ostlund, R. E. J. Phytosterols in human nutrition. *Annu Rev Nutr*, 22:533–49, 2002.

[8] Gaillard D, Passilly-Degrace P, and Besnard P. Molecular mechanisms of fat preference and overeating. *Ann N Y Acad Sci*, 1141:163–75, 2008.

[9] Chan M. Opening address. In *8th Global Conference on Health Promotion*, Helsinki, Finland, 2013.

[10] Fiszman S and Varela P. The satiating mechanisms of major food constituents - an aid to rational food design. *Trends Food Sci Technol*, 32(1):43–50, 2013.

[11] McClements D. *Food Emulsions: Principles, Practices, and Techniques*. CRC Press, 2015.

[12] Lundin L, Golding M, and Wooster TJ. Understanding food structure and function in developing food for appetite control. *Nutr Diet*, 65:S79–S85, 2008.

[13] Halford JC and Harrold JA. Satiety-enhancing products for appetite control: science and regulation of functional foods for weight management. *Proc Nutr Soc*, 71(2):350–62, 2012.

[14] Gidley MJ. Hydrocolloids in the digestive tract and related health implications. *Curr Opin in Colloid Interface Sci*, 18(4):371–378, 2013.

[15] Norton I, Moore S, and Fryer P. Understanding food structuring and breakdown: engineering approaches to obesity. *Obes Rev*, 8:S83–8, 2007.

[16] Marciani L, Wickham MSJ, Bush D, Faulks R, Wright J, Fillery-Travis AJ, Spiller RC, and Gowland PA. Magnetic resonance imaging of the behaviour of oil-in-water emulsions in the gastric lumen of man. *Br J Nutr*, 95(2):331–339, 2006.

[17] Marciani L, Wickham M, Singh G, Bush D, Pick B, Cox E, Fillery-Travis A, Faulks R, Marsden C, Gowland PA, and Spiller RC. Enhancement of intragastric acid stability of a fat emulsion meal delays gastric emptying and increases cholecystokinin release and gallbladder contraction. *Am J Physiol Gastrointest Liver Physiol*, 292(6):G1607–13, 2007.

[18] Marciani L, Faulks R, Wickham MSJ, Bush D, Pick B, Wright J, Cox EF, Fillery-Travis A, Gowland PA, and Spiller RC. Effect of intragastric acid stability of fat emulsions on gastric emptying, plasma lipid profile and postprandial satiety. *Br J Nutr*, 101(6):919–928, 2009.

[19] Steingoetter A, Radovic T, Buetikofer S, Curcic J, Menne D, Fried M, Schwizer W, and Wooster TJ. Imaging gastric structuring of lipid

emulsions and its effect on gastrointestinal function: a randomized trial in healthy subjects. *Am J Clin Nutr*, 101(4):714–24, 2015.

[20] Meyers M, Charnsangavej C, and Oliphant M. *Meyers' Dynamic Radiology of the Abdomen*. Springer, 2011.

[21] Krishnamurthy R, Cheong B, and Muthupillai R. Tools for cardiovascular magnetic resonance imaging. *Cardiovasc Diagn Ther*, 4(2):104–25, 2014.

[22] Musse M, Quellec S, Devaux MF, Cambert M, Lahaye M, and Mariette F. An investigation of the structural aspects of the tomato fruit by means of quantitative nuclear magnetic resonance imaging. *Magn Reson Imaging*, 27(5):709–19, 2009.

[23] Mariette F. Investigations of food colloids by NMR and MRI. *Curr Opin Colloid Interface Sci*, 14(3):203–211, 2009.

[24] Le Feunteun S and Mariette F. Effects of acidification with and without rennet on a concentrated casein system:? a kinetic NMR probe diffusion study. *Macromolecules*, 41(6), 2008.

[25] Treier R, Steingoetter A, Goetze O, Fox M, Fried M, Schwizer W, and Boesiger P. Fast and optimized T1 mapping technique for the non-invasive quantification of gastric secretion. *J Magn Reson Imaging*, 28(1):96–102, 2008.

[26] Agboola SO and Dalgleish DG. Effects of pH and ethanol on the kinetics of destabilisation of oil-in-water emulsions containing milk proteins. *J Sci Food Agr*, 72(4):448–454, 1996.

[27] Chanamai R and McClements DJ. Comparison of gum arabic, modified starch, and whey protein isolate as emulsifiers: influence of pH, CaCl2 and temperature. *J Food Sci*, 67(1):120–125, 2002.

[28] Dickinson E. *Food Hydrocolloids: Structures, Properties, and Functions*. Springer, 1993.

[29] Singh H, Ye A, and Horne D. Structuring food emulsions in the gastrointestinal tract to modify lipid digestion. *Prog Lipid Res*, 48(2):92–100, 2009.

[30] Cummings DE and Overduin J. Gastrointestinal regulation of food intake. *J Clin Invest*, 117(1):13–23, 2007.

[31] Blundell J, De Graaf C, Hulshof T, Jebb S, Livingstone B, Lluch A, Mela D, Salah S, Schuring E, Van Der Knaap H, and Westerterp M. Appetite control: methodological aspects of the evaluation of foods. *Obes Rev*, 11(3):251–270, 2010.

[32] McClements DJ, Decker EA, and Park Y. Controlling lipid bioavailability through physicochemical and structural approaches. *Crit Rev Food Sci Nutr*, 49(1):48–67, 2009.

[33] McClements DJ and Li Y. Review of in vitro digestion models for rapid screening of emulsion-based systems. *Food Funct*, 1(1):32–59, 2010.

[34] Johnson LR. *Physiology of the Gastrointestinal Tract*. Academic Press, 2006.

[35] Sek L, Porter CJ, and Charman WN. Characterisation and quantification of medium chain and long chain triglycerides and their in vitro digestion products, by HPTLC coupled with in situ densitometric analysis. *J Pharm Biomed Anal*, 25(3-4):651–61, 2001.

[36] Dahan A and Hoffman A. Use of a dynamic in vitro lipolysis model to rationalize oral formulation development for poor water soluble drugs: correlation with in vivo data and the relationship to intra-enterocyte processes in rats. *Pharm Res*, 23(9):2165–74, 2006.

[37] Yoo JY and Chen XD. GIT physicochemical modeling - a critical review. *Int J Food Eng*, 2(4), 2006.

[38] Golding M, Wooster TJ, Day L, Xu M, Lundin L, Keogh J, and Clifton P. Impact of gastric structuring on the lipolysis of emulsified lipids. *Soft Matter*, 7(7):3513–3523, 2011.

[39] McClements DJ and Xiao H. Potential biological fate of ingested nanoemulsions: influence of particle characteristics. *Food Funct*, 3(3):202–20, 2012.

[40] Thi TD, Van Speybroeck M, Barillaro V, Martens J, Annaert P, Augustijns P, Van Humbeeck J, Vermant J, and Van den Mooter G. Formulateability of ten compounds with different physicochemical profiles in SMEDDS. *Eur J Pharm Sci*, 38(5):479–88, 2009.

[41] Dahan A and Hoffman A. The effect of different lipid based formulations on the oral absorption of lipophilic drugs: the ability of in vitro

lipolysis and consecutive ex vivo intestinal permeability data to predict in vivo bioavailability in rats. *Eur J Pharm Biopharm*, 67(1):96–105, 2007.

[42] Versantvoort CH, Ondrewater RC, Duizer E, Van de Sandt JJ, Gilde AJ, and Groten JP. Monolayers of IEC-18 cells as an in vitro model for screening the passive transcellular and paracellular transport across the intestinal barrier: comparison of active and passive transport with the human colon carcinoma caco-2 cell line. *Environ Toxicol Pharmacol*, 11(3-4):335–44, 2002.

[43] Ferrua MJ and Singh RP. Modeling the fluid dynamics in a human stomach to gain insight of food digestion. *J Food Sci*, 75(7):R151–62, 2010.

[44] Steinert RE, Beglinger C, and Langhans W. Intestinal GLP-1 and satiation: from man to rodents and back. *Int J Obes*, 40(2):198–205, 2016.

[45] Qi K, Seo T, Jiang Z, Carpentier YA, and Deckelbaum RJ. Triglycerides in fish oil affect the blood clearance of lipid emulsions containing long- and medium-chain triglycerides in mice. *J Nutr*, 136(11):2766–72, 2006.

[46] Pond WG. *The biology of the pig*. Comstock Publishing, 1978.

[47] Armand M, Borel P, Dubois C, Senft M, Peyrot J, Salducci J, Lafont H, and Lairon D. Characterization of emulsions and lipolysis of dietary lipids in the human stomach. *Am J Physiol*, 266(3):G372–81, 1994.

[48] Braden B. Methods and functions: breath tests. *Best Pract Res Clin Gastroenterol*, 23(3):337–52, 2009.

[49] Mukuddem-Petersen J, Oosthuizen W, and Jerling JC. A systematic review of the effects of nuts on blood lipid profiles in humans. *J Nutr*, 135(9):2082–9, 2005.

[50] Steinert RE, Meyer-Gerspach AC, and Beglinger C. The role of the stomach in the control of appetite and the secretion of satiation peptides. *Am J Physiol Endocrinol Metab*, 302(6):E666–73, 2012.

[51] Dietrich CF and Braden B. Sonographic assessments of gastrointestinal and biliary functions. *Best Pract Res Clin Gastroenterol*, 23(3):353–67, 2009.

[52] Simonian HP, Maurer AH, Knight LC, Kantor S, Kontos D, Mega-looikonomou V, Fisher RS, and Parkman HP. Simultaneous assessment of gastric accommodation and emptying: studies with liquid and solid meals. *J Nucl Med*, 45(7):1155–60, 2004.

[53] Schwizer W, Fraser R, Borovicka J, Crelier G, Boesiger P, and Fried M. Measurement of gastric emptying and gastric motility by magnetic resonance imaging (MRI). *Dig Dis Sci*, 39(12):S101–3, 1994.

[54] Schwizer W, Steingoetter A, and Fox M. Magnetic resonance imaging for the assessment of gastrointestinal function. *Scand J Gastroenterol*, 41(11):1245–60, 2006.

[55] Marciani L. Assessment of gastrointestinal motor functions by MRI: a comprehensive review. *Neurogastroenterol Motil*, 23(5):399–407, 2011.

[56] Alyami J, Spiller RC, and Marciani L. Magnetic resonance imaging to evaluate gastrointestinal function. *Neurogastroenterol Motil*, 27(12):1687–92, 2015.

[57] Look DC and Locker DR. Time saving in measurement of NMR and EPR relaxation times. *Rev Sci Instrum*, 41(2):250–251, 1970.

[58] Taylor AJ, Salerno M, Dharmakumar R, and Jerosch-Herold M. T1 mapping: basic techniques and clinical applications. *JACC Cardiovasc Imaging*, 9(1):67–81, 2016.

[59] Fram EK, Herfkens RJ, Johnson GA, Glover GH, Karis JP, Shimakawa A, Perkins TG, and Pelc NJ. Rapid calculation of T1 using variable flip angle gradient refocused imaging. *Magn Reson Imaging*, 5(3):201–8, 1987.

[60] Yarnykh VL. Actual flip-angle imaging in the pulsed steady state: a method for rapid three-dimensional mapping of the transmitted radiofrequency field. *Magn Reson Med*, 57(1):192–200, 2007.

[61] Treier R, Steingoetter A, Weishaupt D, Goetze O, Boesiger P, Fried M, and Schwizer W. Gastric motor function and emptying in the right decubitus and seated body position as assessed by magnetic resonance imaging. *J Magn Reson Imaging*, 23(3):331–8, 2006.

[62] Nehrke K and Bornert P. DREAM - a novel approach for robust, ultrafast, multislice B1 mapping. *Magn Reson Med*, 68(5):1517–26, 2012.

[63] Woessner DE. Effects of diffusion in nuclear magnetic resonance spin-echo experiments. *J Chem Physics*, 34(6):2057–61, 1961.

[64] Malik SJ, Kenny GD, and Hajnal JV. Slice profile correction for transmit sensitivity mapping using actual flip angle imaging. *Magn Reson Med*, 65(5):1393–9, 2011.

[65] Sauter M, Curcic J, Menne D, Goetze O, Fried M, Schwizer W, and Steingoetter A. Measuring the interaction of meal and gastric secretion: a combined quantitative magnetic resonance imaging and pharmacokinetic modeling approach. *Neurogastroenterol Motil*, 24(7):632–e273, 2012.

[66] Steingoetter A, Sauter M, Curcic J, Liu D, Menne D, Fried M, Fox M, and Schwizer W. Volume, distribution and acidity of gastric secretion on and off proton pump inhibitor treatment: a randomized double-blind controlled study in patients with gastro-esophageal reflux disease (GERD) and healthy subjects. *BMC Gastroenterol*, 15(1):1–11, 2015.

[67] Vlaardingerbroek MT and den Boer JA. *Magnetic Resonance Imaging: Theory and Practice*. Springer, 2003.

[68] Hamilton G, Smith, D. L. J, Bydder M, Nayak KS, and Hu HH. MR properties of brown and white adipose tissues. *J Magn Reson Imaging*, 34(2):468–73, 2011.

[69] Mansson S, Peterson P, and Johansson E. Quantification of low fat contents: a comparison of MR imaging and spectroscopy methods at 1.5 and 3 t. *Magn Reson Imaging*, 30(10):1461–7, 2012.

[70] Longo R, Pollesello P, Ricci C, Masutti F, Kvam BJ, Bercich L, Croce LS, Grigolato P, Paoletti S, de Bernard B, and et al. Proton MR spectroscopy in quantitative in vivo determination of fat content in human liver steatosis. *J Magn Reson Imaging*, 5(3):281–5, 1995.

[71] Hussein MO, Hoad CL, Stephenson MC, Cox EF, Placidi E, Pritchard SE, Costigan C, Ribeiro H, Ciampi E, Rayment P, Nandi A, Hedges N, Sanderson P, Peters HPF, Kruse I, Marciani L, Spiller RC, and Gowland PA. Magnetic resonance spectroscopy measurements of intragastric fat fraction of oil emulsions in humans. *Eur J Lipid Sci Technol*, 117(1):31–36, 2015.

[72] Dixon WT. Simple proton spectroscopic imaging. *Radiology*, 153(1):189–94, 1984.

[73] Reeder SB, McKenzie CA, Pineda AR, Yu H, Shimakawa A, Brau AC, Hargreaves BA, Gold GE, and Brittain JH. Water-fat separation with IDEAL gradient-echo imaging. *J Magn Reson Imaging*, 25(3):644–52, 2007.

[74] Yu H, Shimakawa A, McKenzie CA, Brodsky E, Brittain JH, and Reeder SB. Multiecho water-fat separation and simultaneous R2* estimation with multifrequency fat spectrum modeling. *Magn Reson Med*, 60(5):1122–34, 2008.

[75] Reeder SB, Wen Z, Yu H, Pineda AR, Gold GE, Markl M, and Pelc NJ. Multicoil Dixon chemical species separation with an iterative least-squares estimation method. *Magn Reson Med*, 51(1):35–45, 2004.

[76] Tsao J and Kozerke S. MRI temporal acceleration techniques. *J Magn Reson Imaging*, 36(3):543–60, 2012.

[77] Pruessmann KP, Weiger M, Scheidegger MB, and Boesiger P. SENSE: sensitivity encoding for fast MRI. *Magn Reson Med*, 42(5):952–62, 1999.

[78] Griswold MA, Jakob PM, Heidemann RM, Nittka M, Jellus V, Wang J, Kiefer B, and Haase A. Generalized autocalibrating partially parallel acquisitions (GRAPPA). *Magn Reson Med*, 47(6):1202–10, 2002.

[79] Lustig M, Donoho D, and Pauly JM. Sparse MRI: the application of compressed sensing for rapid MR imaging. *Magn Reson Med*, 58(6):1182–95, 2007.

[80] Taubman DS and Marcellin MW. *JPEG2000 Image Compression Fundamentals, Standards and Practice*. Springer, 2002.

[81] Daubechies I, Defrise M, and De Mol C. An iterative thresholding algorithm for linear inverse problems with a sparsity constraint. *Commun Pure Appl Math*, 57(11):1413–57, 2004.

[82] Knoll F, Schultz G, Bredies K, Gallichan D, Zaitsev M, Hennig J, and Stollberger R. Reconstruction of undersampled radial PatLoc imaging using total generalized variation. *Magn Reson Med*, 70(1):40–52, 2013.

References

[83] Caballero J, Price AN, Rueckert D, and Hajnal JV. Dictionary learning and time sparsity for dynamic MR data reconstruction. *IEEE Trans Med Imaging*, 33(4):979–94, 2014.

[84] Elad M and Aharon M. Image denoising via sparse and redundant representations over learned dictionaries. *IEEE Trans Image Process*, 15(12):3736–45, 2006.

[85] Ravishankar S and Bresler Y. MR image reconstruction from highly undersampled k-space data by dictionary learning. *IEEE Trans Med Imaging*, 30(5):1028–41, 2011.

[86] Aharon M, Elad M, and Bruckstein A. K-SVD: an algorithm for designing overcomplete dictionaries for sparse representation. *IEEE Trans Signal Process*, 54(11):4311–22, 2006.

[87] Doneva M, Bornert P, Eggers H, Stehning C, Senegas J, and Mertins A. Compressed sensing reconstruction for magnetic resonance parameter mapping. *Magn Reson Med*, 64(4):1114–20, 2010.

[88] Zhu Y, Zhang Q, Liu Q, Wang YX, Liu X, Zheng H, Liang D, and Yuan J. PANDA-T1rho: integrating principal component analysis and dictionary learning for fast T1rho mapping. *Magn Reson Med*, 73(1):263–72, 2015.

[89] Li W, Griswold M, and Yu X. Fast cardiac T1 mapping in mice using a model-based compressed sensing method. *Magn Reson Med*, 68(4):1127–34, 2012.

[90] Chavhan GB, Babyn PS, Jankharia BG, Cheng HL, and Shroff MM. Steady-state MR imaging sequences: physics, classification, and clinical applications. *Radiographics*, 28(4):1147–60, 2008.

[91] Bruder H, Fischer H, Graumann R, and Deimling M. A new steady-state imaging sequence for simultaneous acquisition of two MR images with clearly different contrasts. *Magn Reson Med*, 7(1):35–42, 1988.

[92] Hardy PA, Recht MP, Piraino D, and Thomasson D. Optimization of a dual echo in the steady state (DESS) free-precession sequence for imaging cartilage. *J Magn Reson Imaging*, 6(2):329–35, 1996.

[93] Cheng CC, Mei CS, Duryea J, Chung HW, Chao TC, Panych LP, and Madore B. Dual-pathway multi-echo sequence for simultaneous frequency and T2 mapping. *J Magn Reson*, 265:177–87, 2016.

[94] Staroswiecki E, Granlund KL, Alley MT, Gold GE, and Hargreaves BA. Simultaneous estimation of T2 and apparent diffusion coefficient in human articular cartilage in vivo with a modified three-dimensional double echo steady state (DESS) sequence at 3 T. *Magn Reson Med*, 67(4):1086–96, 2012.

[95] Eckstein F, Hudelmaier M, Wirth W, Kiefer B, Jackson R, Yu J, Eaton CB, and Schneider E. Double echo steady state magnetic resonance imaging of knee articular cartilage at 3 Tesla: a pilot study for the Osteoarthritis Initiative. *Ann Rheum Dis*, 65(4):433–41, 2006.

[96] Welsch GH, Scheffler K, Mamisch TC, Hughes T, Millington S, Deimling M, and Trattnig S. Rapid estimation of cartilage T2 based on double echo at steady state (DESS) with 3 Tesla. *Magn Reson Med*, 62(2):544–9, 2009.

[97] Heule R, Ganter C, and Bieri O. Triple echo steady-state (TESS) relaxometry. *Magn Reson Med*, 71(1):230–7, 2014.

[98] Juras V, Bohndorf K, Heule R, Kronnerwetter C, Szomolanyi P, Hager B, Bieri O, Zbyn S, and Trattnig S. A comparison of multi-echo spin-echo and triple-echo steady-state T2 mapping for in vivo evaluation of articular cartilage. *Eur Radiol*, 26(6):1905–12, 2016.

[99] Fox AJS, Bedi A, and Rodeo SA. The basic science of articular cartilage: structure, composition, and function. *Sports Health*, 1(6):461–468, 2009.

[100] Stockwell RA. Lipid content of human costal and articular cartilage. *Ann Rheum Dis*, 26(6):481–6, 1967.

[101] Liu F, Chaudhary R, Block WF, Samsonov A, and Kijowski R. Multicomponent T2 analysis of articular cartilage with synovial fluid partial volume correction. *J Magn Reson Imaging*, 43(5):1140–7, 2016.

[102] Reiter DA, Lin PC, Fishbein KW, and Spencer RG. Multicomponent T2 relaxation analysis in cartilage. *Magn Reson Med*, 61(4):803–9, 2009.

[103] Kugel H, Jung C, Schulte O, and Heindel W. Age- and sex-specific differences in the 1h-spectrum of vertebral bone marrow. *J Magn Reson Imaging*, 13(2):263–8, 2001.

[104] Thomas LW. The chemical composition of adipose tissue of man and mice. *Q J Exp Physiol Cogn Med Sci*, 47:179–88, 1962.

[105] Scheffler K. A pictorial description of steady-states in rapid magnetic resonance imaging. *Concepts Magn Reson*, 11(5):291–304, 1999.

[106] Hennig J. Multiecho imaging sequences with low refocusing flip angles. *J Magn Reson*, 78(3):397–407, 1988.

[107] Hanicke W and Vogel HU. An analytical solution for the SSFP signal in MRI. *Magn Reson Med*, 49(4):771–5, 2003.

[108] Mizumoto CT and Yoshitome E. Multiple echo SSFP sequences. *Magn Reson Med*, 18(1):244–50, 1991.

[109] Goa PE, Poser BA, and Barth M. Modeling and suppression of respiration induced B0-fluctuations in non-balanced steady-state free precession sequences at 7 Tesla. *MAGMA*, 26(4):377–87, 2013.

[110] Liu D, Parker HL, Curcic J, Schwizer W, Fried M, Kozerke S, and Steingoetter A. The visualisation and quantification of human gastrointestinal fat distribution with MRI: a randomised study in healthy subjects. *Br J Nutr*, 115(5):903–12, 2016.

[111] Tropp JA and Gilbert AC. Signal recovery from random measurements via orthogonal matching pursuit. *IEEE Trans Inf Theory*, 53(12):4655–4666, 2007.

[112] Haacke EM, Brown RW, Thompson MR, and Venkatesan R. *Magnetic Resonance Imaging: Physical principles and sequence design*. John Wiley & Sons, 1999.

[113] Hardy PA, Recht MP, and Piraino DW. Fat suppressed MRI of articular cartilage with a spatial-spectral excitation pulse. *J Magn Reson Imaging*, 8(6):1279–87, 1998.

[114] Del Grande F, Santini F, Herzka DA, Aro MR, Dean CW, Gold GE, and Carrino JA. Fat-suppression techniques for 3-T MR imaging of the musculoskeletal system. *Radiographics*, 34(1):217–33, 2014.

[115] Bieri O, Ganter C, and Scheffler K. Quantitative in vivo diffusion imaging of cartilage using double echo steady-state free precession. *Magn Reson Med*, 68(3):720–9, 2012.

[116] Zheng S and Xia Y. On the measurement of multi-component T2 relaxation in cartilage by MR spectroscopy and imaging. *Magn Reson Imaging*, 28(4):537–45, 2010.

[117] Zimmet P, Alberti KG, and Shaw J. Global and societal implications of the diabetes epidemic. *Nature*, 414(6865):782–7, 2001.

[118] Reddy KS. Cardiovascular diseases in the developing countries: dimensions, determinants, dynamics and directions for public health action. *Public Health Nutr*, 5(1a):231–7, 2002.

[119] Poirier P, Giles TD, Bray GA, Hong Y, Stern JS, Pi-Sunyer FX, and Eckel RH. Obesity and cardiovascular disease: pathophysiology, evaluation, and effect of weight loss. *Circulation*, 113(6):898–918, 2006.

[120] Golding M and Wooster TJ. The influence of emulsion structure and stability on lipid digestion. *Curr Opin Colloid Interface Sci*, 15(1-2):90–101, 2010.

[121] Seimon RV, Wooster T, Otto B, Golding M, Day L, Little TJ, Horowitz M, Clifton PM, and Feinle-Bisset C. The droplet size of intraduodenal fat emulsions influences antropyloroduodenal motility, hormone release, and appetite in healthy males. *Am J Clin Nutr*, 89(6):1729–36, 2009.

[122] Wooster TJ, Day L, Xu M, Golding M, Oiseth S, Keogh J, and Clifton P. Impact of different biopolymer networks on the digestion of gastric structured emulsions. *Food Hydrocoll*, 36:102–114, 2014.

[123] Reis PM, Raab TW, Chuat JY, Leser ME, Miller R, Watzke HJ, and Holmberg K. Influence of surfactants on lipase fat digestion in a model gastro-intestinal system. *Food Biophys*, 3(4):370–81, 2008.

[124] Sarkar A, Horne DS, and Singh H. Interactions of milk protein-stabilized oil-in-water emulsions with bile salts in a simulated upper intestinal model. *Food Hydrocoll*, 24(2-3):142–51, 2010.

[125] Sek L, Porter CJ, Kaukonen AM, and Charman WN. Evaluation of the in-vitro digestion profiles of long and medium chain glycerides and the phase behaviour of their lipolytic products. *J Pharm Pharmacol*, 54(1):29–41, 2002.

[126] Day L, Golding M, Xu M, Keogh J, Clifton P, and Wooster TJ. Tailoring the digestion of structured emulsions using mixed monoglyceride-caseinate interfaces. *Food Hydrocoll*, 36:151–61, 2014.

[127] Hussein MO, Hoad CL, Wright J, Singh G, Stephenson MC, Cox EF, Placidi E, Pritchard SE, Costigan C, Ribeiro H, Ciampi E, Nandi A, Hedges N, Sanderson P, Peters HP, Rayment P, Spiller RC, Gowland PA, and Marciani L. Fat emulsion intragastric stability and droplet size modulate gastrointestinal responses and subsequent food intake in young adults. *J Nutr*, 145(6):1170–7, 2015.

[128] Marciani L, Ramanathan C, Tyler DJ, Young P, Manoj P, Wickham M, Fillery-Travis A, Spiller RC, and Gowland PA. Fat emulsification measured using NMR transverse relaxation. *J Magn Reson*, 153(1):1–6, 2001.

[129] Curcic J, Sauter M, Schwizer W, Fried M, Boesiger P, and Steingoetter A. Validation of a golden angle radial sequence (GOLD) for abdominal T1 mapping during free breathing: demonstrating clinical feasibility for quantifying gastric secretion and emptying. *J Magn Reson Imaging*, 41(1):157–64, 2015.

[130] Marciani L, Gowland PA, Spiller RC, Manoj P, Moore RJ, Young P, and Fillery-Travis AJ. Effect of meal viscosity and nutrients on satiety, intragastric dilution, and emptying assessed by MRI. *Am J Physiol Gastrointest Liver Physiol*, 280(6):G1227–33, 2001.

[131] Hoad CL, Parker H, Hudders N, Costigan C, Cox EF, Perkins AC, Blackshaw PE, Marciani L, Spiller RC, Fox MR, and Gowland PA. Measurement of gastric meal and secretion volumes using magnetic resonance imaging. *Phys Med Biol*, 60(3):1367–83, 2015.

[132] Yu H, Shimakawa A, McKenzie CA, Lu W, Reeder SB, Hinks RS, and Brittain JH. Phase and amplitude correction for multi-echo water-fat separation with bipolar acquisitions. *J Magn Reson Imaging*, 31(5):1264–71, 2010.

[133] Tsao J and Jiang Y. Hierarchical IDEAL: fast, robust, and multiresolution separation of multiple chemical species from multiple echo times. *Magn Reson Med*, 70(1):155–9, 2013.

[134] Steingoetter A, Fox M, Treier R, Weishaupt D, Marincek B, Boesiger P, Fried M, and Schwizer W. Effects of posture on the physiology of gastric emptying: a magnetic resonance imaging study. *Scand J Gastroenterol*, 41(10):1155–64, 2006.

[135] Lin LI. A concordance correlation coefficient to evaluate reproducibility. *Biometrics*, 45(1):255–68, 1989.

[136] Marciani L, Wickham M, Hills BP, Wright J, Bush D, Faulks R, Fillery-Travis A, Spiller RC, and Gowl PA. Intragastric oil-in-water emulsion fat fraction measured using inversion recovery echo-planar magnetic resonance imaging. *J Food Sci*, 69(6):E290–96, 2004.

[137] Banerjee S, Dixit S, Fox M, and Pal A. Validation of a rapid, semiautomatic image analysis tool for measurement of gastric accommodation and emptying by magnetic resonance imaging. *Am J Physiol Gastrointest Liver Physiol*, 308(8):G652–63, 2015.

[138] R Development Core Team. R: a language and environment for statistical computing. `https://www.R-project.org/`, 2015.

[139] Blundell JE, Lawton CL, Cotton JR, and Macdiarmid JI. Control of human appetite: implications for the intake of dietary fat. *Annu Rev Nutr*, 16(1):285–319, 1996.

[140] McClements DJ and Li Y. Structured emulsion-based delivery systems: controlling the digestion and release of lipophilic food components. *Adv Colloid Interface Sci*, 159(2):213–28, 2010.

[141] Mu H, Holm R, and Mullertz A. Lipid-based formulations for oral administration of poorly water-soluble drugs. *Int J Pharm*, 453(1):215–24, 2013.

[142] Hur SJ, Lim BO, Decker EA, and McClements DJ. In vitro human digestion models for food applications. *Food Chem*, 125(1):1–12, 2011.

[143] Scheuble N, Geue T, Windhab EJ, and Fischer P. Tailored interfacial rheology for gastric stable adsorption layers. *Biomacromolecules*, 15(8):3139–45, 2014.

[144] Khurana I. *Medical Physiology for Undergraduate Students*. Elsevier, 2014.

[145] Murray K, Placidi E, Schuring EA, Hoad CL, Koppenol W, Arnaudov LN, Blom WA, Pritchard SE, Stoyanov SD, Gowland PA, Spiller RC, Peters HP, and Marciani L. Aerated drinks increase gastric volume and reduce appetite as assessed by MRI: a randomized, balanced, crossover trial. *Am J Clin Nutr*, 101(2):270–8, 2015.

[146] Goetze O, Treier R, Fox M, Steingoetter A, Fried M, Boesiger P, and Schwizer W. The effect of gastric secretion on gastric physiology and

emptying in the fasted and fed state assessed by magnetic resonance imaging. *Neurogastroenterol Motil*, 21(7):725–e42, 2009.

[147] Fruehauf H, Menne D, Kwiatek MA, Forras-Kaufman Z, Kaufman E, Goetze O, Fried M, Schwizer W, and Fox M. Inter-observer reproducibility and analysis of gastric volume measurements and gastric emptying assessed with magnetic resonance imaging. *Neurogastroenterol Motil*, 23(9):854–61, 2011.

[148] Heinrich H, Goetze O, Menne D, Iten PX, Fruehauf H, Vavricka SR, Schwizer W, Fried M, and Fox M. Effect on gastric function and symptoms of drinking wine, black tea, or schnapps with a Swiss cheese fondue: randomised controlled crossover trial. *BMJ*, 341:c6731, 2010.

[149] Kunz P, Feinle-Bisset C, Faas H, Boesiger P, Fried M, Steingoetter A, and Schwizer W. Effect of ingestion order of the fat component of a solid meal on intragastric fat distribution and gastric emptying assessed by MRI. *J Magn Reson Imaging*, 21(4):383–90, 2005.

[150] Keogh JB, Wooster TJ, Golding M, Day L, Otto B, and Clifton PM. Slowly and rapidly digested fat emulsions are equally satiating but their triglycerides are differentially absorbed and metabolized in humans. *J Nutr*, 141(5):809–15, 2011.

[151] Hu HH, Bornert P, Hernando D, Kellman P, Ma J, Reeder S, and Sirlin C. ISMRM workshop on fat-water separation: insights, applications and progress in MRI. *Magn Reson Med*, 68(2):378–88, 2012.

[152] Liu CY, McKenzie CA, Yu H, Brittain JH, and Reeder SB. Fat quantification with IDEAL gradient echo imaging: correction of bias from T1 and noise. *Magn Reson Med*, 58(2):354–64, 2007.

[153] Treier R, Steingoetter A, Fried M, Schwizer W, and Boesiger P. Optimized and combined T1 and B1 mapping technique for fast and accurate T1 quantification in contrast-enhanced abdominal MRI. *Magn Reson Med*, 57(3):568–76, 2007.

[154] Sorensen T, Hohenstein S, and Vasishth S. Bayesian linear mixed models using Stan: a tutorial for psychologists, linguists, and cognitive scientists. `http://arxiv.org/abs/1506.06201`, 2015.

[155] Koopmans LH, Owen DB, and Rosenblatt JI. Confidence intervals for the coefficient of variation for the normal and log normal distributions. *Biometrika*, 51(1-2):25–32, 1964.

[156] Ma J. Dixon techniques for water and fat imaging. *J Magn Reson Imaging*, 28(3):543–58, 2008.

[157] Reeder SB, Bice EK, Yu H, Hernando D, and Pineda AR. On the performance of T2* correction methods for quantification of hepatic fat content. *Magn Reson Med*, 67(2):389–404, 2012.

[158] Mashhood A, Railkar R, Yokoo T, Levin Y, Clark L, Fox-Bosetti S, Middleton MS, Riek J, Kauh E, Dardzinski BJ, Williams D, Sirlin C, and Shire NJ. Reproducibility of hepatic fat fraction measurement by magnetic resonance imaging. *J Magn Reson Imaging*, 37(6):1359–70, 2013.

[159] Zhong X, Nickel MD, Kannengiesser SA, Dale BM, Kiefer B, and Bashir MR. Liver fat quantification using a multi-step adaptive fitting approach with multi-echo GRE imaging. *Magn Reson Med*, 72(5):1353–65, 2014.

[160] Gaeta M, Messina S, Mileto A, Vita GL, Ascenti G, Vinci S, Bottari A, Vita G, Settineri N, Bruschetta D, Racchiusa S, and Minutoli F. Muscle fat-fraction and mapping in Duchenne muscular dystrophy: evaluation of disease distribution and correlation with clinical assessments. *Skeletal Radiol*, 41(8):955–61, 2012.

[161] Karampinos DC, Baum T, Nardo L, Alizai H, Yu H, Carballido-Gamio J, Yap SP, Shimakawa A, Link TM, and Majumdar S. Characterization of the regional distribution of skeletal muscle adipose tissue in type 2 diabetes using chemical shift-based water/fat separation. *J Magn Reson Imaging*, 35(4):899–907, 2012.

[162] Burns AA, Livingstone MB, Welch RW, Dunne A, Reid CA, and Rowland IR. The effects of yoghurt containing a novel fat emulsion on energy and macronutrient intakes in non-overweight, overweight and obese subjects. *Int J Obes Relat Metab Disord*, 25(10):1487–96, 2001.

[163] Maljaars PW, van der Wal RJ, Wiersma T, Peters HP, Haddeman E, and Masclee AA. The effect of lipid droplet size on satiety and peptide secretion is intestinal site-specific. *Clin Nutr*, 31(4):535–42, 2012.

References

[164] Pruessmann KP, Weiger M, Bornert P, and Boesiger P. Advances in sensitivity encoding with arbitrary k-space trajectories. *Magn Reson Med*, 46(4):638–51, 2001.

[165] Sharma SD, Hu HH, and Nayak KS. Chemical shift encoded water-fat separation using parallel imaging and compressed sensing. *Magn Reson Med*, 69(2):456–66, 2013.

[166] Wiens CN, McCurdy CM, Willig-Onwuachi JD, and McKenzie CA. R2*-corrected water-fat imaging using compressed sensing and parallel imaging. *Magn Reson Med*, 71(2):608–16, 2014.

[167] Doneva M, Bornert P, Eggers H, Mertins A, Pauly J, and Lustig M. Compressed sensing for chemical shift-based water-fat separation. *Magn Reson Med*, 64(6):1749–59, 2010.

[168] Gdaniec N, Eggers H, Bornert P, Doneva M, and Mertins A. Robust abdominal imaging with incomplete breath-holds. *Magn Reson Med*, 71(5):1733–42, 2014.

[169] Hollingsworth KG, Higgins DM, McCallum M, Ward L, Coombs A, and Straub V. Investigating the quantitative fidelity of prospectively undersampled chemical shift imaging in muscular dystrophy with compressed sensing and parallel imaging reconstruction. *Magn Reson Med*, 72(6):1610–9, 2014.

[170] Ma D, Gulani V, Seiberlich N, Liu K, Sunshine JL, Duerk JL, and Griswold MA. Magnetic resonance fingerprinting. *Nature*, 495(7440):187–92, 2013.

[171] Hoge WS, Brooks DH, Madore B, and Kyriakos W. On the regularization of SENSE and Space-RIP in parallel MR imaging. In *Proc IEEE Int Symp Biomed Imaging*, pages 241–4, Arlington, USA, 2004.

[172] Ying L, Xu D, and Liang ZP. On Tikhonov regularization for image reconstruction in parallel MRI. In *Conf Proc IEEE Eng Med Biol Soc*, volume 2, pages 1056–9, San Francisco, USA, 2004.

[173] Roemer PB, Edelstein WA, Hayes CE, Souza SP, and Mueller OM. The NMR phased array. *Magn Reson Med*, 16(2):192–225, 1990.

[174] Lin FH, Kwong KK, Belliveau JW, and Wald LL. Parallel imaging reconstruction using automatic regularization. *Magn Reson Med*, 51(3):559–67, 2004.

[175] Laidlaw DH, Fleischer KW, and Barr AH. Partial-volume Bayesian classification of material mixtures in MR volume data using voxel histograms. *IEEE Trans Med Imaging*, 17(1):74–86, 1998.

[176] Busse RF and Riederer SJ. Steady-state preparation for spoiled gradient echo imaging. *Magn Reson Med*, 45(4):653–61, 2001.

[177] Liu YL, Riederer SJ, Rossman PJ, Grimm RC, Debbins JP, and Ehman RL. A monitoring, feedback, and triggering system for reproducible breath-hold MR imaging. *Magn Reson Med*, 30(4):507–11, 1993.

[178] Bland JM and Altman DG. Measuring agreement in method comparison studies. *Stat Methods Med Res*, 8(2):135–60, 1999.

[179] Reeder SB, Wintersperger BJ, Dietrich O, Lanz T, Greiser A, Reiser MF, Glazer GM, and Schoenberg SO. Practical approaches to the evaluation of signal-to-noise ratio performance with parallel imaging: application with cardiac imaging and a 32-channel cardiac coil. *Magn Reson Med*, 54(3):748–54, 2005.

[180] Wang X, Hernando D, and Reeder SB. Sensitivity of chemical shift-encoded fat quantification to calibration of fat MR spectrum. *Magn Reson Med*, 75(2):845–51, 2016.

[181] Mulkern RV and Panych LP. Echo planar spectroscopic imaging. *Concepts Magn Reson*, 13(4):213–37, 2001.

[182] Peterson P and Mansson S. Simultaneous quantification of fat content and fatty acid composition using MR imaging. *Magn Reson Med*, 69(3):688–97, 2013.

Curriculum Vitae

Dian Liu

born on June 24, 1987
German nationality

Education

2012 - 2016	**Doctoral degree** at the Institute for Biomedical Engineering, ETH Zurich, Switzerland
2006 - 2012	**Diplom degree** in Electrical Engineering and Information Technology, Technical University Darmstadt, Germany
2009 - 2010	**Exchange semester** at the Faculty of Electronic Engineering, Tsinghua University, Beijing, China
1997 - 2006	**Abitur** at the Gymnasium am Kurfürstlichen Schloss, Mainz, Germany

Practical experience

2011 - 2012	**Internship** at Siemens Corporate Research, Princeton, USA
2011	**Internship** at Philips Research, Eindhoven, the Netherlands
2010 - 2011	**Student assistant** at Fraunhofer Institute, Darmstadt, Germany
2008 - 2010	**Student assistant** at Technical University Darmstadt, Germany
2007	**Internship** at Sanofi, Frankfurt, Germany
2006	**Internship** at Deutsche Bahn, Darmstadt, Germany

List of publications

Journal articles

1. **Liu D**, Steingoetter A, Curcic J, Kozerke S. Exploiting multi-compartment effects in triple echo steady-state T_2 mapping for fat fraction quantification. *Magn Reson Med*, 2017.

2. Parker HL, **Liu D**, Curcic J, Ebert MO, Schwizer W, Fried M, Kozerke S, Steingoetter A. Gastric and post-gastric processing of ^{13}C markers renders the ^{13}C breath test an inappropriate measurement method for the gastric emptying of lipid emulsions in healthy subjects. *J Nutr*, 2017.

3. **Liu D**, Curcic J, Parker HL, Steingoetter A, Kozerke S. Accelerating MRI fat quantification using a signal model-based dictionary to assess gastric fat volume and distribution of fat fraction. *Magn Reson Imaging*, 37(1):81-9, 2017.

4. **Liu D**, Parker HL, Curcic J, Kozerke S, Steingoetter A. Emulsion stability modulates gastric secretion and its mixing with emulsified fat in healthy subjects in a randomized magnetic resonance imaging study. *J Nutr*, 146(10):2158-64, 2016.

5. **Liu D**, Parker HL, Curcic J, Schwizer W, Fried M, Kozerke S, Steingoetter A. The visualisation and quantification of human gastrointestinal fat distribution with MRI: a randomised study in healthy subjects. *Br J Nutr*, 115(5):903-12, 2016.

6. Steingoetter A, Sauter M, Curcic J, **Liu D**, Menne D, Fried M, Fox M, Schwizer W. Volume, distribution and acidity of gastric secretion on and off proton pump inhibitor treatment: a randomized double-blind controlled study in patients with gastro-esophageal reflux disease (GERD) and healthy subjects. *BMC Gastroenterol*, 15(1):111, 2015.

Conference proceedings

1. **Liu D**, Parker HL, Curcic J, Kozerke S, Steingoetter A. Simultaneous quantification of intragastric secretion and fat distribution. *ISMRM 24th Annual Meeting and Exhibition*, Singapore, Singapore, 2016.

2. **Liu D**, Curcic J, Steingoetter A, Kozerke S. Influence of multi-compartment effects on T_2 mapping using multiecho steady state imaging. *ISMRM 24th Annual Meeting and Exhibition*, Singapore, Singapore, 2016.

3. **Liu D**, Parker HL, Curcic J, Kozerke S, Steingoetter A. Visualizing and quantifying human fat digestion with IDEAL. *ISMRM 23rd Annual Meeting and Exhibition*, Toronto, Canada, 2015.

4. **Liu D**, Curcic J, Steingoetter A, Kozerke S. Accelerating water-fat separation for intragastric fat distribution with a signal model-based dictionary. *ISMRM 23rd Annual Meeting and Exhibition*, Toronto, Canada, 2015.

5. **Liu D**, Parker HL, Curcic J, Kozerke S, Steingoetter A. Visualizing and quantifying human fat digestion in vivo with magnetic resonance imaging. *4th International Conference of Food Digestion*, Naples, Italy, 2015.

6. **Liu D**, Curcic J, Kozerke S, Steingoetter A. Quantification of gastric secretion, mixing and emptying within single breath hold. *Joint Annual Meeting ISMRM-ESMRMB*, Milan, Italy, 2014.

7. **Liu D**, Curcic J, Steingoetter A, Kozerke S. Quantification of intra-gastric fat distribution using IDEAL. *Joint Annual Meeting ISMRM-ESMRMB*, Milan, Italy, 2014.

8. **Liu D**, Sauter M, Curcic J, Menne D, Fried M, Kozerke S, Schwizer W, Steingoetter A. Extent and formation of an acid layer (or "acid pocket") does not differ between GERD and healthy subjects. *Digestive Disease Week*, Orlando, USA, 2013, published in *Gastroenterology* 144(5):S182-3, 2013.

Acknowledgments

This dissertation would have never become possible without the contribution of all of those walking together with me along my PhD path, who paved the way in front of me, pointed at the right directions and kept me company.

First, I would like to thank my supervisor Prof. Dr. Sebastian Kozerke, who gave me the opportunity to embark on this journey to explore the fascinating world of magnetic resonance. Your office door was open whenever I needed advice and your constant support prevented me from straying too far away from the path. Many thanks also go to Prof. Dr. Peter Fischer for taking your time to read this thesis and for your exhilarant evaluation.

I would also like to thank Dr. Andreas Steingötter as my supervisor in the Gastro group for establishing an interdisciplinary framework, which made my journey all the more colorful. To keep it minimalistic: I cherish your enthusiasm towards research and commitment in all the discussions. You did your best to shield from me all the dramas down there (and, in contrast, to round the year off at all the lovely locations up there), which I very much appreciate.

My thanks also go to the rest of the Gastro group. Thank you, Jelena, for providing me a smooth start at the IBT. I highly value your straight opinion, which helped me to retain a clear vision during my journey. Thank you, Helen, for being my reliable study buddy through all kinds of study madness, during which the foundation for our future duet career was laid. Vlad, I can still vividly imagine your giggle echoing across the hallway, thank you for traveling with me among all the cardios and techs on the F floor.

Thank you, Nathalie, for providing me new emulsions to play with and showing me some fancy machines in your lab. Thank you, Dieter, for being our statistics guru for all kinds of problems involving significance (I'm not allowed to report its value). Thanks to everyone else over the years, Tobias Hahn, Martina Bertschimger, Matthias Sauter, Tijana Radovic and Werner Schwizer. Thank you, microfluidizer, for not blasting my ears off.

One of the great assets of the institute was its sheer endless abundance in knowledge. I thank Martin and Gérard for greeting me with bright smiles whenever I stumbled into your office, to tap into your vast expertise in image reconstruction and pulse programing. Thanks to the solid rock down in the MR center, Roger, for dealing with all emotional outbursts of the 1.5 T drama queen and your infinite motivation to go running. Thanks to Andi H for revealing the nuts and bolts for acquiring nice fat spectra.

My endurance on the path would not have lasted even halfway without the support of all my colleagues and the friends I found in them. Thanks, Nicole, for bearing my inscrutable moods and for ultraserious discussions about ice cream. Jonas & Josip a.k.a. "the Jojos" for mutual support in beach body training. Thanks to my current and past office mates, Giorgios, Manuela, Hyo, Lars, max, Laetitia and Alex. In retrospect, I could have stared on my screen less intensely and spent more time on chitchat! Kudos to Christian B, Christian G, Christian S, Claudio, Constantin, Jan, Jenny, Jonas S, Julia, Georg, Kerem, Maria, Matteo, Max F, Niklaus, Lukas, Patrick, Robbert, Romain, Sascha, Simon, Sophie, Thomas, Yolanda and Yoojin. Thank you for your patience at the ski lift, birthday cake ambitions, BQM pitchers! Thank you for the lovely unicorn!

Finally, I would like to express my gratitude to my parents, who discovered that the simple question "how's research?" could modulate all types of emotions, for offering me unconditional support and alternative PhD projects in event management. Thank you, Benjamin, who I encountered during my journey, for walking along with me on this path and many more to follow.